12-2012

UNDERSTANDING NANOPARTICLE-CELL INTERACTION

Ran Chen
Clemson University, ran@g.clemson.edu

UNDERSTANDING NANOPARTICLE-CELL INTERACTION

A Dissertation
Presented to
the Graduate School of
Clemson University

In Partial Fulfillment
of the Requirements for the Degree
Doctor of Philosophy
Physics

---

by
Ran Chen
December 2012

Accepted by:
Dr. Pu-Chun Ke, Committee Chair
Dr. Apparao Rao
Dr. Jian He
Dr. Feng Ding

ABSTRACT

Nanotechnology has revolutionalized the landscape of modern science and technology, including materials, electronics, therapeutics, bioimaging, sensing, and the environment. Along with these technological advancements, there arises a concern that engineered nanomaterials, owing to their high surface area and high reactivity, may exert adverse effects upon discharge to compromise biological and ecological systems. Research in the past decade has examined the fate of nanomaterials *in vitro* and *in vivo*, as well as the interactions between nanoparticles and biological and ecosystems using primarily toxicological and ecotoxicological approaches. However, due to the versatility in the physical and physicochemical properties of nanoparticles, and due to the vast complexity of their hosting systems, the solubility, transformation, and biocompatibility of nanomaterials are still poorly understood.

Accordingly, this dissertation offers a mechanistic study on the differential translocation of pristine and water-soluble fullerene nanoparticles in mammalian and plant cells (Chapter 2), an investigation on membrane fluidity upon exocytosis of gold nanoparticles by the cell (Chapter 3), and an in-depth examination of the formation of an array of nanoparticle-protein coronas and their interactions with lipid vesicles and the cell (Chapters 4 and 5).

The organization of this dissertation is as follows.

Chapter 1 presents a review on the general applications (gene and drug delivery, imaging, sensing, nanotherapy) and implications (toxicity) of nanomaterials, mostly within the context of biological systems. In addition, this chapter documents the

endocytotic and exocytotic pathways of the cell, and reviews the state-of-the-art of our understanding of nanoparticle-protein corona formation and nanoparticle-cell interactions, two precursors of nanotoxicity.

Chapter 2 offers, for the first time, a parallel study on the differential uptake of hydrophobic and amphiphilic fullerene nanoparticles by *Allium cepa* plant cells and HT-29 mammalian cells, two model systems representing ecological and biological systems. Methodologically, this study was conducted using a plant cell viability assay, bright field and fluorescence imaging, and, extensively, electron microscopy imaging.

Chapter 3 examines an important but rarely documented aspect of cellular response to nanoparticles – exocytosis. A lipophilic Laurdan dye was used to partition into HT-29 mammalian cell membranes. Membrane fluidity as a result of the discharge of gold nanoparticles was inferred from UV-vis absorbance as well as by calculating the general polarization value of the dye -- hereby treated an electric dipole in a lipid bilayer continuum -- based on its fluorescence emissions at two characteristic wavelengths.

Chapter 4 concerns protein adsorption on carbon nanotubes (CNTs) to form protein coronas in cell culture media, an environment relevant to both *in vitro* and *in vivo* studies. A label-free mass spectrometry-based proteomic approach was employed, and the compositions of the protein forming coronas on a set of CNTs were examined. The physicochemical properties of the CNTs were also extensively characterized in order to establish a correlation between protein adsorption and CNT surface properties.

Chapter 5 characterizes the formation of a serum albumin corona on silver nanoparticles and evaluates the impact of silver nanoparticle-albumin corona on the

fluidity of an artificial lipid vesicle. The reason of adopting a lipid vesicle in this study is to eliminate endo- and exocytosis and pinpoint the roles of physical forces in nanoparticle-cell interactions. In this chapter we also show the formation and conformational changes of fibrinogen corona in HT-29 cell lines. Fibrinogen is one of the most abundant types of plasma proteins in the bloodstream.

Chapter 6 summarizes the major findings in this dissertation and presents future work inspired by this PhD research.

DEDICATION

This dissertation is dedicated to my parents for their understanding, tolerance and unconditional support.

ACKNOWLEDGMENTS

I would like to thank many people who have made this dissertation possible.

My first and foremost gratitude goes to my PhD advisor, Dr. Pu-Chun Ke, whose guidance and scientific intuitions were the most enlightening. He helped me make a significant career transition from condensed matter physics to this highly multidisciplinary field of nano-biophysics. His passion for research, unmatched work ethics, and broad knowledge has always been an inspiration to everyone around him. Most importantly, he was always there whenever I needed his help. His contributions to this dissertation as well as to my personal advancement are of the most importance.

My appreciations go to my PhD committee members – Drs. Apparao M. Rao, Jian He, and Feng Ding, for their expertise, thoughtful suggestions on my PhD research proposal, and fruitful discussions throughout our collaborations. I would like to also thank my former committee member, Dr. Meredith Newby Spano, for her selfless help and constructive discussions.

I wish to thank the scientists whom I have collaborated with over these past years at Clemson. I thank Dr. George Huang for his help with cell culture, Dr. JoAn Hudson and her staff members for their assistance with electron microscopy, and Dr. Jared Brown for his support and advices. I thank Dr. Emppu Salonen at Aalto University in Finland for providing wonderful computer simulations that complemented and enhanced my research, Dr. Hong Luo for his help with plant cell culture, and Drs. Brian A. Powell and Anne M. Spuches for their instructions on isothermal titration calorimetry.

I would like to thank my colleagues and friends in the Nano-Biophysics and Soft Matter Laboratory: Dr. Sijie Lin, Dr. Tatsiana Ratnikova, Dr. Priyanka Bhattacharya, Pengyu Chen, Poonam Choudhary, Nick Geitner, Slaven Radic, Hengjia Wang, Aleksandr Käkinen, Andrew Baker, Matthew Stone, Mercy Lard, James Turner, Mark Bebber, Ryan Schurr, and other fellow graduate students in the Department of Physics and Astronomy at Clemson University. It was a great pleasure studying and working with them.

I would like to thank funding sources for this research: The National Science Foundation (CAREER Award CBET-0744040 and Grant CBET-1232724) and The National Institute of Environmental Health and Safety (Grant R01 ES019311 02S1).

Lastly, my special thanks go to Zhao Zhang, for making my time at Clemson more joyful.

TABLE OF CONTENTS

Page

Table of Contents (Continued)

Page

LIST OF TABLES

Table Page

LIST OF FIGURES

Figure Page

List of Figures (Continued)

Figure Page

List of Figures (Continued)

Figure Page

List of Figures (Continued)

Figure Page

List of Figures (Continued)

Figure Page

CHAPTER 1. LITERATURE REVIEW

1.1 Introduction

Since Richard Feynman's dream of "maneuvering things atom by atom", researchers have been pushing the limit of dimensions at which matter can be manipulated. With the inventions of electron microscopy and scanning probe microscopy, one can now observe and manipulate matter on the nanometer, or even atomic scale. Two decades of development later, nanotechnology has now become a highly interdisciplinary area of research, benefiting from the advancement in device/semiconductor physics, surface science, organic/biochemistry, cellular/molecular biology, and microfacrication, etc. Nanotechnology has also provided vastly new opportunities in materials science, electronics, diagnostics, medicine, and industrial engineering.

The properties of the materials change dramatically when their sizes are reduced from the bulk level to the nanoscale. The special properties relative to their bulk forms include: quantum confinement in semiconductor materials, surface plasmon resonance (SPR) in metallic materials, and superparamagnetism in magnetic materials. Reactivity of nanomaterials is usually magnified due to the much-increased surface area to mass ratio, such as that found in super catalytic nano-sized titanium particles. Thus, different approaches and strategies should be taken when dealing with nanosized objects.

Due to their unique physical and chemical properties and sizes comparable to biological matter, nanomaterials naturally converge with biology to elicit interesting phenomena. With the growth in the biological applications of nanomaterials, a

comprehensive understanding of the interactions between nanomaterials and biological systems has become essential to facilitate the applications and mitigate the adverse effects associated with nanomaterials. Such understanding can be achieved by integrating physical and biological sciences and nanotechnologies.

In this dissertation, the principles of physics, materials science, biochemistry, cell/molecular biology, as well as the techniques of spectroscopies and microscopies are utilized to investigate the interactions between biological matter, including the cell, artificial lipid membranes, and proteins, and nanoparticles (NPs) such as fullerenes and their derivatives, metallic gold and silver NPs, and carbon nanotubes, etc. Specifically, chapter 2 of this dissertation is focused on the cellular response and uptake of both mammalian and plant cells to either hydrophilic of hydrophobic NPs; chapter 3 discusses the discharge of NPs from the cell; chapter 4 describes the molecular interactions of proteins and carbon nanotubes; chapter 5 illustrates the impact of NP-protein corona on both lipid vesicles and living cells. The overall goal of this dissertation is to present a complete picture of NP-biosystem interactions.

1.2 Biological Applications of Nanomaterials

Based on their unique structural, physiochemical and optical properties, nanomaterials have found their application in various bio-related areas. For example, fullerene has been demonstrated to have anti-oxidative properties, [1] quantum dots have been used as fluorescence imaging agent, [2] magnetic NPs have been used as contrast

agents in magnetic resonance imaging (MRI) [3], liposomes can be used to deliver drugs and other biomolecules into the cell [4]. The aim of this section is to review the bio-related application of nanomaterials to illustrate the importance of understanding cell-nano interactions.

1.2.1 Drug/gene Delivery

The surface charge, chemical coating, morphology and hydrophobicity of NPs enable their binding with pharmaceutical agents or other biological molecules through electrostatic and hydrophobic interactions, hydrogen bonding, and *van der Waals* (vdW) forces, etc. [5] The small size enables the NPs to be taken up by the cells more easily than other larger carriers. [6–11] It the NPs are conjugated with specific ligands, they can be used to target very specific type of membrane receptors. The release of bound drug agents or molecules can accordingly be administered by changing the surface properties of the NPs. So far, various nanomaterials have been shown to be able to deliver therapeutic drugs, [12] ribonucleic acid (RNA), [13] deoxyribonucleic acid (DNA) [14], or lipids [15] into different cells or tissues within the body.

Kim et al. demonstrated the delivery of small interfering ribonucleic acid (siRNA) into human prostate cancer cells using cationic solid lipid NPs (SLN) reconstituted from low density lipoprotein (LDL).[13] In this study, the cationic SLN with a diameter of ~117 nm was prepared using a modified solvent-emulsification method from cholesteryl ester, triglyceride, cholesterol, dioleoylphosphatidylethanolamine (DOPE), and 3β-[N-

(N′,N′-dimethylaminoethane)- carbamoyl]-cholesterol (DC-chol) to mimic the chemical composition of a LDL particle. siRNA was conjugated with polyethylene glycol (PEG) through a disulfide bond, then anchored onto the surface of SLN via electrostatic interactions to render stable complexes in buffer solution and cell culture medium. (Figure 1-1) Such complex exhibited a higher gene silencing efficiency of green fluorescent protein (GFP) and vascular endothelial growth factor (VEGF) with a much lower cytotoxicity compared to that of polyethylenimine (PEI). Kim et al. also conducted flow cytometry studies to show that siRNA-PEG/SLN complexes were indeed efficiently taken up by the cells.

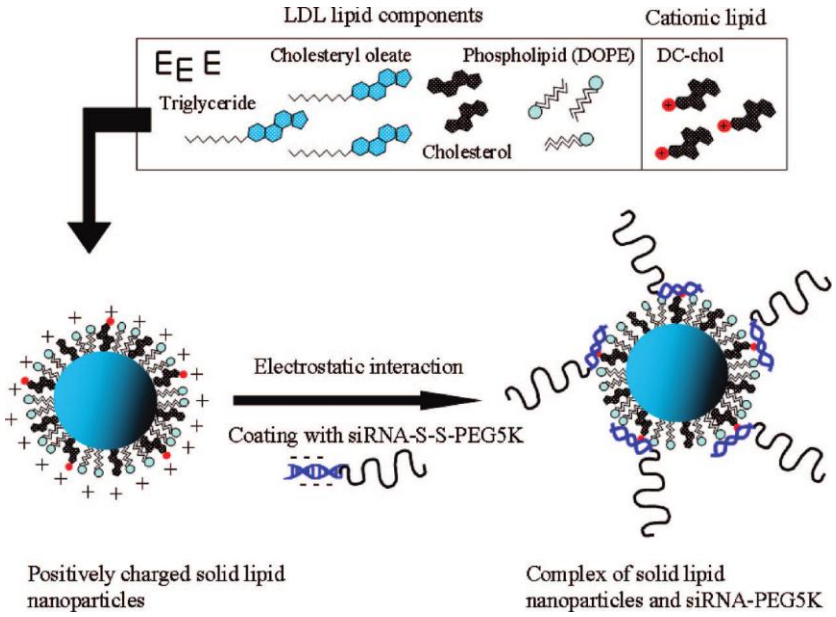

Figure 1-1 Schematic diagram of the assembly of lipid portions of low density lipoprotein (LDL), DOPE, and DC-chol for preparation of solid lipid NPs (SLN). The formulation of

siRNA-PEG/SLN complexes via electrostatic interactions between the positively charged SLN surface and negatively charged siRNA is illustrated. [13]

In another study conducted by Murakami et al., the *in vitro* binding and release of anti-inflammatory glucocorticoid dexamethasone (DEX) by single-wall carbon nanohorns (SWNH) and their oxidized form (oxSWNH) were investigated. [16] Adsorption analysis (Figure 1-2) using [^{3}H]-DEX determined that the adsorption capacity of oxSWNH to be ~200 mg/g in 0.5 mg/mL of DEX solution, ~6 times larger than that obtained for SWNHs. Adsorption kinetics of H_2-treated oxSWNHs indicated that oxSWNHs had a higher affinity for DEX than SWNHs due to the nanowindows in walls of oxSWNHs, not the oxygen functional groups. Such nanowindows allowed small molecules to infiltrate into the inner space of SWNHs, and the strong binding energy to the interior surface possibly contributed to the increased affinity for DEX. The authors also examined the responsiveness of glucocorticoid response elements (GRE) to DEX released from DEX-oxSWNHs using a reporter plasmid, pBV@-MMTV-LUC, which contained a luciferase gene under the control of GREs. As a result, the expression of luciferase positively corresponded to the DEX uptake rate. Figure 1-3 shows that free DEX activated expression of luciferase in a concentration-dependent manner. At concentration >0.1 μM, the activation was suppressed to levels below that seen at 0.1 μM. In addition, DEX-oxSWNHs also activated expression of luciferase dose-dependently whereas empty oxSWNGs induced no activation.

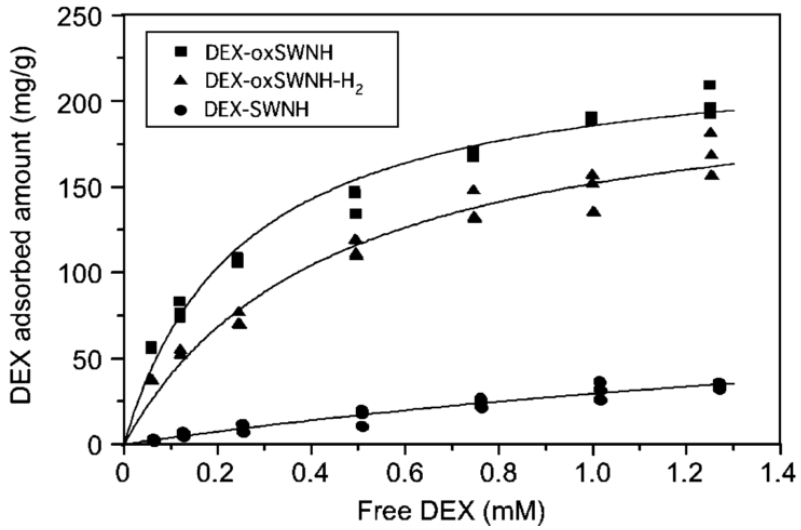

Figure 1-2 Langmuir adsorption isotherms describing adsorption of DEX by oxSWNHs, oxSWNH-H_2s, and SWNHs in a 1:1 ethanol/H_2O mixture: plotted is the amount of DEX adsorbed vs. the steady-state drug concentration; DEX-oxSWNHs (closed squares); DEX-oxSWNH-H_2s (closed triangles); DEX-SWNHs (closed circles). oxSWNHs, ox-SWNH-H2s, or SWNHs (50 μg/mL) and the indicated concentrations of DEX containing [^{3}H]-DEX were mixed in 1:1 ethanol/H2O and incubated overnight. The mixtures were then centrifuged and DEX-oxSWNHs, DEX-oxSWNH-H_2s, or SWNHs in the residues were quantified using a liquid scintillation counter. [16]

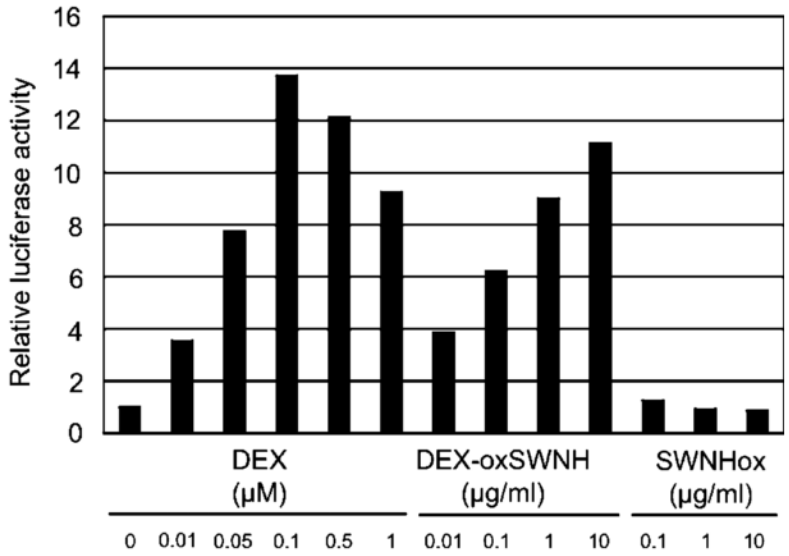

Figure 1-3 Effects of DEX-oxSWNHs and oxSWNHs on GR transcriptional activity. ST2 cells were transfected with pBV2- MMTV-LUC and treated with DEX, DEX-oxSWNHs, or oxSWNHs for 12 h. Firefly luciferase activity was measured in the cells lysates and normalized to the luciferase activity. The values in the figure represent the means of duplicate determinations. [16]

1.2.2 Imaging and Detection

Many nanomaterials possess unique optical or magnetic properties that can be utilized in various types of biomedical detection and imaging. For example, SPR of metal NPs like gold and silver can be utilized for the detection of adsorption of biological molecules like lipids and proteins as well as enhanced Raman spectroscopy and microscopy; [17–22] Raman scattering signal [23] and near infrared (NIR)

fluorescence/photoluminescence [24] of carbon nanotubes are often employed in biomolecule tracking, tissue and cell imaging.

Welsher et al. showed whole-animal imaging can be accomplished using an InGaAs camera in the 1-1.7 μm spectral range by detecting the intrinsic NIR photoluminescence of single-walled carbon nanotubes (SWCNT). [24] Due to the low autofluorescence and the ability to penetrate tissues beyond 1 μm in the near IR region, the photoluminescence of SWCNT can be used in tissue or even whole animal imaging. In this study, debundled and solubilized (in sodium cholate) pristine SWCNTs were further processed, displacing the attached sodium cholate with a phospholipid-polyethylene glycol (PL-PEG) group to obtain over one order of magnitude increased relative quantum yield compared to SWCNTs directly dispersed in PL-PEG as well as near-zero autofluorescence background in the SWCNT emission range (1,100-1,700 nm). (Figure 1-4) The NIR photoluminescence signal showed good tissue penetration, with clear images of SWCNTs in the vasculature under the skin.

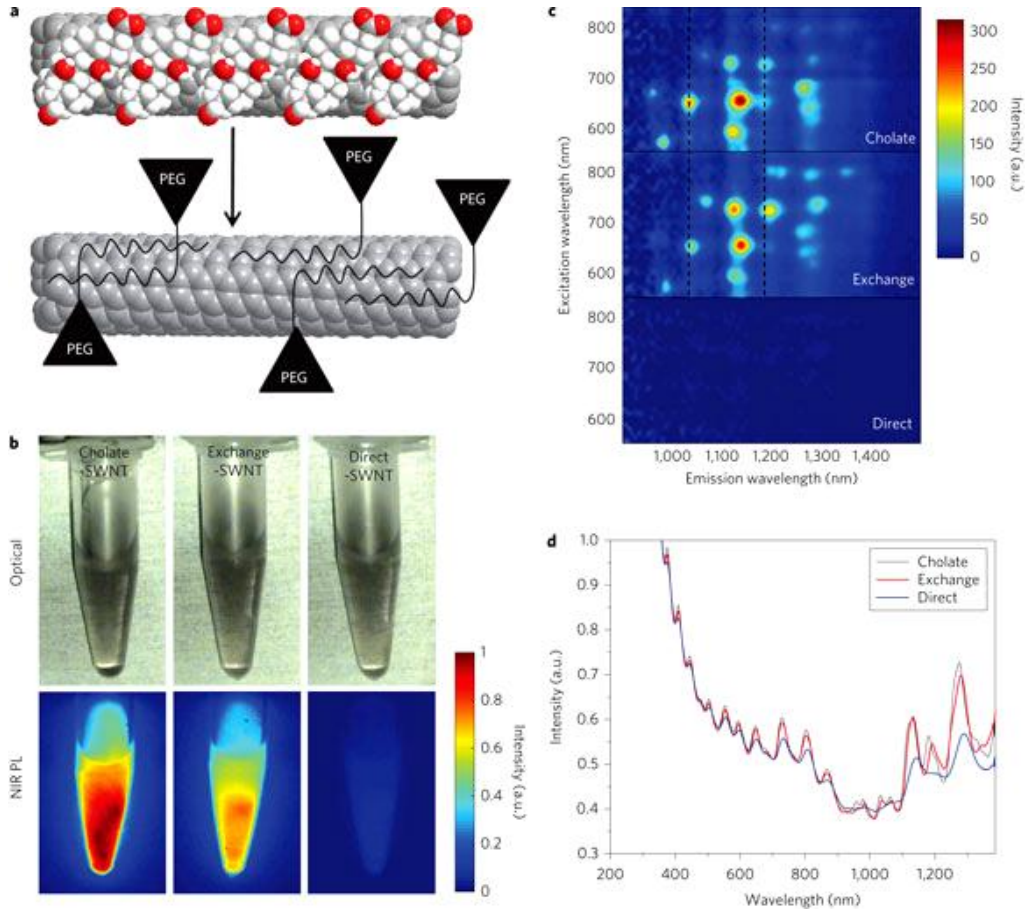

Figure 1-4 **a**, Schematic of the exchange process. Cholate (red and white balls) on SWCNTs (grey) is dialysed and eventually replaced by phospholipid–polyethylene glycol (PL–PEG) to form biocompatible nanotubes without damaging the integrity of the nanotube sidewall. **b**, NIR photoluminescence images of the three solutions excited at 808 nm at equal concentrations. Exchange-SWCNTs show greater fluorescence yield than direct-SWCNTs. **c**, Photoluminescence versus excitation spectra show improved quantum yield in cholate and exchange samples. The dotted lines show how peaks are redshifted after exchange. **d**, UV–vis–NIR curves. Exchange- and cholate-SWCNTs

show sharp transition peaks; direct-SWCNTs show very low and broad absorption features. PL, photoluminescence. [24]

Metallic NPs such as gold (AuNP) or silver (AgNP) possess a unique optical property – SPR: the free electrons can be resonantly excited at certain optical frequencies, enhancing the electromagnetic field at the NP surfaces. [25] As a result, these metallic NPs are often used to enhance the surface sensitivities of fluorescence, photoluminescence emission [26], or Raman scattering [27]. In a recent study Wang et al. developed a specific and sensitive methodology using epidermal growth factor (EGF)-surface enhanced spectroscopy (SERS) NPs to rapidly detect circulating tumor cells (CTC) in peripheral blood specimens from squamous cell carcinoma of the head and neck (SCCHN) of patients. [27] 60 nm citrate-stabilized AuNPs were conjugated with EGF through PEG-SH, with the N terminus of EGF peptide attached to the carboxyl function groups of PEG. (Figure 1-5) Due to the over expression of EGF receptor (EGFR) in the SCCHN cells, the EGF-functionalized AuNPs can easily attach to the SCCHN cells to induce SERS signals.

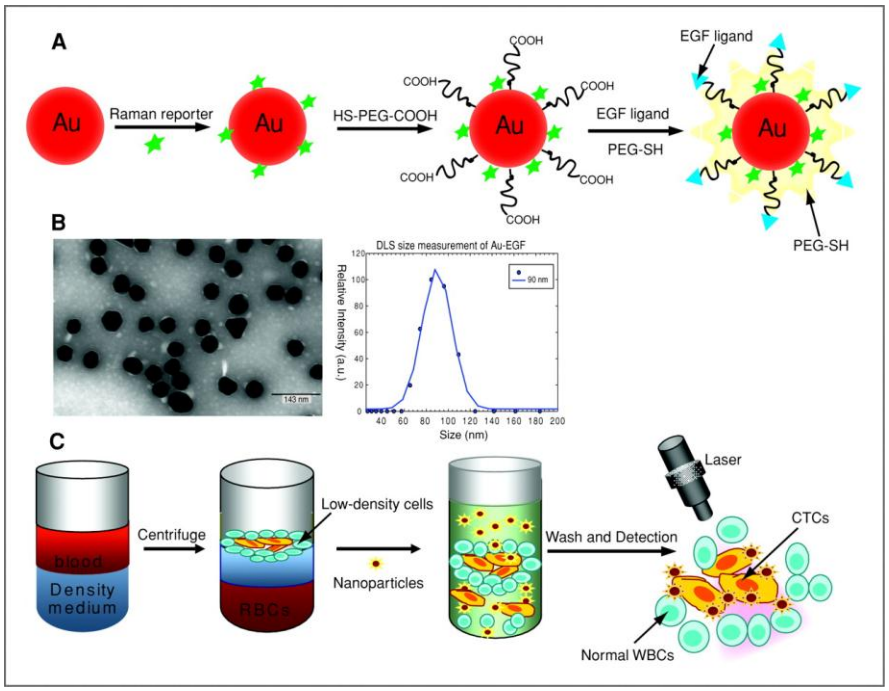

Figure 1-5 Design of EGF-SERS NP for labeling and detection of CTCs. A, preparation and schematic structures of Raman-encoded, PEG-stabilized, and EGF-peptide–functionalized SERS NP. B, TEM image and dynamic light scattering (DLS) measurement. C, assay principle of CTC detection from whole blood using EGF-SERS NPs. [27]

1.2.3 Nanotherapy

Some NPs possess properties that endow them as therapeutic agents. For example, metallic or metal-coated NPs can be used in photodynamic therapy with illumination from outside sources; some fullerene derivatives have been found to have anti-oxidative properties.

Loo et al. reported that gold-coated silica NPs (nanoshells) can be used for cancer therapy. [28] In one scheme, a 35 nm thick gold shell was grown on the surface a 120 nm silica core by the adsorption of small gold particles (1-3 nm) from gold colloids onto the silica surface. The optical resonance of those nanoshells in the NIR region, and the tissue penetrating property of NIR light allowed their combination for highly localized heating of targeted cancer cells. Then HER2 or IgG antibodies were tethered onto the gold nanoshell surfaces for the recognition by tumor cells. SKBr3 breast cancer cells were incubated with these nanoshells and exposed to NIR laser and the damaged cells were labeled with calcein-AM afterward. Figure 1- demonstrates the nanoshell-mediated photothermal destruction of tumor cells. After laser exposure, the cells within the laser spot from nanoshell containing samples underwent photothermal destruction as indicated by calcein-AM staining, while such effect was not present in samples exposed to nanoshell or NIR illumination alone.

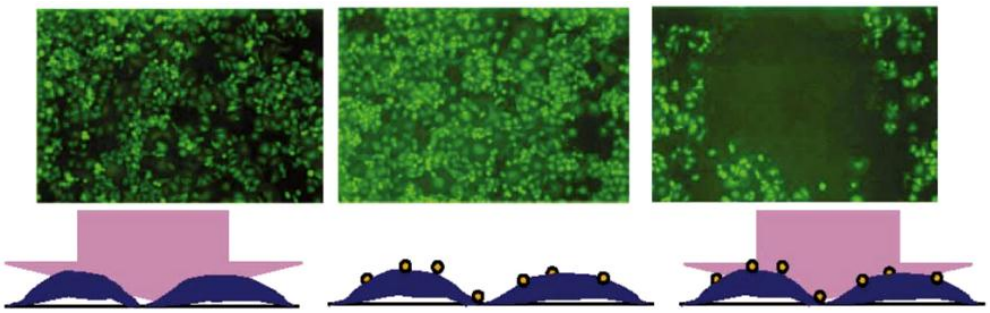

Figure 1-6 Calcein-AM staining of cells (green fluorescence indicates cellular viability). Left: cells after exposure to laser only (no nanoshells). Middle: cells incubated with nanoshells but not exposed to laser light. Right: cell incubated with nanoshells after laser

exposure. The dark circle seen in the image on the right corresponds to the region of cell death caused by exposure to laser light after incubation with nanoshells. [28]

Fullerene and its derivatives have been found to possess anti-oxidative properties; they can be used as medication against oxidative stresses induced by toxins, aging, and environmental stresses, etc. Our group recently reported that a hydroxylated fullerene derivative (fullerol, $C_{60}(OH)_{20}$) could suppress cell damage as well as reactive oxygen species (ROS) production induced by copper ions. [29] In this study, images of HT-29 cells were obtained for cell count after incubation with different agents. Toxicity was found to be decreased for cells pre-exposed to 20 mg/L fullerol relative to corresponding controls by 68.9% and 75.0%, after the cells were washed and then exposed to copper at LD20 and LD50 concentrations. (Figure 1-a) Furthermore, a DHL cell viability and proliferation assay kit (AnaSpec) was used to detect cell damage by the fluorescence intensities of the resorufin, which indicated the mitochondrial dehydrogenase activity of the cells. The cells treated with 20 and 50 mg/L fullerol showed 29.6% and 68.5% reduced damage for 6 h exposure to copper, 14% and 27.5% reduce for 12 h exposure. (Figure 1-b). Such reduce in toxicity was attributed to the anti-oxidative property of fullerol, proved by a ROS production study showing pretreating the cells with of 20 mg/L fullerol significantly decreased the cellular accumulation of ROS induced by copper and hydrogen peroxide by 14.3% and 15.0%, (Figure 1-b) while the addition of same concentration of fullerol in cell culture medium did not affect the ROS accumulation. (Figure 1-a)

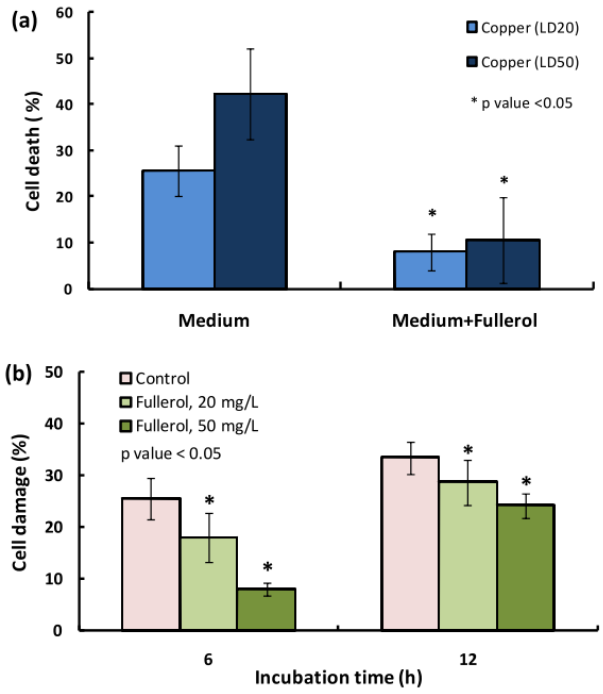

Figure 1-7 Cell damage in the presence of fullerols and copper ions. (a) Cell count: the cells were pre-exposed to 20 mg l−1 of fullerols and the washed cells were then treated with copper at LD20 and LD50 concentrations. After 24 h, the cells were washed three times with PBS and cell numbers were counted. The controls for calculating cell damage for medium and medium+fullerols (20 mg l−1, LD20) samples were the medium and medium+fullerol (LD20) without any copper ions. The results are the means ±standard errors of three repeats. Statistically significant differences between the band intensities were determined by the Student's t -test (* $p < 0.05$). (b) Relative damage of HT-29 cells pre-exposed to 0 mg/l (control), 20 mg/l, and 50 mg/l fullerols after 6 and 12 h and subsequent exposure to copper at LD50 concentration. The damage was calculated relative to the controls containing no copper ions. The results are the means ±standard errors of eight repeats. [29]

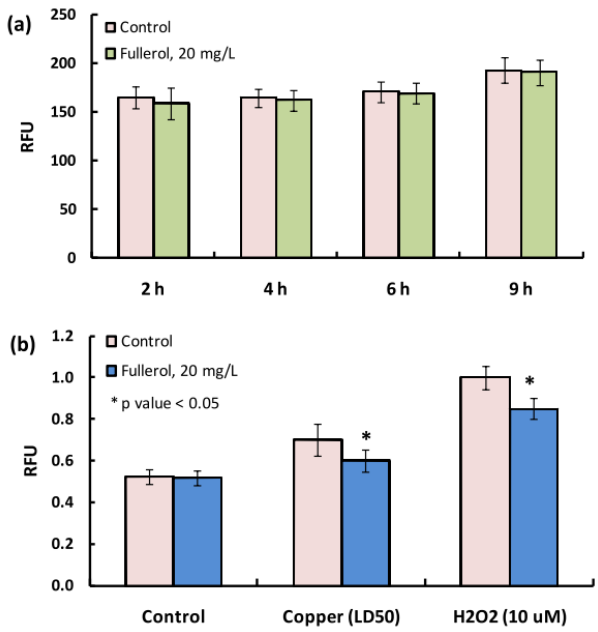

Figure 1-8 Intracellular ROS production after cell exposure to fullerols for 9 h and to copper (LD50) and $H2O_2$ (10 µM) for an additional 9 h. The cells were first treated with 1 mMDCFH-DA for 60 min. (a) The cells were incubated with 20 mg l−1 fullerols and their fluorescencewas monitored up to 9 h. (b) Accumulation of intracellular ROS products in the presence (darker bars) and absence (lighter bars) of 20 mg l−1 fullerols after 9 h. The results are the means ±standard errors of two experiments each carried out in triplicate. RFU: relative fluorescence units. Statistically significant differences between the samples and the controls in each condition were determined by the Student's t -test (*: $p < 0.05$). [29]

1.3 Implications of Nanomaterials

1.3.1 Production of Nanomaterials

Due to their large potential in biomedical research as well as in other industries such as home appliances, electronics, automotive, and cosmetics, a vast and rapidly growing quantity of nanomaterials has been produced every year. (Figure 1-9) [30] The total production of nanomaterials is projected to increase from estimated 2,300 tons in 2006 to 58,000 tons by the end of 2020. [31] As a result, understanding the fate of both administered and unintentional release of nanomaterials in biological and ecosystems has become crucially important for guiding the safe development of nanotechnology and human health and environmental protection.

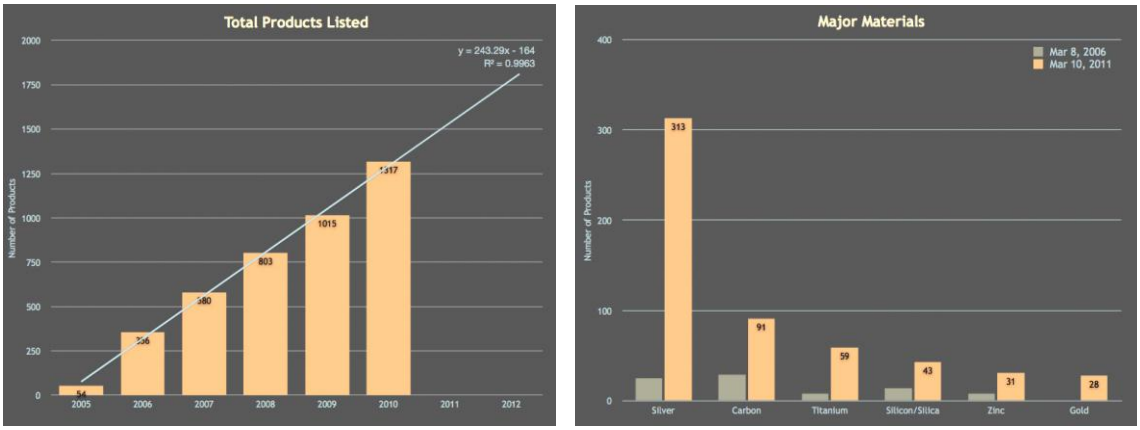

Figure 1-9 (Left) Number of total products listed, by date of inventory update, with regression analysis. (Right) Numbers of products associated with specific materials. [30]

1.3.2 Toxicity of Nanomaterials

As aforementioned, the effects of nanomaterials on biological systems highly depend on the physicochemical properties of the materials (size, aspect ratio, morphology, charge, surface coating, etc.). [32–40] Along with the numerous applications of nanomaterials in diagnostics and bioimaging, the toxicities of these materials have become a major concern. Studies suggested toxicities associated with the exposure of biological systems to nanomaterials could be attributed to different causes, such as membrane damage, [41], [42] toxic metal ion release, [43–45] ROS production, [32], [36], [46–50] binding with specific cellular machineries that prohibit their normal functionality, [51–53] and genotoxicity, [32], [54–61] etc. Yang et al. found both particle composition and shape were key factors in determining the toxicity of nanomaterials. [32] They utilized methyl thiazolyl tetrazolium (MTT) and water-soluble tetrazolium (WST) assays to evaluate the cytotoxicity of 4 types of NPs: carbon black (CB), SWCNT, silicon dioxide (SiO_2) and zinc oxide (ZnO). ZnO was found to be much more toxic than the non-metal NPs. (Figure 1-5). Their further measurements on glutathione depletion, malondialdehyde production, superoxide dismutase inhibition, and reactive oxygen species generation indicated that oxidative stress could play an important role in causing toxic effects. Although carbon nanotubes (CNTs) were less cytotoxic, comet assay showed that they induced more DNA damage. In comparison, CB and SiO_2 were found relatively non-toxic. Other studies suggested that ion release of metallic NPs could be a major cause of cytotoxicity. For example, Hanagata et al. proposed that the mechanism for lung epithelial A546 cell response to copper oxide (CuO) NPs was

derived from the copper ions released from the CuO-NPs in the aqueous solution. [62] In their study, the A546 cells were exposed to either CuO-NP or the ions released by CuO-NPs and assessed with WST assay which is based on the production of formazan from WST-8 by mitochondrial dehydrogenases in viable cells. Their results showed that both CuO-NPs and the released copper ions damaged mitochondria after 4 h of exposure. Their study further revealed genotoxicity induced by the CuO-NPs: after exposure, genes involved in mitogen-activated protein kinase pathways were upregulated while genes involved in cell cycle progression were downregulated, similar to cells exposed to Cu ions.

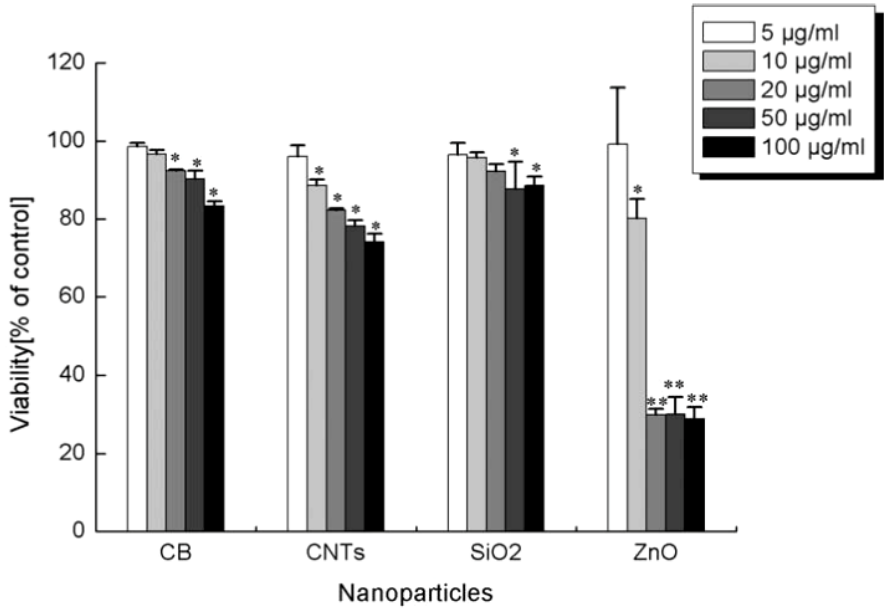

Figure 1-5 Viability of PMEF cells exposed to NPs with different exposure concentrations determined by the WST assay. Cells were respectively treated with 5, 10, 20, 50 and 100 µg/ml of CB, CNT, SiO_2 and ZnO for 24 h. The viability was measured with the WST assay and results are given in percent related to untreated to controls.

Results are the mean ± SEM (vertical bars) of three independent experiments each carried out in triplicate. *P < 0.05; **P < 0.01 in comparison to untreated controls. [32]

Valant et al. conducted a related study on the toxicity of TiO_2 and ZnO NPs as well as fullerenes *in vivo*. [63] In this study an acridine orange/ethidium bromide (AO/EB) assay was used for assessment of cell membrane stability of entire organs exposed to targeted nanomaterials. The digestive glands (hepatopancreas) of terrestrial ispods were taken as a model system for toxicity assessment. After validated with $Cu(NO_3)_2$ and surfactants, this assay showed that all tested nanomaterials had the potential ability to destabilize cell membranes. Among the three types of nanomaterials, fullerene caused the most significant membrane destabilization. (Figure 1-6) Also, sonicated NPs were found to be more biologically active than the nonsonicated ones.

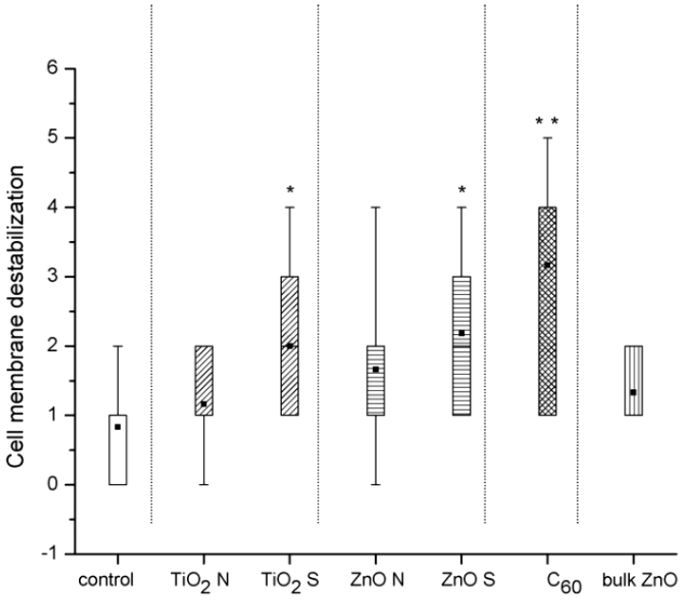

Figure 1-6 Membrane integrity (nuclei stained with EB) of the hepatopancreatic cells after oral application of NPs. Statistical differences between control group and exposed groups are marked as different numbers of stars ($p<0.05$ – *, $p<0.01$ – **). [63]

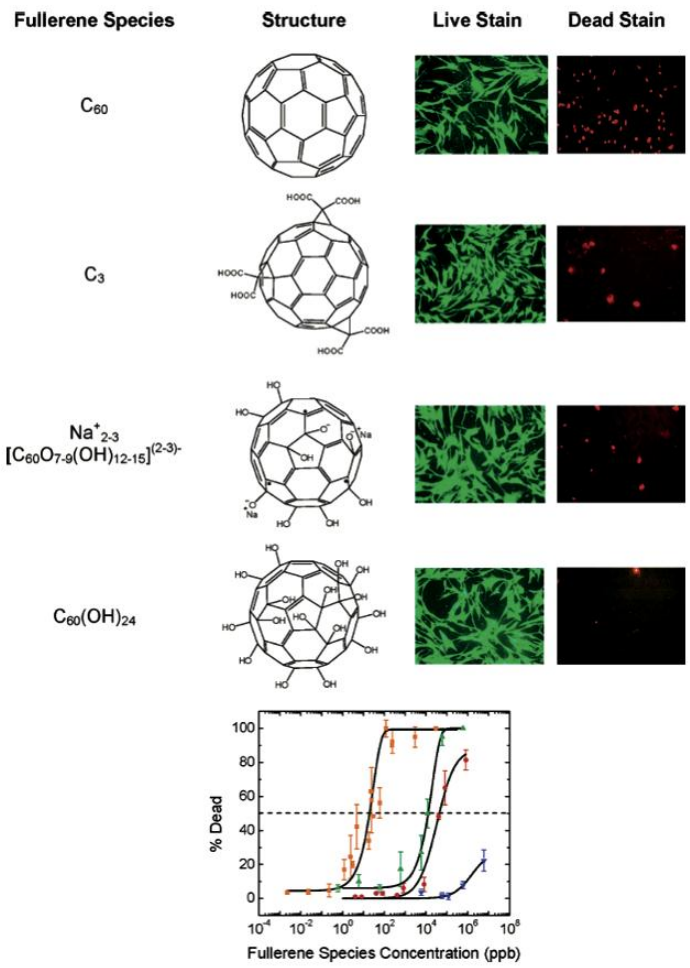

Figure 1-7 Differences in the structure and cellular activity of nano-C_{60}, C_3, $Na^{+}_{2-3}[C_{60}O_{7-9}(OH)_{12-15}]^{(2-3)-}$, and $C_{60}(OH)_{24}$. The structure of each fullerene species is shown in the table, as well as the live and dead stains. (Bottom) The differential cytotoxicity of nano-C_{60} (■) as compared to C_3 (▲), $Na^{+}_{2-3}[C_{60}O_{7-9}(OH)_{12-15}]^{(2-3)-}$ (●), and $C_{60}(OH)_{24}$ (▼) in human dermal fibroblasts. Cells were exposed to toxicant for 48 h. [64]

The toxicities of fullerenes and their derivatives were also assessed by Sayes et al. [64] Their study revealed that pristine C_{60} was cytoxic to both human dermal fibroblasts

(HDD) and human liver carcinoma cells (HepG2) at the 20 ppb level. In comparison, the carboxylated C_3 and $Na^{+}_{2\text{-}3}[C_{60}O_{7\text{-}9}(OH)_{12\text{-}15}]^{(2\text{-}3)-}$ water-soluble fullerene derivatives were less toxic, while $C_{60}(OH)_{24}$ showed no toxicity up to its upper limit of solubility. This result implies that functional groups on the surface of fullerenes that render their solubility also significantly decrease their cytotoxicity. (Figure 1-7) The superoxide anions generated by fullerenes in cell-free studies could be responsible for membrane oxidation exhibited in such cytotoxicity tests.

In connection with their potential for biomedical imaging, the toxicity of quantum dots (QDs) has also been studied extensively on both cellular and whole organism level. [39], [65–68] QDs usually have a core/shell structure composed of atoms from groups II-VI and III-V on the periodic table, such as cadmium (Cd), selenium (Se), lead (Pb) and arsenic (As), often synthesized with polymer surface coatings to yield stability and steric separations of the NPs in aqueous solution. Soluble organic polymers such as PEG as well as biomolecules such as amino acids, peptides, DNA have been used for surface coating of QDs to render their water solubility and biocompatibility. [66] Many of the core materials for QD synthesis are known to be toxic, however. When QDs are applied under conditions where degradation of the shell or coating materials is feasible, exposure of their toxic cores to the aqueous environment, often oxidative, would release toxic ions to the host system. As a result, the stability of the shell or surface coating is one of the key factors in the assessment of QD toxicity. [69] Strategically, additional functional groups or ligands can be attached to the surface of QDs to improve the biocompatibility and bioavailability. Derfus el al. showed CdSe-core QDs were cytotoxic to hepatocytes

by releasing Cd ions through the formation of reduced Cd due to surface oxidation. Such toxicity was shown to be significantly reduced by surface coating with ZnS or bovine serum albumin (BSA). [39] Li et al. found that the difference in the chirality of the Glutathione surface coating could also affect the cytotoxicity of QDs: nonbiologically active D-tripeptide glutathione (GSH)-coated QDs showed less cytotoxicity than L-GSH-coated ones, possibly due to chirality-dependence of autophagy activation, which is usually correlated with cell death. [66]

Besides entering mammalian cells or tissue during medical procedures, NPs unintentionally released to or naturally formed in the environment could elicit an ecotoxicity. In the ecosphere nanomaterials could interact with various organisms including animals, plants and microbes, and get transferred through the entire food chain. Consequently, nanomaterial-induced toxicity on aquatic organisms has been evaluated. Oberdörster reported that engineered fullerenes could induce oxidative stress in the brain of juvenile largemouth bass, [70] and significant lipid peroxidation was found in the brains of large-mouth bass after 48 h of exposure. Fang et al. found that both Gram-negative and Gram-positive bacteria changed their phospholipid composition and assumed phase transition after exposure to fullerenes. [71] Roberts et al. discovered that *Daphnia* magna ingested lysophophatidylcholine (LPC)-coated SWCNT through a normal feeding behavior and modified solubility of the nanotubes through digesting the LPC coating. Such modification of nanotube surface chemistry led to an acute toxicity at high concentrations. Lin et al. and Bhattacharya et al. examined the effect QDs and plastic NPs on algal photosynthesis, and found that the adsorption of both QDs and

plastic NPs significantly inhibited photosynthesis through either altering the photochemistry of plant species or the blockage of light and airflow. In the case of plastic NP, such adsorption was found to also promote algal ROS production. [72], [73]

Plants are an essential part of the ecosystem, and their response to NP exposure is therefore of great interest. [74] Lin et al. characterized the dynamic uptake, compartment distribution and transformation of natural organic matter (NOM)-suspended fullerene C_{70} in rice plants, and detected transmission of C_{70} to the rice progeny through seeds. [23] Liu et al. discovered water-soluble fullerenes ($C_{70}(C(COOH)_2)_{4-8}$) could inhibit *Arabidopsis* thaliana plant growth on the cellular level, particularly in seedling roots with shortened length and loss of gravitropism. [75] Fluorescence imaging of the root cells revealed phytotoxic effects at the cellular level, including auxin disruption, abnormal cell division, and microtubule disorganization. Graphene was shown to induce phytotoxicity in the seedling stage of cabbage, tomato, red spinach, and lettuce. [76] In this study, H_2O_2 visualization indicated overproduction of ROS, which could be responsible for significant plant growth inhibition and biomass reduction. Both necrotic damage lesions and massive electrolyte leakage indicated an oxidative stress mechanism mediated through the necrotic pathway.

1.4 Interactions between Nanoparticles and the Cell

Numerous studies have shown that engineering nanomaterials that possess maximal loading capacity, accurate targeting, controlled release, and minimal toxicities

requires an intimate understanding of the interaction between nanomaterials and their host systems. This section therefore focuses on a review of the structures, components and activities of biological systems, the interactions of those structures and components with NPs along their uptake pathways, and the impact of NPs on biological activities of their host systems.

As the building blocks and functional unit of any living organisms, cells are at the center of examining the interactions of living systems and nanomaterials. Historically research of the nano-safety community has been focused on eukaryotic cells, especially mammalian cells. With that consideration we review the state with the framework of mammalian systems; the different cytotoxicities induced by nanomaterials in mammalian and plant cells will be discussed in chapter 2. [77]

From a microscopic and physical point of view, the interaction of NPs with the cell can be further broken down to various specific physical or chemical interactions at the nano-bio interfaces, at the organelle or molecular level. The interactions may include vdW force, electrostatic, hydrogen bonding, and chemical reactions. Typically the NPs used for biological applications have diverse sizes, shapes, and chemical coatings for enhanced solubility and biocompatibility, and the biological environment the NPs target is vastly complex, consisting of proteins, peptides, nucleic acids, and lipids, etc. Upon integration, the conformation of the biomolecules undergoes changes due to the presence of the NPs, and the NP surface chemistry is readily modified by the biomolecules and enzymes in the host systems. (Figure 1-8) In addition, the flexible, heterogeneous and non-uniform cell membrane experiences fluctuations to account for the energy exchange

resulting from NP-lipid/protein interactions. If the NP is comparable to membrane lipid rafts in size, their interactions could become highly dependent on the exactly locations of the NPs. The unevenly distributed receptors and other membrane proteins also make the interactions difficult to predict and analyze. (Figure 1-9) The biological activities of the cell create a dynamic interface, adding another dimension of complexity to the interactions: active transporting of ions, proteins and other biomolecules; adenosine-5'-triphosphate (ATP) dependent endocytosis and exocytosis; cell skeleton protein polymerization; active NP transport, and processes after NP internalization, etc. (Figure 1-10) [5]

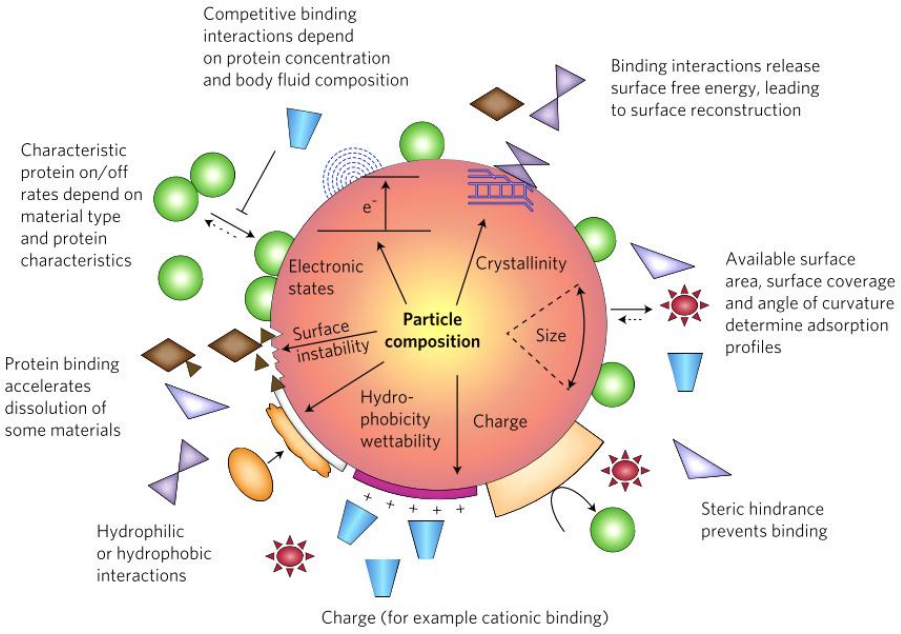

Figure 1-8 Biological molecules interacting with the surface of a NP. [5]

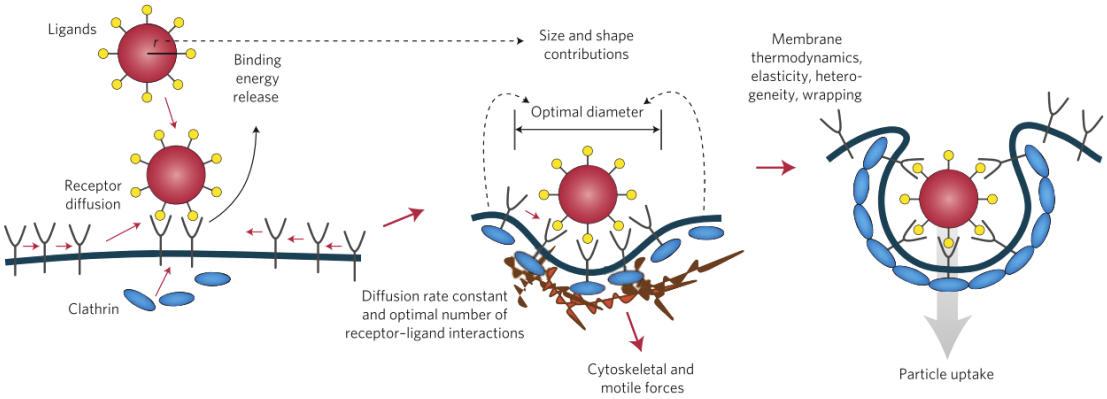

Figure 1-9 A coated NP interacting with a patch of nonuniform and dynamic cell membrane. [5]

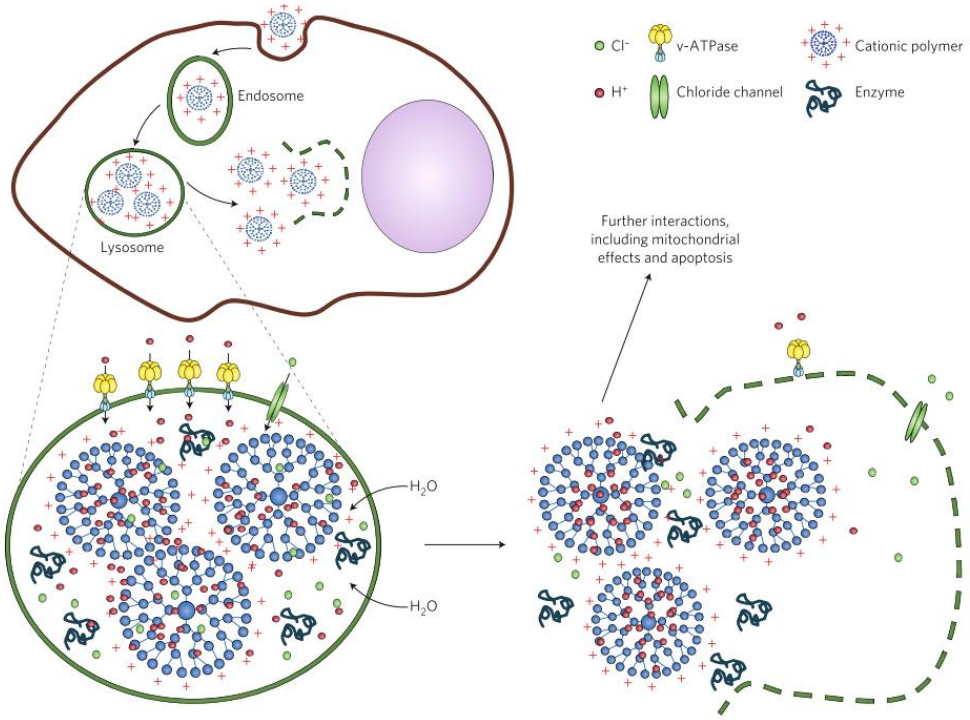

Figure 1-10 Uptake, transport, and processing of a positively charged NP. [5]

NP-cell membrane interactions

Cell membrane is a soft and fluid structure that envelops the cell, for both prokaryotes and eukaryotes, separating and protecting the intracellualar organelles from the outside environment. The functions of cell membrane include mediating the cell volume, regulating biomolecular and ion trafficking, and maintaining the electric potential and osmotic pressure of the cell. The integrity of the cell membrane is therefore extremely essential for normal cellular functions. Cell membrane is made mostly from a phospholipid bilayer, with hydrophobic fatty acid tails shielded in the middle of the layers and hydrophilic heads pointing out toward the aqueous environment. [78], [79] Because of the biological functionality and position of cell membrane, the interaction of membrane with nanomaterials is a focus of study. The biological membrane is dynamic; the assembly is formed through hydrophobic force in an aqueous environment, with thermal dynamically driven lipid movements present, such as lateral diffusion, vibration, and flip-flop. Due to the different physicochemical properties associated with the lipid heads of the membrane, including head size, polarity and charge, as well as the length, degree of saturation, and configuration isomerism of the fatty acid chain, the fluidity, water permeability, lipid dynamics of the membrane could change significantly and instantaneously. Accordingly, the interaction of nanomaterials of different composition and surface chemistry with such membrane could exert a great influence on the membrane dynamics. A molecular dynamics (MD) simulation study done by Nielsen et al. showed a lipid bilayer perturbation caused by the presence of a transmembrane nanotube, as well as the response of the nanotube to the lipid bilayer. The perturbations observed include ordering of the lipid head-to-tail vectors in the membrane plane, and

lipid tail density modulations due to molecular layering at the lipid-nanotube interface. (Figure 1-) [80] Experimental study has also shown the impact of the presence of NP on lipid bilayer structure. For example, Wang et al. discovered the nonspecific adsorption of charged NPs onto an artificial lipid vesicle could induce lipid reconstruction. In this study the lipids used to form the vesicles had a negative charge on their necks, and a positive charge on their heads. When the vesicles were mixed with negatively charged NPs, local gelation occurred in an otherwise fluidic bilayer, while when mixed with positively charged NPs the otherwise gelled membrane fluidized locally. Thus, through the adsorption of differently charged NPs, the nominal phase transition temperature could be shifted significantly. (Figure 1-) [81]

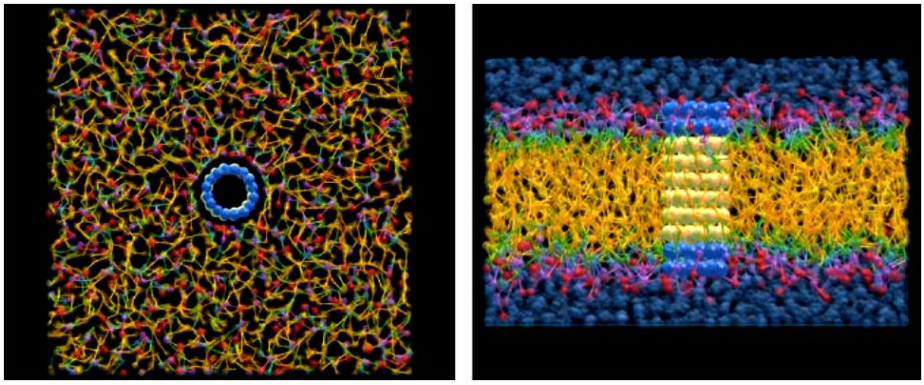

Figure 1-16 (Left) Snapshot of the simulation unit cell consisting of dimyristoyl phosphocholine (DMPC) lipids, coarse-grained water molecules, and one 10-ring narrow transmembrane nanotube. The six inner hydrophobic nanotube rings are colored white whereas the hydrophilic rings are colored blue. (Right) The lipid tails are shown in yellow and the head groups in red, purple, and green. The water is colored in blue. [80]

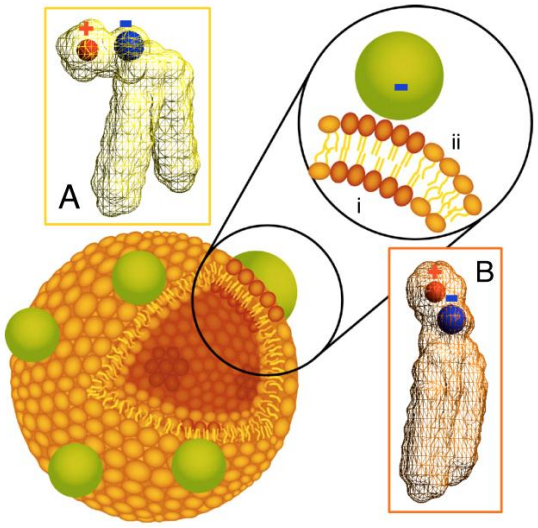

Figure 1-17 Schematic of a phospholipid bilayer vesicle with bound NPs. Binding of anionic NPs to a lipid bilayer in the fluid phase causes the NP to template a gel phase in the place where the NP binds. Binding-induced reorientation of the phosphocholine head group causes lipids in the fluid phase to have lower density (A) than in the gel phase (B). In the phosphocholine head group, P- and N+ are denoted by blue and red respectively. [81]

Compared to mere adsorption onto the surface of cell membrane, the translocation through membrane could have a much stronger impact on the biological functions of the cell. Many computer simulation methods have been employed in the study of the penetration of NPs through lipid bilayer. Qiao et al. conducted a comparison study on the interaction of fullerene and its hydroxylated derivative (fullerol, or $C_{60}(OH)_{20}$) with a DPPC bilayer. Their atomistic simulation showed although a pristine fullerene could

easily diffuse into the bilayer through transient micropores and translocate the membrane, while the fullerol molecule could barely penetrate the bilayer. (Figure 1-, Figure 1-) For fullerene, the translocation could further facilitate the formation of micropores, causing the membrane leakage. For fullerol molecules, due to the hydrophilic surface functionalization, they merely got adsorbed onto the surface, decreasing the spacing between the lipid head groups. [82] Wong-Ekkabut et al. simulated the process of fullerene translocation through lipid membranes using a coarse-grained model. The energy gain of transferring fullerenes into a dioleoylphosphatidycholine (DOPC) or dipalmitoylphosphatidylcholine (DPPC) bilayer made it favorable for the translocation, even for fullerene clusters. After the penetration, clusters disaggregated inside the bilayer quickly. The penetration of fullerenes induced small distortions in the structure and some increase in membrane fluidity. (Figure 1-) Their results suggested membrane damage due to such penetration was unlikely to occur.[83]

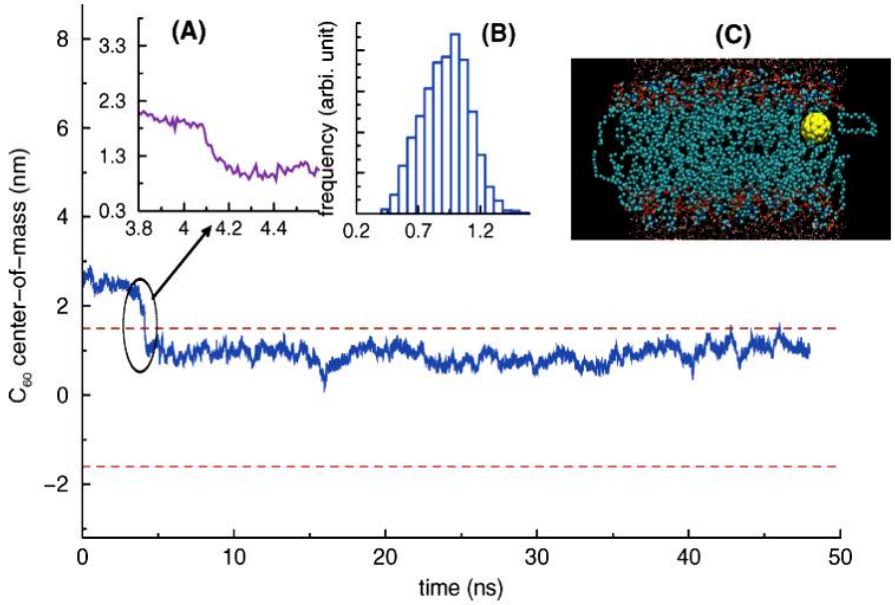

Figure 1-18 Trajectory of the C_{60} molecule in the transmembrane (z) direction. The two dashed lines denote the locations of density peaks of the upper and lower leaflet of the DPPC bilayer. (A) Zoomed view of the trajectory at t=4.09 ns. (B) Histogram of the z-coordinate of the center-of-mass of C_{60} molecule after the buckyball enters the bilayer (t > 4.2 ns). (C) Side view of the simulation system at t=34.5 ns. The yellow ball denotes the C_{60} molecule, cyan dots denote the lipid tail groups, and the red and blue dots represent the lipid head groups. [82]

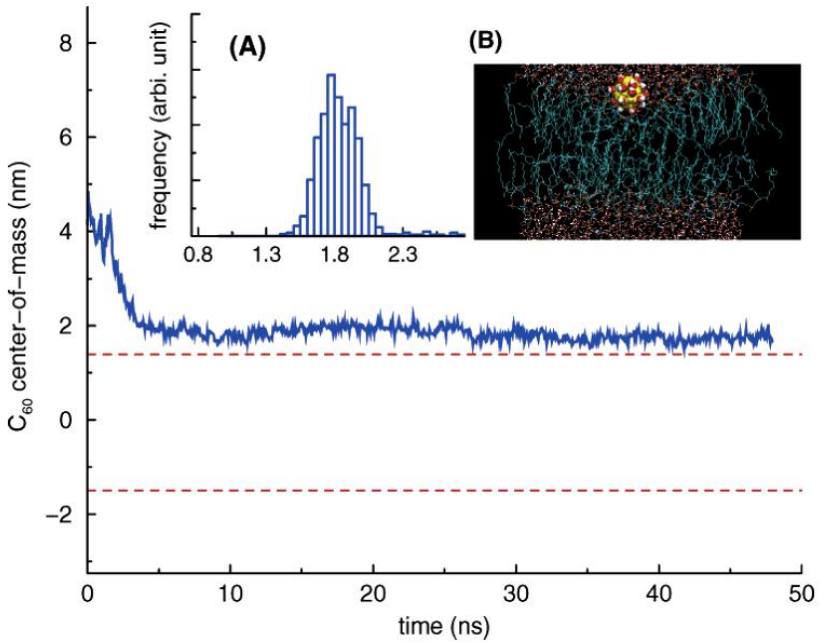

Figure 1-19 Trajectory of the $C_{60}(OH)_{20}$ molecule in the transmembrane (z) direction. The two dashed lines denote the location of density peak of the upper and lower leaflets of the DPPC bilayer. (A) Histogram of the z-coordinate of the center-of-mass of $C_{60}(OH)_{20}$ molecule during simulation. (B) Representative side view of the simulation system. Yellow balls and the attached large red and white dots denote the $C_{60}(OH)_{20}$ molecule, cyan dots denote the tail groups of the DPPC lipids, and the small red and blue dots denote the lipid head groups. [82]

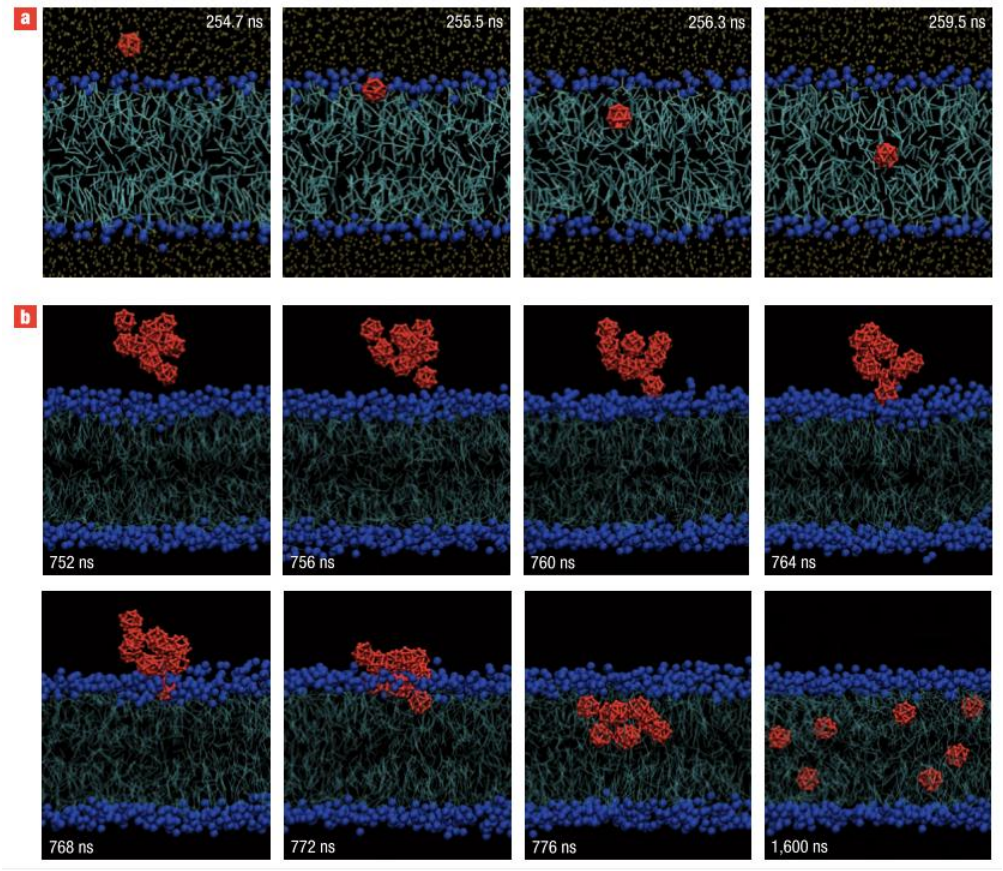

Figure 1-20 a, Monomeric fullerene rapidly crosses the lipid head group region, and then diffuses more slowly in the membrane interior. Fullerene is shown in red, the lipids in cyan with blue head groups (phosphodiester groups), and water is yellow. The simulation time is indicated in each snapshot. b, Penetration of a cluster of ten fullerenes. Lipid phosphodiester groups are shown as blue spheres, lipid tails as cyan lines; water is not represented. The permeation of fullerene clusters is much slower than for monomers, and starts with the insertion of a single fullerene in the lipid head group region. The simulation time is indicated in each snapshot. [83]

Experimentally, Zupanc et al. studied the interaction of fullerene with lipid vesicle membrane. After incubation of palmitoyloleoylphosphocholine (POPC) giant unilamella vesicles, rupture was observed for nearly 2/3 of the vesicles within 10 min, probably due to changes of the average mean curvature of the lipid membrane caused by the adsorption of the fullerene. Disturbances of the lattice order of multilamella vesicles were observed only after vigorous freeze and thaw cycles. In addition, they discovered such effects on lipid membranes were independent of lipid peroxidation, implying the latter possibly only occurs at later stages of membrane damage. [84] The interaction of dendrimers with biological membrane has been of interest since such polymeric NPs have been employed or shown great potential in drug delivery or environment remediation. For example, Hong et al. studied the interaction between positively charged (amine terminated) generation 7 (G7) polyamidoamine dendrimers and lipid bilayers. Their atomic force microscopy (AFM) measurement revealed that the dendrimers caused formation of nanoscale holes of 15 and 40 nm, hypothetically due to electrostatic interactions and formation of dendrimer-nulceated lipid vesicles, while carboxylate surface functionalized dendrimers reduced the hole-formation because of their negative charge; instead they expanded the size of pre-existing defects in the membrane. [41] Neutral dendrimers (capped with acetamide) caused neither hole-formation nor defect-expansion due to the absence of electrostatic interactions. This study further showed pore formation on live cells was also surface chemistry dependent: amine-terminated G5 dendrimers caused a much more significant leakage for both KB and RAT2 cells than acetamide-terminated ones.

Endocytosis of NPs

The physicochemical interactions between NPs and cell membranes are essential for the understanding of the onset of cellular response to the presence of NPs. However, various biological activities are also involved, such as receptor recognition of ligands on the NP surfaces, and endocytosis and exocytosis of NPs. Endocytosis, as one of the major pathways of cellular trafficking of molecule or particles from the extracellular environment, involves dynamic and spontaneous membrane and cytoskeleton activities rather than passive diffusion controlled by the gating mechanism. Endocytosis is present in all types of cells across the body and essential for polar macromolecules such as proteins, growth factors, hormones to pass through the amphiphilic cell membrane, which have to be carried through membrane-bound vesicles produced by invagination and pinching-off of the cell membrane. [85] Endocytosis through different mechanisms generally falls into two categories: phagocytosis (cell eating) and pinocytosis (cell drinking). [86], [87] Specifically, phagocytosis is a cellular process of engulfing solid particles, such as bacterial, yeast or large debris of dead cells by cell membranes, and is only seen in highly specialized cell types, including macrophages, monocytes, dendritic cells, mast cells, and neutrophils, usually well regulated by specific cell-surface receptors and signaling mechanisms that trigger an actin folding-initiated process of cell-surface extending and wrapping around the antibody-coated particles. Phagocytosis is considered as a crucial part of immunological activity against and inflammatory response to foreign pathogens, it could also play an important role in the immune response to the exposure of

NPs, and is currently of great interest for the understanding of the fundamental mechanisms of nanotoxicity by both immunologists and toxicologists. The study of the interaction of NPs with phagocytes could benefit the understanding of inflammatory symptoms manifested on the whole organism level when the subject is exposed to toxic NPs. Pinocytosis, on the other hand, is the fluid-phase uptake from the extracellular space into the cell, commonly found in all cell types, including macropinocytosis, clathrin-mediated endocytosis, caveolae-mediated endocytosis, and clathrin- and caveolae-independent endocytosis. The schematic illustrations of those different types of endocytosis, typical sizes of their endocytic vesicles, and the nature of their cargo are shown in Figure 1-11. Macropinocytosis, similar to phagocytosis, is also caused by membrane protrusion driven by the folding of actin to form generally large volume of endocytic vesicles. The initiation of macropinocytosis could be stimulated by signaling molecules such as growth factors, but is nonspecific in the substance that it takes in. For clathrin-mediated or caveolae-mediated endocytosis only specific substance that is targeted at is engulfed, since the processes of both are initiated by the recognition of a specific ligand on the target by the receptors present at the endocytic pit on the cell membrane. Clathrin-mediated endocytosis is facilitated by the bending of membrane and formation of clathrin-coated endocytic vesicles. While in caveolae-mediated endocytosis, the bending of membrane is caused by caveolin, a dimeric protein that binds to cholesterol. Due to their initiation by highly specific binding between the receptors on the endocytic pit and the ligands on the target, clathrin- and caveolae-mediated endocytosis are utilized in transporting specific materials that the cells need, such as LDL, transferrin,

and growth factors antibodies, etc. Such specificity allows endocytosis to be employed in highly controlled and targeted delivery.

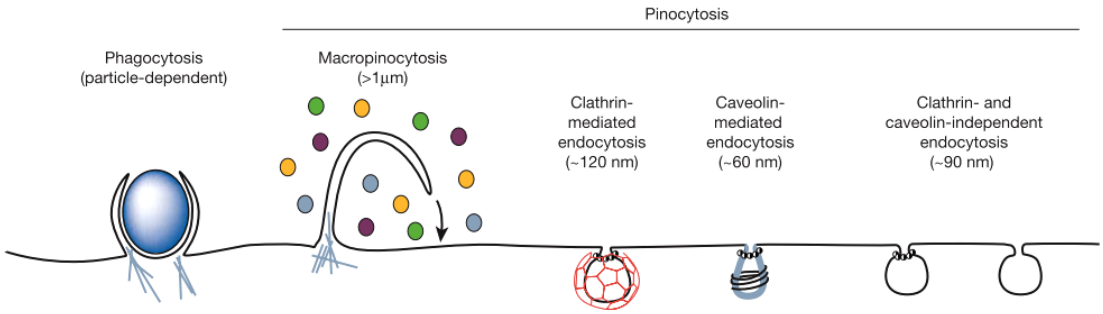

Figure 1-11 Multiple portals of entry into the mammalian cell. The endocytic pathways differ with regard to the size of the endocytic vesicle, the nature of the cargo (ligands, receptors and lipids), and the mechanism of vesicle formation. [86]

A number of studies have been conducted to reveal the different cell uptake mechanisms for NPs. Kim et al. showed that poly(methoxypolyethyleneglycol cyanoacrylate-co-hexadecylcyanoacrylate) (PEG-PHDCA) NPs were internalized through clathrin-coated pit dependent and LDL-receptor-mediated endocytic pathways by rat brain endothelial cells. [88] Their experiments demonstrated that PEG-PHDCA NPs could be recognized by LDL-receptor at the external surface of the cell membrane to form a complex, and then such complex was internalized through clathrin-coated pit formation. Subsequently, the LDL-receptor was recycled and the NPs were transferred to endosomes/lysosomes. Verma et al. revealed the connection between cell internalization

and surface geometry of the NPs. They found that NPs with homogeneous and unstructured surface were internalized primarily through energy-dependent endocytosis, while those with structured surface were able to directly penetrate through cell membrane at low temperature when cellular activities such as endocytosis were inhibited. [89]

While endocytosis of NPs has attracted much attention from researchers in various areas because of its high relevance for drug delivery, bioimaging, and nanotoxicology, the aspect of exocytosis of NPs has been rarely documented. Exocytosis is essentially an opposite process of endocytosis, in which the cell prepares the substance to be exocytosed in a vesicle, and transports the vesicle through a cytoskeletal track to the vicinity of cell membrane, and finally fuses the vesicle with the membrane and releases the contained substance to the extracellular space. During exocytosis, the phospholipids that are consumed by endocytosis can be recovered back to the cell membrane, and the balance between these two cellular biological processes is extremely important for the maintenance of membrane fluidity and cell volume. [90–93] It should be pointed out that both endoxytosis and exocytosis constitute the major aspects of the cell response, as described in more detail in Chapter 3 of this dissertation.

NP-biomolecule interactions and surface-modification of NPs

Upon their entrance into bio or ecological systems, nanomaterials first encounter various biological or organic macromolecules residing in those systems. For nanomaterials disposed to the environment, they may interact with NOM to impose impact on aquatic and soil organisms. [23], [94–96] For NPs used in biomedical

applications, they may interact with the body fluid such as blood, [97–102] gastric mucus, [103], [104] or pulmonary surfactant lipids [105], [106] before they are taken up by the tissues or cells. The interactions between nanomaterials and biological macromolecules could alter or impair the normal functionality of the molecules; for example, the binding of proteins to NPs could induce changes in the secondary structures of the proteins and thus affect the stability and folding of the proteins; also the binding to the unfolded proteins to membrane receptors could lead to immune response of the cell.

Depending on the physicochemical properties of both the NPs and the proteins, the mechanisms for their binding range from vdW force, hydrophobic interaction, electrostatic, to π-stacking and hydrogen bonding. The vdW force is a short-range interaction which decreases rapidly as the participating atoms moving away from each other. The vdW foce between two atoms is usually very weak, however a large contact area sometimes can be accomplished through the deformation of the proteins; thus the vdW force can be drastically enhanced. On the other hand, the vdW force also tends to maximize the contacting area to suppress the attractive potential energy between the atoms, so the complementary shapes of the NP and proteins can sometimes dictate the affinity of their binding.

Laera et al. discovered using synchrotron radiation circular dichroism (SRCD) that at low nanomolar concentration range, the thermal unfolding temperature of human serum albumin (HSA) decreased 6 ℃ upon its interaction with silver NPs, indicating that HSA was significantly destabilized by the NPs possibly due to a more flexible folded

structure in the presence of the silver NPs even before the protein was thermally unfolded. Such phenomenon was not observed for gold NPs. [107]

For carbon-based nanomaterials interacting with aromatic residue-rich proteins, π-stacking is often observed. The π-stacking is an attractive interaction between aromatic carbon rings, resulting in two most energetically preferred configurations: parallel and T-shaped. It is often observed the aromatic rings of amino acids reside parallel to the aromatic rings of carbon sheets or fullerene cages. [108] Surface curvature was also proposed to be one of the key factors that could affect the affinity between nano-surfaces and proteins. By comparing the interactions of villin headpiece (HP35) with grapheme, carbon nanotube and C_{60}, Zuo et al. concluded that due to the different curvatures, π-stacking interactions between HP35's aromatic residues and grapheme played a major role in the adsorption, which caused the protein to lose most of its native secondary and tertiary structures; while for nanotubes and C_{60} the adsorption was primarily due to the dispersion interaction with HP35's aliphatic side chains. [109] Surface curvature effect has also been studied through comparisons among different sized spherical NPs. Vertegel et al. studied the adsorption of chicken egg lysozyme on silica NPs of various sizes with regard to the secondary structures and enzymatic activities of the protein. They discovered that both the adsorption capacities and secondary structural changes (loss in α-helices) were correlated with changes in NP size and pH, indicating that decreased surface curvature or acidity promoted protein unfolding. These results were in agreement with their enzymatic activity measurement: 40% of the native lysozyme activity was lost when 1/3 of the initial α-helix content remained, and as α-helix content further decreased,

a much sharper loss in enzymatic activity was observed. The authors further proposed that the contact between smaller NPs and proteins was limited, and as a result the presence of the small NPs actually stabilized the protein and promoted retention of their structure and function when compared with larger and less curved particles. [110] However such conclusion should not be overly generalized since the interaction between proteins and a NP surface not only depends on the NP curvature but also the physicochemistries of both the protein and the particle: if the protein is energetically obliged to fully unfold to obtain a maxima contact with the NP, one might observe a greater change in both structure and function.

On a related topic, Wang et al. reported relatively weak interactions between silica NPs and Subtilisin Carlsberg (SC) – a non-specific protease – could significantly alter the conformation and enzymatic activity in a NP-size dependent fashion. In this study, data obtained from a colorimetric activity assay was analyzed using the Michaelis-Menten model, showing an increased Michaelis constant K_m, which indicated the competitive inhibition of enzymatic activity because the NPs could act as a competitor to the substrate, while change in the turnover number k_{cat} suggested a long-term conformational alteration of the enzyme. [111]

Hydrogen bonding (H-bonding) is another key intermolecular force involved in nanparticle-protein interaction because of the abundance of hydrogen donors and acceptors on the protein surface. It was reported that H-bonding between NPs and proteins could inhibit protein-protein interaction, including polymerization of protein complexes by their monomers or dimers. Ratnikova et al. reported that the presence of

fullerol inhibited microtubule polymerization *in vitro* even at low micromolar concentrations, as indicated by shortened microtubule length and decreased release of inorganic phosphates. Such inhibition was attributed to the formation of hydrogen bonding between the fullerols and the tubulin heterodimers as shown by docking and MD simulations. This study also showed loss in α-helix content of the tubulins as a result of their interaction with the fullerols. [53]

Another major component in protein-NP interaction is hydrophobic interaction, which is an entropic-driven effect originating from the ability of water molecules to cage nonpolar surfaces. In aqueous solution, most biomolecules form such structures that their hydrophobic moieties are hidden from water, and their hydrophilic components are present at the surfaces. Most NPs entering a biological system possess partially hydrophobic surfaces, including the NPs with hydrophilic surface coating that is usually incomplete. The hydrophobic interactions between proteins and NPs tend to either integrate the NP to the hydrophobic core of the protein, or unfold the protein to expose its hydrophobic residues. Through large-scale MD simulations of different proteins binding with SWCNTs as representatives of hydrophobic NPs, Zuo et al. demonstrated the SWCNTs could plug into the hydrophobic core of the proteins forming stable structures. Such binding completely disrupted and blocked proline-rich peptide motifs (PRM) active sites and inhibited the direct binding between the PRM and the WW domain (containing two highly conserved tryptophan residues, critical for protein function), and further resulted in a loss of the original function of the WW domain. Based on these observations, the authors further suggested that the toxicity of nanomaterials or the “poisoning” of the

proteins originated from their mutual interactions on the molecular level. [112] Ge et al. compared the adsorption of different plasma proteins, namely bovine fibrinogen (BFG), Immunoglobulin G (IgG), transferrin (Tf), and BSA onto SWCNTs, and found the amounts of adsorbed proteins were correlated with the protein molecular weight and the abundance of hydrophobic or aromatic residues, including tyrosine (Tyr), phenylalanine (Phe), and tryptophan (Trp) in the protein. (Figure 1-12) This study also presented a MD simulation to show π-stacking between the aromatic rings in the protein and the hexagons on the curved carbon sheets. [113]

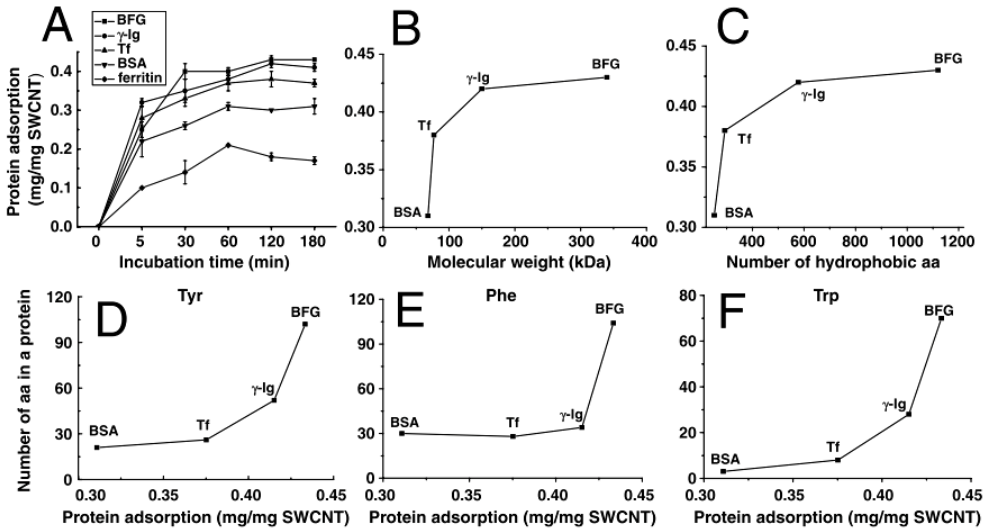

Figure 1-12 Adsorption kinetics and the main factors controlling the protein adsorption on SWCNTs. (A) Kinetics curves of protein adsorption on SWCNTs. The positive correlations between protein adsorption capacity and protein molecular weight (B) or the number of hydrophobic amino acids (aa) (C). The positive correlations between protein adsorption capacity and the number of Tyr (D), Trp (E), and Phe (F). The total numbers

of (Trp, Tyr, Phe) residues are (70, 102, 104) in BFG; (28, 52, 34) in Ig; (8, 26, 28) in Tf; and (3, 21, 30) in BSA, respectively. [113]

The interaction between a protein and a NP not only alters the structure and function of the protein, it also causes protein adsorption onto the NP to alter the physicochemistry of the latter. A large number of proteins adsorb onto the surfaces of NPs due to their high binding affinity, forming either a loose (soft) or a condensed (hard) layer(s) of surface coating that is termed as a "protein corona". Such concept sometimes is expanded to the surface coating of NPs by biological molecules in general, including proteins, lipids, peptides, and nucleic acids, known as "biocorona", which literally defines the biological identity of the particles and determines how the cell sees them. The existence of such corona as an entity of multiple biomolecules encasing a NP "core" can be dynamic within the biological context: the biomolecules constantly exchange with other nearby molecules, the residing time of the biomolecules depends on their binding affinity for the NP surface, interactions among the biomolecules, as well as thermal dynamics of the ensemble. The simplest thermal dynamical model of biomolecule (M)-NP (NP) interaction can be expressed as: [114]

$$M + NP \underset{k_{off}}{\overset{k_{on}}{\rightleftharpoons}} M - NP, \text{ and } K_d = \frac{[M][NP]}{[M-NP]} = \frac{k_{on}}{k_{off}},$$

where k_{on} is the on-rate, k_{off} is the off-rate, and K_d is the dissociation constant. The brackets denote the equilibrium concentrations. Such interactions may be classified as either weak or strong, based on the magnitude of K_d. A weak binding ($K_d > 10^{-4}$ M) is

usually nonspecific, while a strong binding is typically specific such as ligand-receptor recognition. It is worth noting that this simple model is based on single protein-single particle interaction, while in a biological environment that is crowded with abundant biomolecules of extremely high concentrations even weak binding molecules still are able to coat the NP surface. Hence by comparing the thermal dynamics associated with different NPs (material, size, surface coating, and charge, etc.), one can achieve optimal interactions between the NPs and their host systems.

The thermal dynamics of biomolecule-NP interaction or biocorona formation can be studied, in principle, by isothermal titration calorimetry (ITC). In ITC measurements, the heat exchange is accurately detected during each injection, and the thermal dynamic parameters can be calculated using different binding models. Cedervall et al. characterized the stoichiometric ratio of the binding between HSA and N-*iso*propylacrylamide (NIPAM): N-*tert*-butylacrylamide (BAM) copolymer NPs with different sizes. Their calorimetric results showing the binding was an exothermic process, indicating the binding was spontaneous and energetically favorable. Larger stoichiometric ratios of proteins to NPs were obtained for more hydrophobic or larger particles, indicating that the number of adsorbed protein molecules was correlated with surface hydrophobicity and size. [115] Baier et al. also acquired enthalpy, stoichiometric ratio, and binding constant through ITC measurement of the interaction between BSA and NIPAM: BAM particles with different coatings, and found that the pH of the solvent also played an important role to invoke protonation or deprotonation of the nanopaticle

surface coating, thus modulating the electrostatic interactions between the NP and the proteins.[116]

Even for already formed protein corona, such structure is still highly dynamic and is subject to constant exchange with the proteins in the surroundings, a phenomenon known as the Vroman effect. [117], [118] Vilaseca et al. simulated the adsorption of various plasma proteins, including albumin, immunoglogbulin-γ and fibrinogen onto a glass surface. Their results indicated that the Vroman effect was a consequence of the different mass, size, shape, and affinity of the proteins. Such properties govern the diffusive behavior of the proteins and their interactions with the NP surfaces, which led to a competitive adsorption process that had different proteins residing sequentially on the NP surface and replacing each other until the structure was equilibrated.[119] Dell'Ocro et al. proposed a simple and effective mathematical model to derive the kinetics of corona formation around a copolymer NP. Their results showed that HSA was initially bound to the NP due to its higher abundance in the plasma, but soon was replaced by the higher-affinity and slower-exchanging apolipoproteins. In addition, the binding between high density lipoprotein (HDL) and the particle was much stronger than the rest, likely due to the specific binding between the NP and apolipoprotein A-I, a major component of the HDL.[120]

The Vroman effect is dynamic and evolves when NPs are exposed to different types of biological fluids to introduce a sequential exchange between the bound and free proteins or other biomolecules. When NPs enter an organism, naturally they translocate from one subsystem to another within the organism. For example, it was observed the

NPs penetrated gastric mucosa to enter the gastric tissue or bloodstream, [103], [104] or were taken up by cells from the bloodstream. Thus, understanding the evolution of pre-formed NP-protein corona in different biological fluids is essential for describing the complex behaviors of NPs within biological systems. Lundqvist et al. studied the dynamics of protein corona as a result of transferring NPs from the plasma into the cytosolic fluid to mimic the uptake of the particles by the cell from the bloodstream. Their sodium dodecyl sulfate (SDS)-polyacrylamide gel electrophoresis (PAGE) gel patterns clearly showed that the protein corona pre-formed with plasma proteins in equilibration became significantly altered in original composition after their incubation with the cytosolic fluid, and their proteomics analysis indicated some of proteins present in the plasma protein corona were replaced by, for example, apolipoprotein A-I.[121]

"Hardening" is another phenomenon that is associated with NP-protein corona. Casals et al. observed a time evolution toward a denser dielectric coating of AuNPs after their incubation with the cell culture medium, as indicated by a shift in the NP SPR peak, as well as time-dependent changes for up to 48 h in protein corona size and zeta-potential analyzed by dynamic light scattering. Also, the BSA-specific antibody induced a size increase while the BSA content in the corona remained in its native state rather than denatured. [122] In a following study, the authors expanded the time for incubation with serum-containing cell culture medium up to 38 days, and included both metal (Au, Ag) and oxides (Fe_3O_4, CoO, and CeO_2) particles. The results from their size, zeta-potential, and SPR shift measurements indicated that a saturation of adsorption was reached after 30 days and desorption of the proteins did not occur after the particle-protein corona was

resuspended in water. This study suggests that a dynamic or "soft" protein corona eventually evolves into an irreversibly "hard" corona over time. *In vitro* experiments by these researchers further revealed that such a "hard" corona defined the biological identity of the NP in terms of cell recognition and response: ROS production by acute monocytic leukemia cell line (THP-1) cells in the presence of CoO-protein corona was much reduced compared with pure CoO particles, possibly because the particle itself was shielded from the cell by its surface coating, which was far more biocompatible. [123] In a previously mentioned study, [113] Ge et al. discovered the cellular response of THP-1 and human umbilical vein endothelial cells (HUVECs) to protein-coated SWCNTs largely depended upon the competitive binding of blood proteins, and the bound proteins could greatly alter their interaction pathways and reduce cytotoxicity according to their respective adsorption capacity. Especially for BFG, which had the largest binding capacity for SWCNTs due to the abundance of hydrophobic/aromatic residues, the toxicity was almost completely eliminated for both cell types.

CHAPTER 2. DIFFERENTIAL UPTAKE OF CARBON NANOPARTICLES BY PLANT AND MAMMALIAN CELLS

Understanding the biological and environmental impacts of nanomaterials has recently become a focused research area worldwide. Emergence of this new field is driven by the crucial need for developing safe nanotechnologies without compromising human health and environmental sustainability[124–126]. Fundamental to this inquiry is the interaction of NPs and living systems[127], whose underlining mechanisms are little understood. In chapter 2, we show a direct comparison of fullerene uptake by plant and mammalian cells. We demonstrate that the presence of a plant cell wall and solubility of the fullerene play central roles on NP uptake and cell damage. Specifically, fullerene C_{70} suspended in NOM [23], [94] exerted no damage to *Allium cepa* plant cells, while water-soluble $C_{60}(OH)_{20}$ increasingly impaired plant cell viability with concentration up to 70 mg/L. These trends were reversed in HT-29 mammalian cells, however, where C_{70}-NOM induced increased cytotoxicity at higher concentrations while $C_{60}(OH)_{20}$ showed no effect on cell morphology.

2.1 Introduction

It has been realized by the scientific community that understanding the fate of nanomaterials from cradle to grave is essential to the sustainability of nanotechnolgy.[126] Consequently, a body of literature over the past decade has been centered on cytotoxicity, genotoxicity, and ecotoxicity of nanomaterials, pointing to the general understanding that nanotoxicity is often derived from the physiochemical

properties of the nanomaterials and their interplay with the host environment.[11], [23], [56], [64], [67], [69], [70], [81–83], [94], [128–142] However, while biological and ecological systems constantly interact and are integrated in the network of nature, it remains a new challenge to evaluate and correlate the biological and environmental impacts of NPs within the same context.[126], [127] Here we present a first parallel study of carbon NP uptake by plant and mammalian cells. Specifically, *Allium cepa* and HT-29 human colonic adenocarcinoma cell lines were used as model plant and mammalian systems, and were exposed to different doses of fullerene C_{70} suspended in NOM and fullerol $C_{60}(OH)_{20}$, a water-soluble fullerene derivative. The use of NOM, a collection of heterogeneous organic substances from decomposed living species, is justified because of its abundance in the natural water sources and soil and its likelihood to interact with discharged NPs.[23], [94] Using microscopy and a plant viability assay we show that variations in NP size and hydrophobicity as well as structural differences between plant and mammalian cells underlie NP-cell interaction and cell damage.

2.2 Materials and Methods

NP suspension preparation and characterization:

C_{70} (SES Research, purity: 99%), $C_{60}(OH)_{20}$ (BuckyUSA), and Nordic NOM (IHSS) were used as purchased. C_{70}-NOM stock suspension of 1,000 mg/L was prepared using the same protocol described previously.[23] $C_{60}(OH)_{20}$ was dissolved directly into Milli-Q to obtains a stock suspension of 1,000 mg/L. The NP suspensions were diluted in

Milli-Q at concentrations of 10-110 mg/L and their UV-vis absorbance was measured using a Biomate 3 spectrophotometer. The signature wavelengths of C_{70}-NOM and $C_{60}(OH)_{20}$ were located at 400 nm and 252 nm, respectively. The stability of the suspensions was observed by measuring the absorbance at their signature wavelengths over 9 h (Figure 2-2 and Figure 2-3). Ultracentrifugation (10,000 RCF, 5 min) was applied to the more stable $C_{60}(OH)_{20}$ suspension to characterize its aggregation at high concentrations (Figure 2-3). The size distributions of C_{70}-NOM and $C_{60}(OH)_{20}$ suspensions were measured using a NanoSizer S90 (Sections 1C and 1D) and their zeta potentials were read using a ZetaSizer Nano ZS.

Plant cell preparation, examination and data analysis:

Allium cepa samples were obtained from produce quality onion bulbs. Storage leaves of area 1 cm^2 were removed, and laminar cells were collected from the inner layers of the plant tissue. Samples were immersed in $C_{60}(OH)_{20}$ and C_{70}-NOM suspensions to obtain final concentrations of 10-110 mg/L in MS buffer (pH = 6) [23] (Higher concentrations introduced significant aggregation, especially for C_{70}-NOM, and therefore were not included for the current study). After 9 h incubation and gentle shaking the samples were washed in MS buffer prior to the addition of a plant cell viability assay (Sigma). A stock solution of the viability assay contained 1% of propidium iodide (PI) and an equal amount of fluorescein diacetate (FD) in MS buffer. Each sample was incubated with 14.29% of the stock solution (total volume 400 μL) for 5 min before imaging with a Zeiss A1 microscope. Each data point was sampled from an area of approximately 8 mm^2, which contained an average of 303 onion cells. Twenty data

points, corresponding to approximately 6,000 cells, were collected for each concentration used. Fluorescence images were taken from the FITC (for FD emission) and Rhod (for PI emission) channels. Damaged cells showed orange fluorescence (peak at 620 nm) in the nuclear region when viewed under the Rhod channel. Data points were taken only for areas on the interior of the sample to exclude artificial damage due to handling. Significant difference from the control was examined using a student *t*-test. Statistical significance was accepted when the probability of the result assuming the null hypothesis (p) is less than 0.01.

Transmission electron microscopy (TEM) imaging of Allium cepa:

For TEM imaging, thin layers of *Allium cepa* cells were fixed in 3.5% glutaraldehyde overnight and dehydrated in a graded series of ethanol. The dehydrated samples were then embedded in LR white resin overnight at 40 ℃ and sectioned into thin films approximately 200 nm thick using an Ultracut E Microtome. No osmium tetroxide was added in order to eliminate the introduction of artifacts. TEM images were acquired using a Hitachi H7600 microscope operated at 80 and 100 kV. The lattice structures of C_{70}-NOM and $C_{60}(OH)_{20}$ were captured using a Hitachi H9500 microscope operated at 150 kV. The lattice spacings of the NPs in *Allium cepa* were analyzed by performing Fast Fourier Transform (FFT) of the TEM images, using "Diffractogram" software.

HT-29 cell culture and confocal imaging:

HT-29 human colonic adenocarcinoma cell lines were cultured in Dulbecco's Modified Eagle's Medium (DMEM) with 1% penicillin streptomycin, 1% sodium pyruvate, and 10% fetal bovine serum. Approximately 5,000 HT-29 cells were seeded in each well (200 μL) of an eight-chamber glass plate and allowed to attach overnight at 37℃ with 5% CO2. After the cells reached a 60% confluence C_{70}-NOM and $C_{60}(OH)_{20}$ were added in each chamber glass well to obtain final concentrations of 10, 30, 50, 70, 90 and 110 mg/L. After 9 h incubation, the cells were thoroughly rinsed three times using PBS buffer to remove dead cells and un-bound NPs. An Argon laser of 488 nm was used as an excitation source for confocal imaging (LSM510, Zeiss), and 10 images (900×900 μm) were acquired for each sample condition using a 10× objective. The images were then analyzed and the cells of each sample were counted using LSM Image Browser.

2.3 Results and Discussion

Fullerene C_{70} was dissolved in aqueous NOM solution to self-assemble into C_{70}-NOM. Fullerol $C_{60}(OH)_{20}$ was directly dissolved in Milli-Q water. The structures of C_{70}-NOM and $C_{60}(OH)_{20}$ are illustrated in Figure 2-1. The solubilities of the NP suspensions were characterized (Figure 2-2 and Figure 2-3), with C_{70}-NOM showing an ~30% precipitation and $C_{60}(OH)_{20}$ showing no precipitation over 9 h incubation, for all concentrations. The size distributions of the suspensions were determined using dynamic light scattering, ranging between 18.17-43.82 nm at 10 mg/L and 27.36-100 nm at 110 mg/L for C_{70}-NOM and 1.12-1.74 nm at 10 mg/L and 15.69-24.36 nm at 110 mg/L for

$C_{60}(OH)_{20}$, respectively (Figure 2-4 and Figure 2-5). The larger sizes and broader size distributions of C_{70}-NOM are attributed to the non-covalent binding between the C_{70} aggregates and the inhomogeneous, amphiphilic, and aromatic-rich NOM. Consequently, C_{70}-NOM complexes were heterogeneous and more hydrophobic than the covalent structure of $C_{60}(OH)_{20}$. The surface charges of both suspensions were comparable, with a zeta potential of -34.3 mV recorded for C_{70}-NOM and -42.6 mV for the more stable $C_{60}(OH)_{20}$ (pH = 6.3).

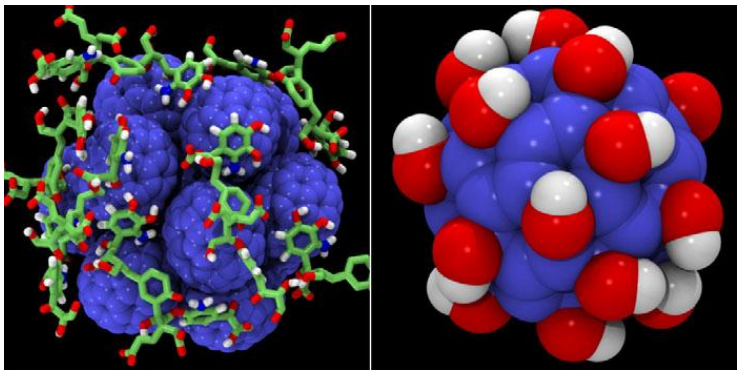

Figure 2-1 Atomistic illustrations of (left) a C_{70}-NOM supramolecular assembly and (right) a single $C_{60}(OH)_{20}$ molecule. In the left panel, the C_{70} molecules are shown in blue, while the heterogeneous NOM molecules are shown in green, red and white based on the Temple-Northeastern-Birmingham (TNB) model.[143] In the right panel, the C60 molecule is shown in blue while the OH groups are illustrated in red and white

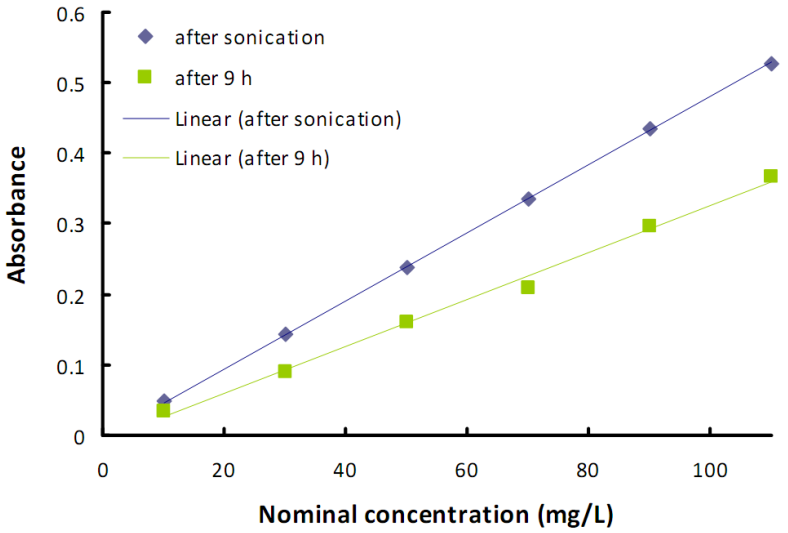

Figure 2-2 Absorbance of C_{70}-NOM vs. nominal C_{70} concentration. (Blue curve) Fresh samples measured immediately after probe sonication. (Green curve) Samples incubated at room temperature for 9 h, as used in all plant and mammalian cell experiments. The decrease in absorbance (green vs. blue) indicates C_{70} precipitation, especially at high concentrations (30.4% at 110 mg/L). Absorbance was measured at 400 nm (Biomate 3).

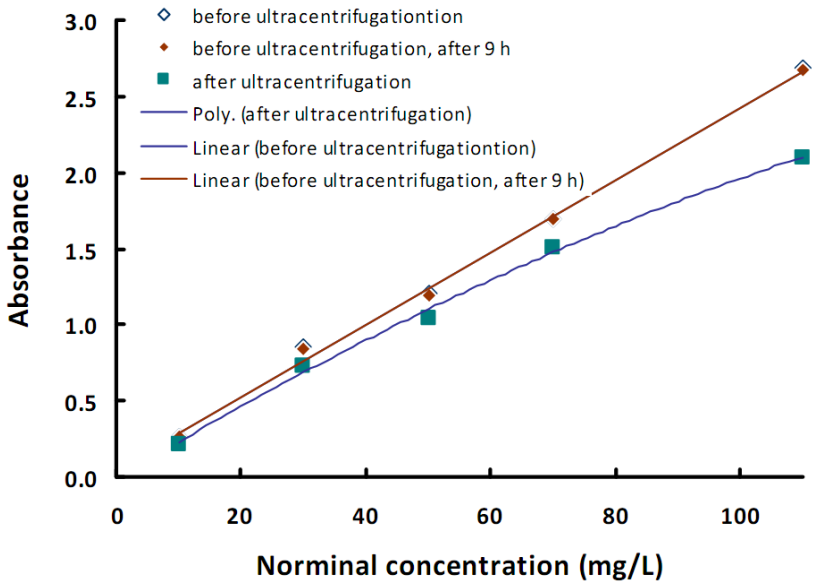

Figure 2-3 Absorbance of $C_{60}(OH)_{20}$ vs. nominal $C_{60}(OH)_{20}$ concentration before and after ultracentrifugation. No significant difference in absorbance was measured for freshly prepared $C_{60}(OH)_{20}$ suspension (hollow diamonds) and after 9 h of storage (solid diamonds) at room temperature, indicating high stability of the $C_{60}(OH)_{20}$ suspension. The bending curve (cyan) after ultracentrifugation (squares vs. diamonds) indicates gradual aggregation of $C_{60}(OH)_{20}$ with increased concentration. Ultracentrifugation: 10,000 RCF, for 5 min (Eppendorf, Centrifuge 5810 R). Absorbance was measured at 252 nm (Biomate 3).

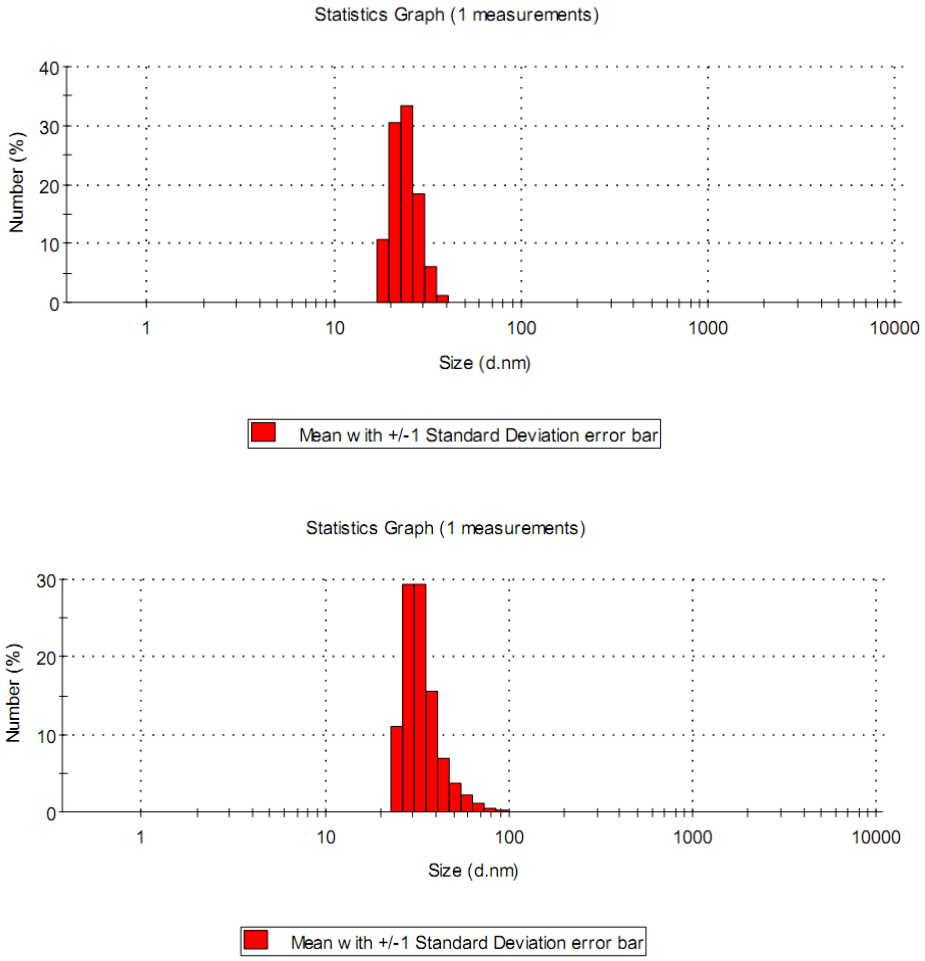

Figure 2-4 C_{70}-NOM size distribution by dynamic light scattering (Nanosizer S90), 10 and 110 mg/L.

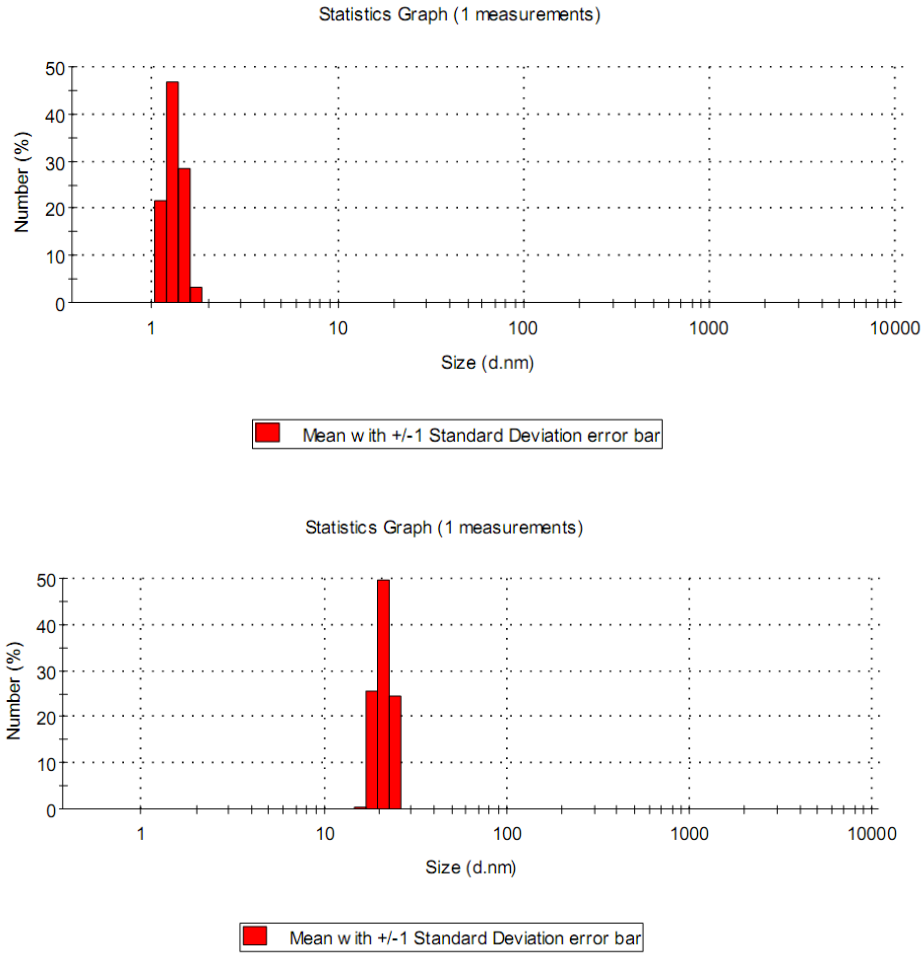

Figure 2-5 $C_{60}(OH)_{20}$ size distribution by dynamic light scattering (Nanosizer S90), 10 and 110 mg/L.

Laminar *Allium cepa* cells were prepared and HT-29 cell lines were cultured to 60% confluence (Experimental Section), which were then incubated separately with C_{70}-NOM and $C_{60}(OH)_{20}$ of 10~110 mg/L, for 9 h. Figure 2-6 shows optical images of *Allium cepa* cell morphology (bright field) and loss of membrane integrity (PI), emission in orange) in the presence of $C_{60}(OH)_{20}$ (Figure 2-6a-f) and C_{70}-NOM (Figure 2-6g-i).

Specifically, more orange fluorescent spots can be seen in Figure 2-6e than Figure 2-6b, indicating increased cell damage with $C_{60}(OH)_{20}$ concentration of 30 mg/L to 70 mg/L. The bright green fluorescence regions in Figure 2-6c, f, and i signify hydrolysis of FD by intracellular esterases, which were indicative of viable cells. The cells shown in Figure 2-6g-i were further treated with mannitol (0.8 M) for 15 min, after their incubation with C_{70}-NOM of 50 mg/L for 9 h. The mannitol gradient across the cell surfaces induced an osmotic pressure, which in turn split plant cell walls from their underlining plasma membranes. C_{70} aggregates were revealed by the osmosis assay as mostly adsorbed on or trapped within the hydrophobic cellulose matrices of the plant cell walls (Figure 2-6i). A comparison between the bright field and fluorescence images shows a good correlation between damaged membranes (orange spots in Figure 2-6b and e), cells of impaired viability (dim green regions in Figure 2-6c and f), and cells of altered morphology (rough cell surfaces in Figures 1a and 1d). The appearances of contagious nonviable cells (regions denoted by red arrow in Figure 2-6c and orange spots in Figure 2-6e) further suggest that upon $C_{60}(OH)_{20}$ uptake cells underwent necrosis, which is typically invoked by abnormal environmental conditions and viruses.

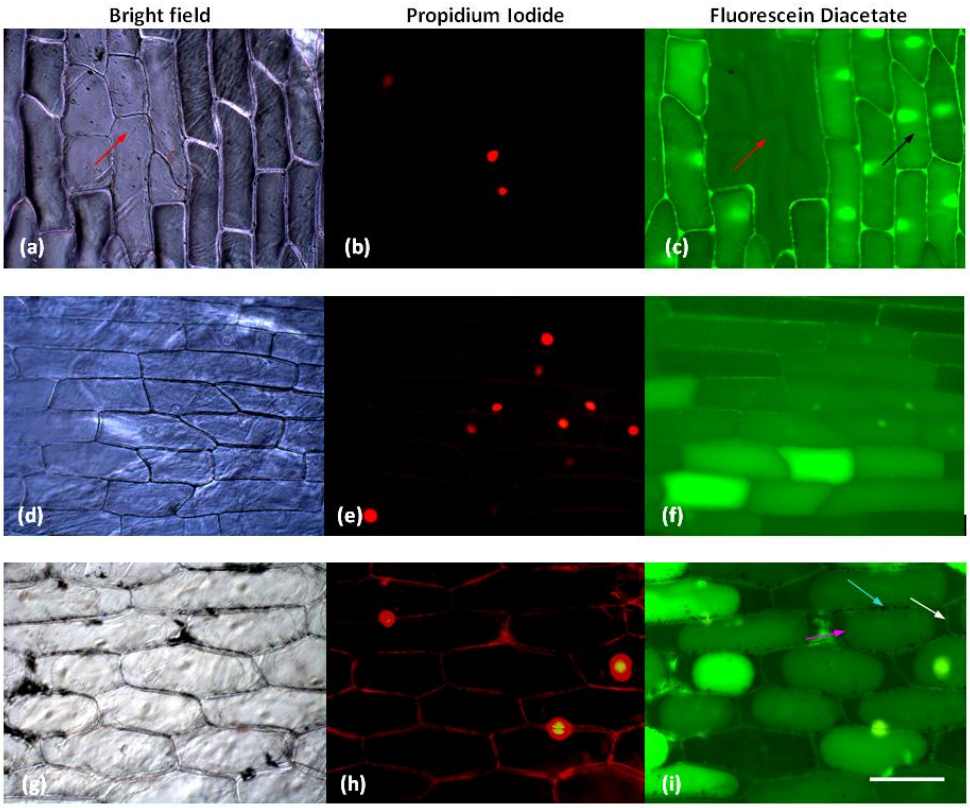

Figure 2-6 Optical imaging of *Allium cepa* plant cell damage in the presence of C_{70}-NOM and $C_{60}(OH)_{20}$. (a-c) Plant cells incubated with $C_{60}(OH)_{20}$ of 30 mg/L for 9 h. (d-f) Plant cells incubated with $C_{60}(OH)_{20}$ of 70 mg/L for 9 h. (g-i) Plant cells incubated with C_{70}-NOM of 50 mg/L for 9 h. Images were acquired using the bright field, Rhodamine (PI), and FITC (fluorescein diacetate) modes. (b, e, h) The orange fluorescence indicates staining of nucleic acids by PI due to loss of cell viability. (c, f, i) The bright green fluorescence indicates hydrolysis of FD by intracellular esterases of viable cells. (a, c) Examples of non-viable (red arrows) and viable cells (black arrow). (g-i) Osmosis procedures were applied to split plasma cell membranes (pink arrow in (i)) from plant cell walls (white arrow in (i)). Aggregation of C_{70} particles is exemplified by the blue arrow in (i). All images are of the same scale (scale bar: 50 μm).

A summary of plant cell damage in the presence of C_{70}-NOM and $C_{60}(OH)_{20}$, each of 10-110 mg/L, is shown in Figure 2-7. The damage was calculated by counting percent of nonviable cells in the PI channel, while the FD channel was used as a reference due to its susceptibility to crosstalk from the PI channel and cell autofluorescence. As shown in the top panel of Figure 2-7, C_{70}-NOM caused a mere 0.8% more plant cell damage than the control at 90 mg/L and 110 mg/L, and no damage at lower concentrations. This phenomenon is attributed to the large size and hydrophobicity of the C_{70}-NOM, which tended to block the porous plant cell wall and form clusters therein through hydrophobic interactions (Figure 2-8b and c, Figure 2-6i). $C_{60}(OH)_{20}$, in comparison, triggered a steady rise in cell damage, causing a maximum 4.7% more damage than the control at 70 mg/L. Due to their small size and good solubility, $C_{60}(OH)_{20}$ readily permeated through the plant cell wall driven by a concentration gradient, and were mostly excluded by the plasma membrane due to their hydrophilicity, mutual electrostatic repulsion, and hydrogen-bonding with water.[82] Under capillary and vdW forces these NPs were confined between the cell wall and the plasma membrane (Figure 2-10a), and accumulate under the concentration gradient to protrude the plasma membrane (Figure 2-8e). Since fullerols—unlike pristine fullerenes—have been shown as relatively inactive in creating ROS,[64] the loss of membrane integrity (Figure 2-6b, 1e) is therefore inferred as a result of mechanical damage exerted by $C_{60}(OH)_{20}$ aggregation. Such damage would impinge on membrane fluidity and the transport of nutrients and ions between the plant cell and its extracellular space, further stressing the physiological state

of the cell and its neighboring cells. $C_{60}(OH)_{20}$ clusters occasionally appeared near the plasma membrane within the cytoplasm (Figure 2-8f and g), likely due to membrane damage and a low-level steady state endocytosis.[144], [145] Although not intended to be a focus in this study, accumulation of $C_{60}(OH)_{20}$ between adjacent epidermal cell walls (Figure 2-10b) further implies that transport of $C_{60}(OH)_{20}$ in the plant tissue was partially conveyed through the apoplastic pathway,[146] whose blockage could also impact on cell viability. The ease of cell damage at 90 mg/L and 110 mg/L (Figure 2-7, lower panel) is attributed to the gradual aggregation of $C_{60}(OH)_{20}$ at these concentrations (Figure 2-3, "after ultracentrifugation" curve; Figure 2-5), which would have hindered NP uptake.

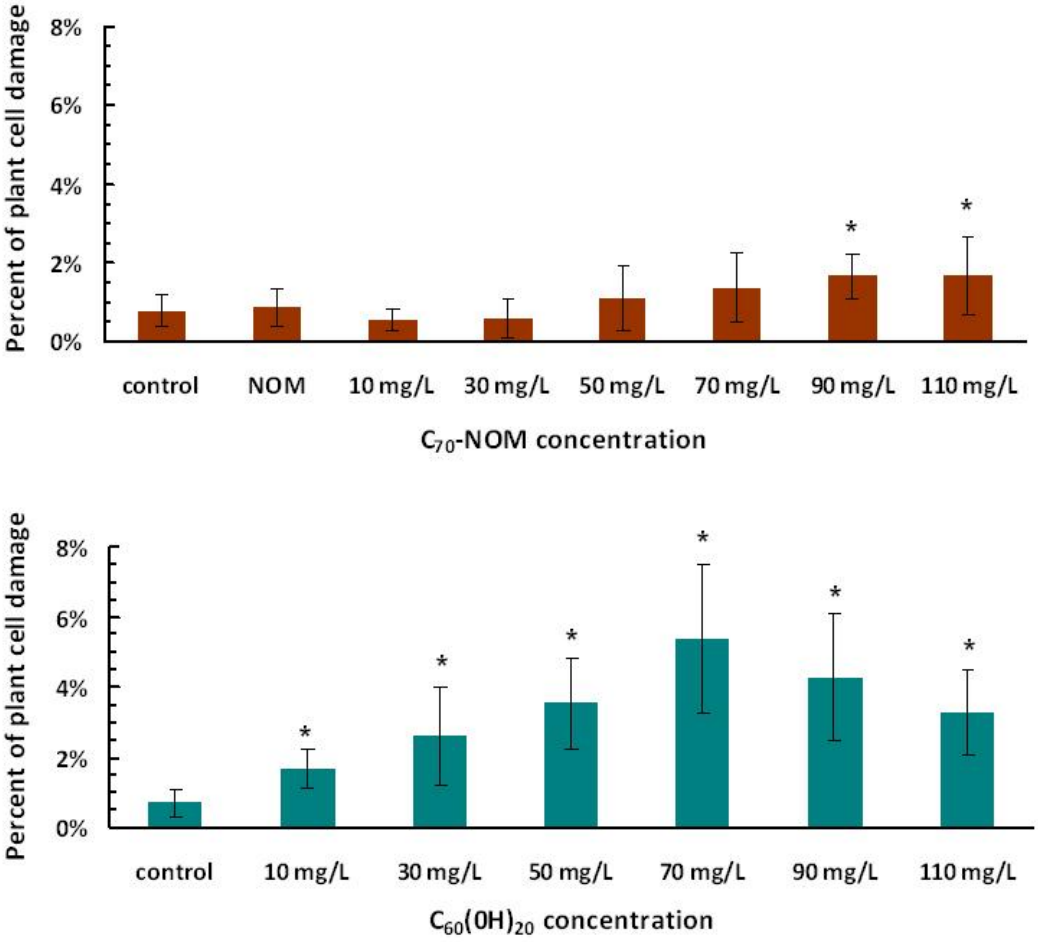

Figure 2-7 Percent of *Allium cepa* plant cell damage in the presence of C_{70}-NOM and $C_{60}(OH)_{20}$ of various concentrations. Incubation time: 9 h. The asterisks indicate data which are statistically different from the control ($p<0.01$). NOM: positive control.

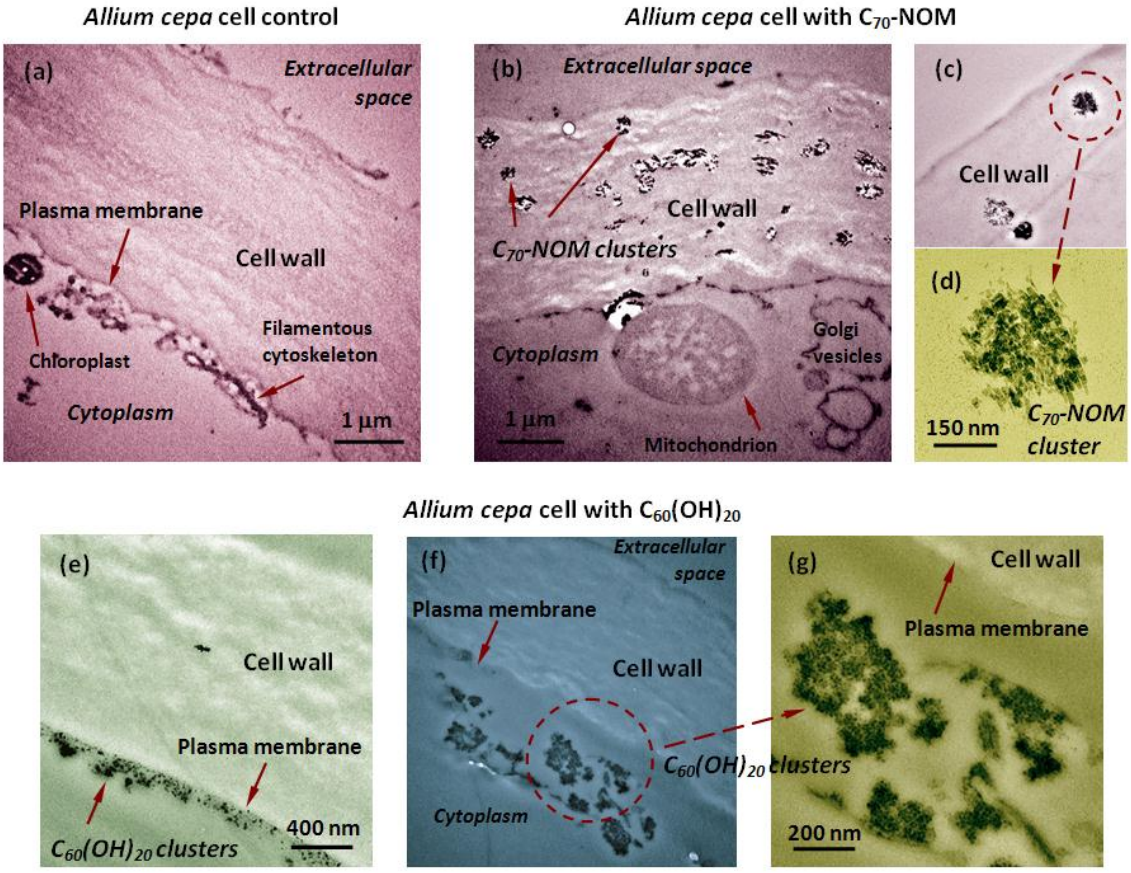

Figure 2-8 TEM imaging of carbon NP uptake by *Allium cepa* plant cells. (a) Control showing plant cell wall and plasma membrane. The cell wall typically bends towards its intracellular space. (b-d) Plant cell walls entrapped with C_{70}-NOM clusters of 50-400 nm. C_{70}-NOM concentration: 50 mg/L. (d) Magnified view of a C_{70}-NOM cluster in (c). (e-g) Translocation of $C_{60}(OH)_{20}$ across plant cell walls. $C_{60}(OH)_{20}$ clusters can be seen (e) near the interface between the plant cell wall and the plasma membrane and (f, g) in intracellular space. $C_{60}(OH)_{20}$ concentration: 50 mg/L. (g) Magnified view of the $C_{60}(OH)_{20}$ clusters in (f). The lattice structures of C_{70}-NOM and $C_{60}(OH)_{20}$ in *Allium cepa* cells are confirmed Figure 2-9.

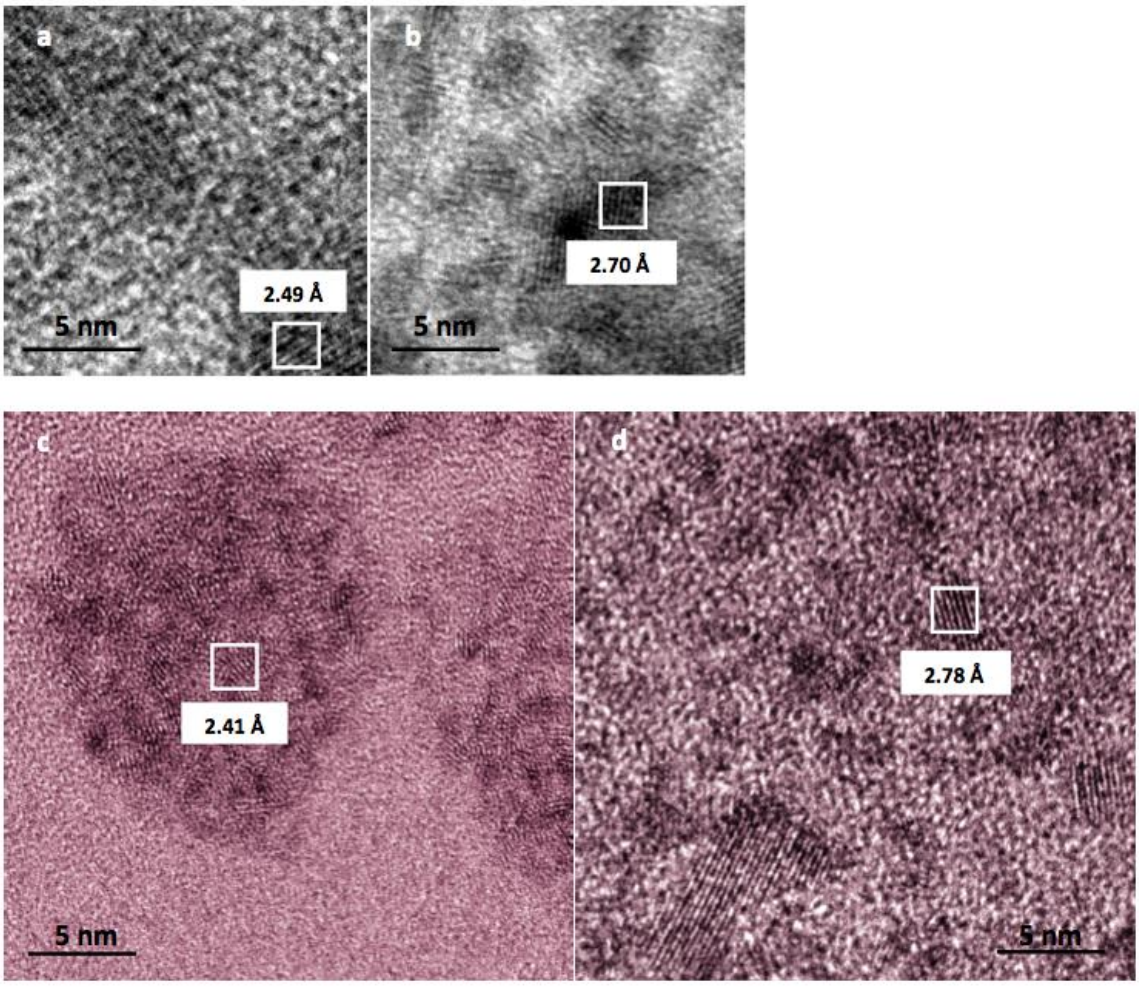

Figure 2-9 High resolution TEM images showing (a) a C_{70}- NOM lattice spacing of 2.49 Å, (b) a $C_{60}(OH)_{20}$ lattice spacing of 2.70 Å, (c) a C_{70}- NOM lattice spacing of 2.41 Å, and (d) a $C_{60}(OH)_{20}$ lattice spacing of 2.78 Å. Images (a) and (b) were obtained from dried NP suspensions, while (c) and (d) were obtained for the NPs in *Allium cepa*.

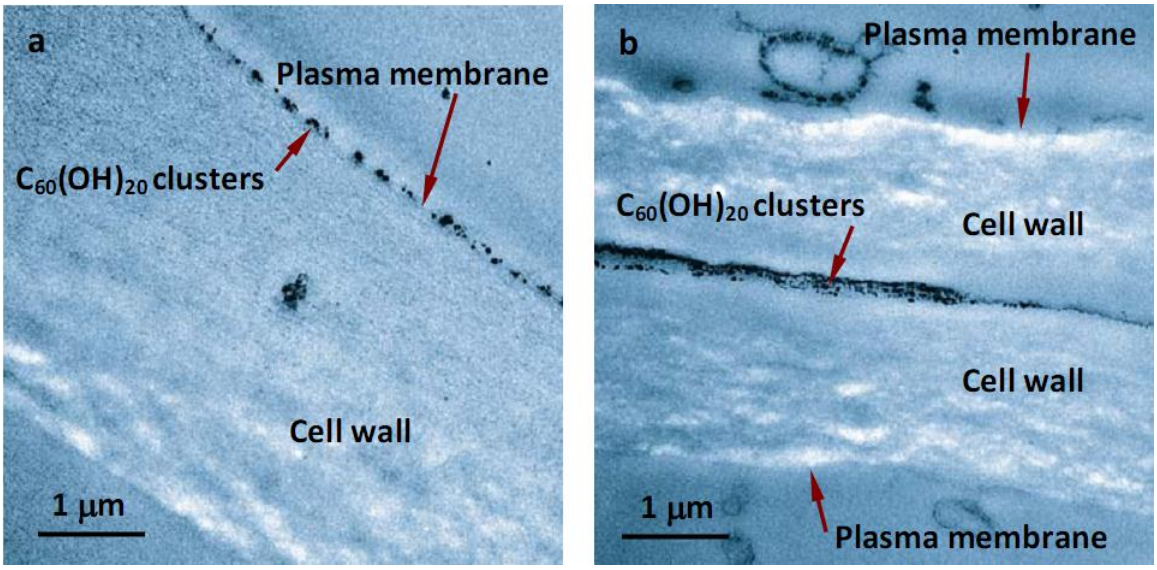

Figure 2-10 (a) Presence of $C_{60}(OH)_{20}$ clusters at the interface between plant cell wall and plasma membrane. (b) Presence of $C_{60}(OH)_{20}$ clusters in the apoplastic pathway between two plant cell walls.

In contrast to the observations made above for plant cells, mammalian cells showed distinctly different responses to the two types of carbon NPs. After 9 h incubation and thorough washing to remove dead cells and unbound NPs, the number/density of viable HT-29 cells decreased continuously with increased C_{70}-NOM concentration up to 70 mg/L, and then leveled off at higher concentrations due to NP aggregation (Figure 2-11 lower panel). The cell morphology also changed from the healthy elongated form to the less viable more spherical shapes at higher C_{70}-NOM concentrations, showing abundant NP aggregates bound to/imbedded in the cell membranes (Figure 2-11 top panels). Cell lysis was visible, likely due to exhaustive

endocytosis Figure 2-11d) and occurrence of necrosis in the damaged cells. By comparison, no cell damage was found for HT-29 cells exposed to $C_{60}(OH)_{20}$ of all concentrations used (Figure 2-12), thus confirming the low affinity of $C_{60}(OH)_{20}$ for mammalian cell membranes. These contrasting damages induced by the noncovalent assembly of C_{70}-NOM and covalent $C_{60}(OH)_{20}$ to HT-29 cells are in good agreement with the *in vitro* study by Sayes et al.[64] and the simulations by Qiao et al.[82], on the cytotoxicities of pristine fullerene C_{60} and fullerol $C_{60}(OH)_{24}$/ $C_{60}(OH)_{20}$. This suggests that C_{70}-NOM impacts on mammalian cells similarly to C_{60}, possibly due to the hydrophobicity and dissociation of C_{70}-NOM to facilitate C_{70} interacting with the fatty acyl chains in the lipid bilayer. Such hydrophobic interaction, when coupled with the ROS production by C_{70}, could result in cytotoxicity and cell lysis, especially at high NP concentrations.[130] Unlike C_{70}-NOM, $C_{60}(OH)_{20}$ is more hydrophilic and, therefore, is largely excluded by mammalian cells due to the same reasons discussed above for plant cell membranes.

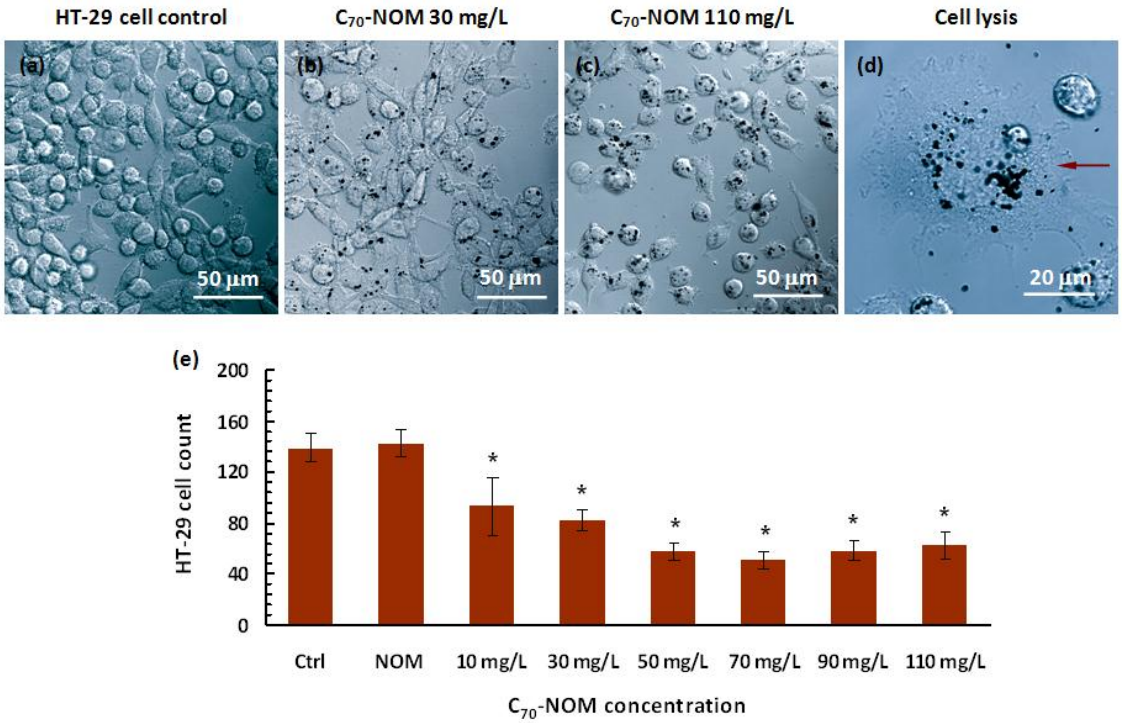

Figure 2-11 Mammalian cell damage in the presence of C_{70}-NOM of various concentrations. Incubation time: 9 h. (a) HT-29 cell control. (b) HT-29 cells in the presence of C_{70}-NOM of 30 mg/L. (c) HT-29 cells in the presence of C_{70}-NOM of 110 mg/L. (d) Cell lysis (indicated by red arrow) in the presence of C_{70}-NOM at 110 mg/L. The aggregation of C_{70} particles is evident in (b-d). (e) HT-29 cell count in the presence of C_{70}-NOM of various concentrations. The asterisks indicate data which are statistically different from the control ($p<0.01$). NOM: positive control.

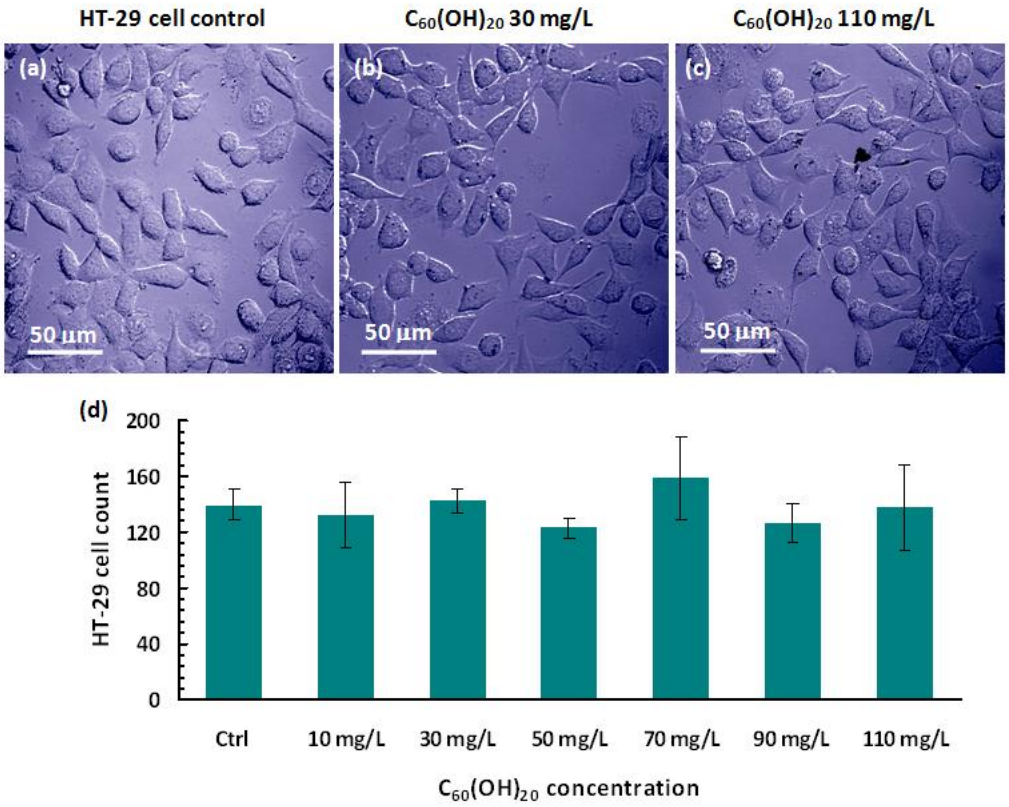

Figure 2-12 Mammalian cell damage in the presence of $C_{60}(OH)_{20}$ of various concentrations. Incubation time: 9 h. (a) HT-29 cell control. (b) HT-29 cells in the presence of $C_{60}(OH)_{20}$ of 30 mg/L. (c) HT-29 cells in the presence of $C_{60}(OH)_{20}$ of 110 mg/L. (d) HT-29 cell count in the presence of $C_{60}(OH)_{20}$ of various concentrations.

2.4 Conclusion

The differential plant and mammalian cell responses to NPs (Figure 2-7 top panel vs. Figure 2-11e; Figure 2-7 lower panel vs. Figure 2-12d) can be understood as a combined result of NP filtration by the porous plant cell wall, confinement on NP mobility by the hydrophobic, thick (a few to tens of micrometers), and rigid plant cell wall and the amphiphilic, thin (~7 nm), and fluidic plasma membrane,[146] as well as

the physiochemical properties of the NPs. The filtration by the plant cell wall favors uptake of smaller and more hydrophilic NPs. Post-translocation these small and hydrophilic NPs are confined at the interface between the plant cell wall and the plasma membrane, and self-assemble to initiate a mechanical damage to the plasma membrane. Larger and more hydrophobic NPs of low concentrations exert little damage on the plant cell. However, at high concentrations adsorption of hydrophobic NPs onto the plant cell wall and their retention within the plant cell wall would still impact on the physiological state of the plant cell, as implied by the emergence of cell damage with C_{70}-NOM of 90 mg/L and 110 mg/L (Figure 2-7 top panel). Absence of a cell wall in mammalian cells is favorable for minimizing the adverse effect of hydrophilic NPs, but encourages membrane partitioning[147] by hydrophobic and/or noncovalentlyfunctionalized NPs to induce cell damage. Such differentiality on NP uptake may help shed light on the intensive debate on nanotoxicity, and shall prove beneficial for guiding the design of nanomedicine and environmentally sustainable nanotechnologies.

CHAPTER 3. CALCIUM-ENHANCED EXOCYTOSIS OF GOLD NANOPARTICLES

Chapter 3 examines the exocytosis of NPs, an important but rarely documented aspect of cell responses to engineered nanomaterials. Specifically, HT-29 mammalian cells were labeled with a lipophilic Laurdan dye, and the membrane fluidity in the presence of gold NPs was evaluated by the generalized polarization (GP) values derived from the fluorescence spectra of the dye. Exocytosis of the gold NPs, in the presence of extracellular calcium ions, was inferred from the GP values, which decreased over time and correlated with the increased extracellular calcium concentration. This study provides new information for understanding the fate of nanomaterials in cellular systems.

3.1 Introduction

Engineered nanomaterials are produced in increasingly significant quantities, driven by growing research, industry, and domestic needs. Post-application these engineered nanomaterials will likely be discharged to landfills, and subsequently released into the air, water, and soil in the natural environment.[124–127] Depending upon their physicochemistry and localization, such discharged nanomaterials may gain mobility through their noncovalent supramolecular assembly or covalent functionalization with natural organic matter and various pollutants, biomolecules, and organisms, and consequently become integrated into the ecosphere, including the food chain.[23], [148] In addition to the environmental concerns, the biological impact of the nanomaterials that

are exploited for drug delivery, cosmetics, and foodstuffs is yet to be fully understood.[149], [150] In view of the rapid development of nanotechnology and its vast biological and environmental applications and implications, it is imperative to obtain a database on describing the behaviors of nanomaterials in living systems, especially on the cellular level.

The discharge of foreign materials in a cell is usually conducted through exocytosis. During the process of exocytosis, vesicles which contain the materials to be exocytosed first dock onto the inner surface of the cell membrane, then merge with the membrane, and finally release the material content to the extracellular space. The mechanism of exocytosis has recently been elucidated for neuronal and secretory cells, where the exocytosed materials such as neurotransmitters and hormones were natural components of the host cells.[151–154] In contrast, there is little knowledge as to how exocytosis is executed for endocytosed or administered engineered NPs.[155]

The most important venue in which exocytosis occurs is the cell membrane. Driven by thermodynamics and metabolism, amphiphilic lipid molecules undergo rapid lateral and rotational diffusion within the two dimensional continuum of the lipid bilayer. A cell membrane usually assumes a solid gel phase state at lower temperatures, but adopts a fluid phase state at higher temperatures.[154], [156], [157] The packing of lipids within a bilayer also affects the mechanical properties of the cell, including the cell resistance to external stimuli such as stretching and bending.[157] During endocytosis, a receptor initiated or facilitated process of engulfing foreign materials by the cell, the consumption of lipids in forming vesicles for containing the foreign materials increases

the area per lipid molecule, thereby causing the cell membrane to shift toward the fluid phase.[144] The process of exocytosis, in contrast, recycles vesicles from the intracellular space back to the cell membrane, decreasing the area per lipid molecule and causing a shift of the cell membrane toward the gel phase.[158]

3.2 Results and Discussion

In view of the essential role of excytosis in governing cell responses to nanomaterials this section examines the relationship between the rate of exocytosis of AuNPs and the concentration of the physiologically essential calcium ions[159], [160] in the extracellular space. The use of the more biocompatible AuNPs[6], [132], [161] was to minimize the potential complications to the current study introduced by nanotoxicity. To indicate the phase transition of the cell membrane, a Laurdan dye *(*6-Dodecanoyl-2-dimethylaminonaphthalene, AnaSpec) was used to partition into the membrane and report on the local environment of the dye through fluorescence emission. The lipophilic Laurdan dye possesses a dipole moment induced by a partial charge separation between the 2-dimethylamino and the 6-carbonyl residues. When surrounded by polar solvent molecules such as water, the dipole moment of the dye assumes a lower excited energy level by reorienting the solvent molecules, giving off a red-shifted emission spectrum upon light excitation. Upon the occurrence of endocytosis, the dye molecule partitioned into a lipid bilayer experiences a more polar environment with the incorporation of water

(Figure 3-1(a)). Conversely, a partitioned dye molecule experiences a less polar environment as a result of exocytosis.[144], [156–158], [162]

The physical properties closely related to the membrane phase can be quantitatively described by GP of the membrane, defined as:[156]

$$GP = \frac{I_B - I_R}{I_B + I_R},$$

where I_R denotes the fluorescence intensity in the red region, and I_B the fluorescence intensity in the blue region. When the membrane shifts from the gel to the fluid phase, the fluorescence intensity of the Laurdan dye in the blue region decreases while that in the red region increases (Figure 3-1(b)) to induce a decreased GP value.

HT-29 human colonic adenocarcinoma cell lines were used as a model system in our study. The cells were cultured in McCoy's 5A medium (ATCC) in a flask for 1 to 2 days depending upon their condition of growth. The healthy cells were then transferred to a 96-well plate and kept in an incubator (at 37 ℃, in 5% CO_2 flow) for one day to initiate their attachment to the bottom of the plate wells. To detect phase transition, the cells were pre-labeled with the Laurdan dye for 1 h in the incubator. After incubation, the dye solution was removed and the cells were rinsed with PBS buffer. The wells were then refilled with fresh culture medium, and confocal fluorescence imaging (*Nikon Ti* Eclipse) was performed to confirm cell viability and partitioning of the dye in the cell membranes (cell cross-sections shown as blue rings under light excitation at 340 nm, Figure 3-1(c)).

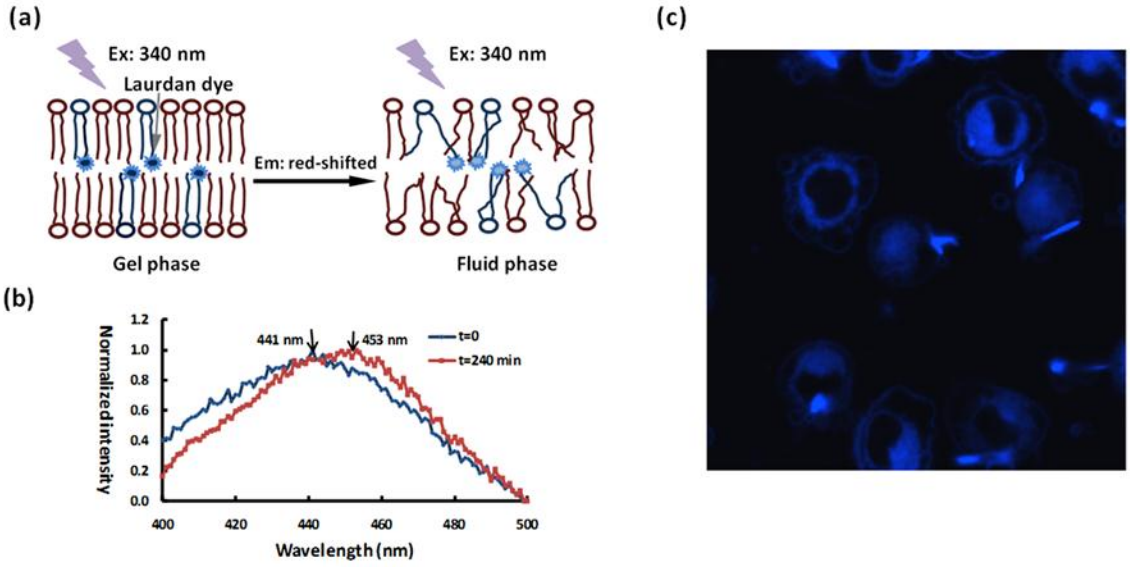

Figure 3-1 (a) Experimental scheme showing labeling of a lipid bilayer using the lipophilic Laurdan dye. When excited with light at 340 nm, a red shift of the dye emission (illustrated by a change of dye emission color from dark to light blue) is induced when the bilayer undergoes a transition from the gel to the fluid phase. (b) Example of the red shift of the Laurdan dye emission, from a peak wavelength of 441 nm to 452 nm for a time lapse of 240 min. Excitation: 340 nm. (c) Confocal fluorescence image of HT-29 cells labelled with Laurdan, showing the cross-sections of the cell membranes as blue rings. Excitation: 340 nm.

To examine the effect of Ca^{2+} concentration on cell exocytosis of engineered NPs, positively charged AuNPs (Vive Nano), coated with poly(quaternary ammonium) for solubility and steric separation, were added to the culture medium at different dosages (from 0.0005 to 0.5 mg/mL). The hydrodynamic size of the AuNPs was determined to be

10 nm in diameter (S90, Malvern). The zeta potential of the AuNPs was characterized to be +65 mV (ZetaSizer Nano, Malvern), indicating an excellent stability of the NP suspension.

The cultured HT-29 cells were then incubated with the AuNPs for 2 h to allow the cells to undergo endocytosis of the NPs. These positively charged AuNPs were expected to be readily integrated by the cells due to the negative electric potential of approximately -80 mV to -40 mV across the plasma cell membrane. The plate wells to which the cells were attached were rinsed and then refilled with culture medium after the original medium with free and adsorbed AuNPs was removed, thus promoting exocytosis of the NPs to be initiated and immediately measured.

For mammalian cells, the physiological extracellular Ca^{2+} concentration is approximately 2 mM.[163] In our study, Ca^{2+} concentration in the culture medium was adjusted to 0-10 mM by adding Na_2CO_3 or $CaCl_2$ solutions to ensure the biological relevance of the experimental design. A spectrofluorometer (Cary Eclipse, Varian) was used to excite the Laurdan dye at 340 nm and the fluorescence emission intensities of the dye were collected at 416 nm and 473 nm. The fluorescence intensities at these two specific wavelengths were then used to calculate the GP values. The spectrofluorometer chamber was operated at room temperature without the flow of CO_2. For each sample condition (AuNPs and Ca^{2+} concentrations), 4 replicates were measured to obtain the error bars for statistical analysis. Significant differences from the control samples (AuNPs of 0 mg/mL in Fig. 2(a), or Ca^{2+} concentration of 0 mM in Figure 3-3) were

examined using a student *t*-test. Statistical significance was acceptable when the probability of the result of the *t*-test assuming null hypothesis (*p*) is less than 0.01.

Figure 3-2(a) shows the GP values measured immediately after incubation of the HT-29 cells with the AuNPs, when exocytosis of the NPs was expected to be initiated. The GP value decreased from 0.0488 to -0.145 when the concentration of the AuNPs was increased from 0 to 0.5 mg/mL. Compared with the control (not treated with AuNPs), the decrease in the GP value versus the increase in the AuNP concentration was statistically significant (p-values < 0.01 for all samples treated with the AuNPs). This result suggests that higher AuNP concentrations resulted in a more fluid-phased plasma membrane; further implying that a larger amount of the AuNPs was taken up by the cells with their increased concentrations.[37], [155] This result further verifies the hypothesis that AuNP suspensions of up to 0.5 mg/mL did not cause significant aggregation.

The GP values are shown to decrease overtime in Figure 3-2(b) for the control sample (not treated with the AuNPs, only labeled with the Laurdan dye), suggesting that the plasma cell membranes themselves can undergo a transition from the gel phase to the more fluidic phase, possibly due to the gradual loss of cell viability under non-ideal conditions in the spectrofluorometer chamber (22 ℃ instead of 37 ℃, and lack of CO_2 flow). Compared with the control, the samples treated with AuNPs of 0.0005 mg/mL and Ca^{2+} of 10 mM in the culture medium showed a far less pronounced decrease in the GP value over the same time period of 240 min (a drop of 229% for the control samples versus a drop of 97% for the AuNP-treated samples). These different changing rates of the GP values can be attributed to the onset of exocytosis of the endocytosed AuNPs,

which led to a recovery of the lipid content to sustain the gel-phased cell membranes. The low AuNP concentration (0.0005 mg/mL) was chosen to both ensure integrity of the cell membranes post endocytosis, and reveal the process of exocytosis of the AuNPs.

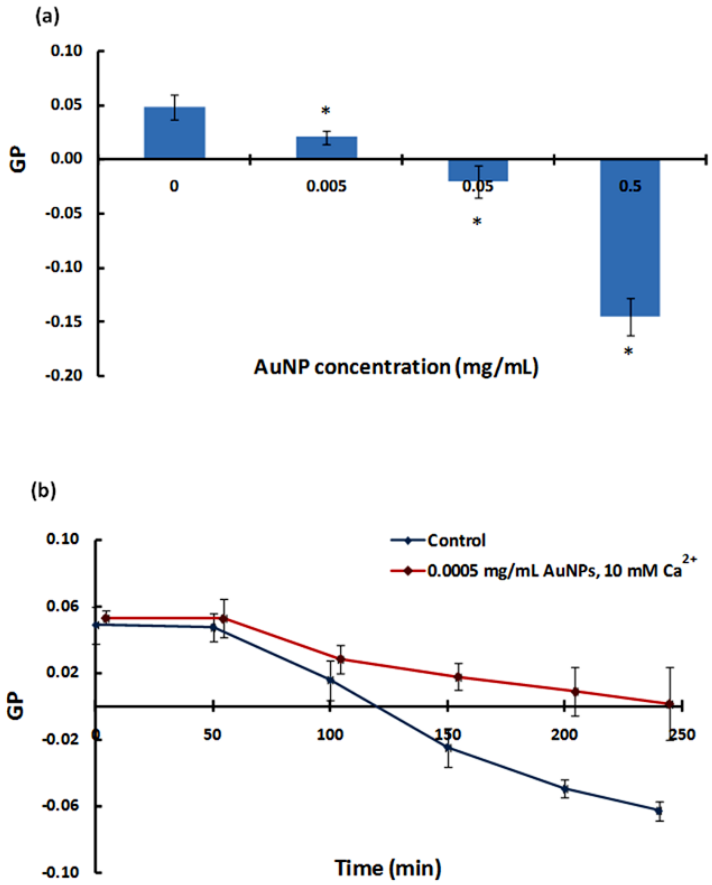

Figure 3-2 (a) GP values for cells incubated with different concentrations of AuNPs, measured immediately after the free NPs were removed. The asterisks indicate statistically different GP values from that for the control samples (0 mg/mL AuNP concentration) ($p < 0.01$). (b) Change in GP value over time for control cells (blue curve) and cells pre-incubated with AuNPs of 0.0005 mg/mL and treated with Ca^{2+} of 10 mM (red curve).

To confirm that the slower GP changing rate in Figure 3-2(b) was induced by exocytosis, extracellular liquids were collected for the cells exposed to Ca^{2+} of 0 to 10 mM for 4 hours, after being pre-incubated with AuNPs of 0.5 mg/mL and 0.05 mg/mL for 2 hours respectively and wash thoroughly. Absorbance of the extracellular liquids was measured at the peak wavelength of 490 nm for the AuNPs using an absorbance plate reader (Biotek). As shown in Figure 3-3(a), the absorbance of the extracellular liquids increases steadily with the increased Ca^{2+} concentration indicating both the occurrence of cell exclusion of the AuNPs and the dependence of such exclusion on the Ca^{2+} concentration.

The chestnut bars in Figure 3-3(b) represent the GP values for the cell samples 4 h after incubating with Ca^{2+} of 0 to 10 mM (untreated). The GP values for all Ca^{2+} concentrations display no statistically significant differences, indicating that, of the working concentration range, Ca^{2+} alone did not alter the membrane phase. To further illustrate the effect of Ca^{2+} concentration on exocytosis rate, the above procedure was repeated for cells treated with AuNPs of 0.005 mg/mL. The blue bars inFigure 3-3(b) represent the GP values for the cell samples with added Ca^{2+} of 0 to 10 mM, 4 h after exocytosis began to dominate. The GP values are shown to positively correlate with the Ca^{2+} concentrations in the culture medium in the presence of pre-endocytosed AuNPs (the GP value increased from -0.126 ± 0.020 to 0.019 ± 0.010 when the Ca^{2+} concentration was raised from 0 to 10 mM). This correlation is understandable since the process of exocytosis served to recover phospholipids in the cell membranes and therefore induced the transition of the membranes towards the gel phase. This result offered evidence that

exocytosis of AuNPs could be enhanced by increasing the Ca^{2+}concentration in the extracellular space, in accordance with other reports on the exocytosis of mammalian cells without the introduction of NPs.[151–154]

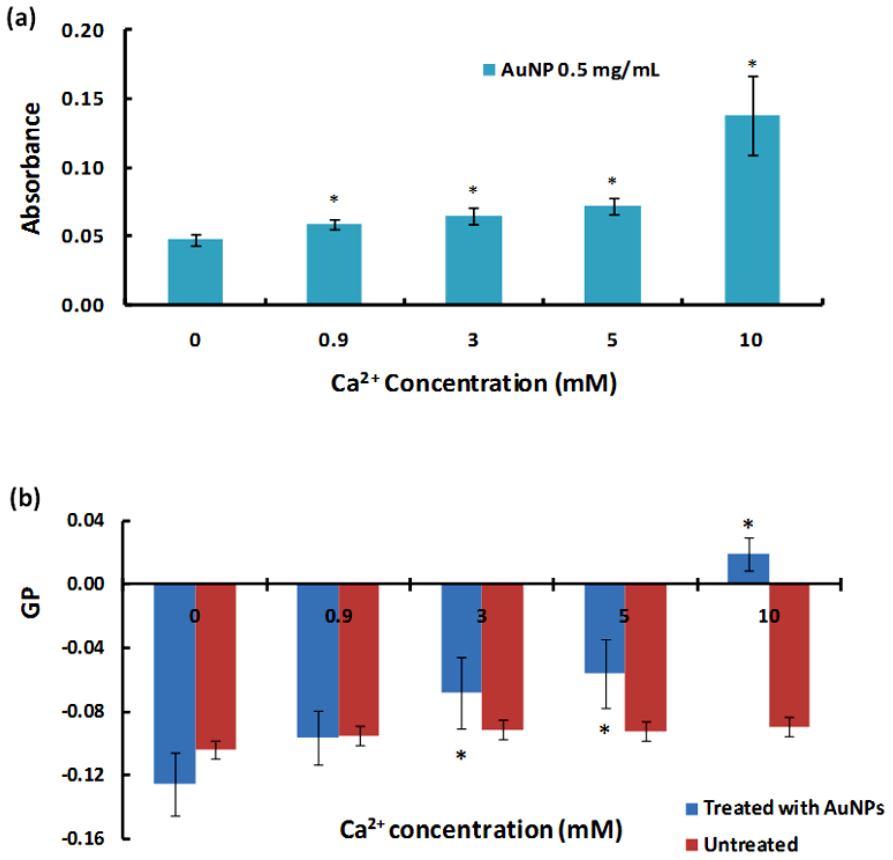

Figure 3-3 (a) Absorbance of the AuNPs collected from the extracellular space vs. Ca^{2+} concentration. The original AuNP concentrations: 0.5 mg/mL (cyan bars) and 0.05 mg/mL (pink bars). Incubation time of the AuNPs with the cells: 2 h. Exposure time of cells to Ca^{2+}: 4 h. (b) GP values of cells treated (blue bars) & untreated with AuNPs (chestnut bars) in culture medium with different Ca^{2+} concentrations. Incubation time of the AuNPs with the cells: 4 h. AuNP concentration: 0.005 mg/mL. The asterisks indicate

statistically different absorbance/GP values from that for the control samples (0 mM Ca^{2+} concentration) ($p < 0.01$).

3.3 Conclusion

This study offers an initial examination on the exocytosis of engineered NPs by human colonic adenocarcinoma cells. Increased AuNP concentrations have been shown to enhance endocytosis, possibly to compensate for the increased uptake of the NPs and to maintain HT-29 cell viability. The rate of exocytosis of AuNPs by the cells correlates with the increased Ca^{2+} concentration in the extracellular space. Since the influx of Ca^{2+} is governed by the ion channels in the cell membrane, the observed differences in the rate of membrane phase transition were mainly a result of lipid recovery through exocytosis of the AuNPs and, to a lesser extent, a result of the transition to the fluid phase due to non-ideal environmental conditions in the spectrofluorometer chamber. Although only AuNPs were used in this current study, these reported observations may have broader applicability to the cases of exocytosis of other engineered NP species. To fully understand such biological processes, other factors that normally affect exocytosis of natural components in the host cells, such as ionic strength, membrane potential, and gating of ion channels, may be examined in connection with the physiochemical properties of the NPs (surface charge, shape, and functionalization) and the biophysical interactions (electrostatic, vdW, H-bonding, and hydrophobic forces) between the NPs and the lipids and proteins in the cell membranes.

CHAPTER 4. COMPARISON OF NANOTUBE-PROTEIN CORONA COMPOSITION IN CELL CULTURE MEDIA

As introduced in Chapter 1, protein corona is a mono- or multi-layer of protein surface coating on nanomaterials in biological environments. The addition of the protein corona may alter both the pharmacokinetics and pharmacodynamics of the nanomaterial thereby influencing toxicity. Utilizing a label-free mass spectrometry-based proteomics approach, we have examined the composition of proteins forming the protein corona for a set of nanomaterials including unmodified and carboxylated SWCNT and MWCNT, polyvinylpyrrolidone (PVP)-coated MWCNT (MWCNT-PVP), and nanoclay. To simulate cell culture conditions, nanomaterials were incubated for 1 h in DMEM supplemented with 10% fetal bovine serum, washed, resuspended in PBS, and assessed by liquid chromatography (LC)-mass spectrometry (MS)/MS for their associated protein content. To determine those attributes of nanomaterials that influence corona formation, the NPs were extensively characterized. All nanotubes (NTs) were found to have negative zeta potentials in water (SWCNT-COOH < MWCNT-COOH < Unmodified NTs) while carboxylation increased the hydrodynamic size of NTs. All NTs were also found to associate with a common subset of proteins that included albumin, titin, and apolipoproteins. Specifically, SWCNT-COOH and MWCNT-COOH were found to associate with the greatest number of proteins (181 and 133 respectively) compared to the unmodified NTs (<100), possibly due to the abundance of protein amines via the formation of covalent bonding. Modified NTs, however, bound a number of unique

proteins that were not found to associate with unmodified NTs, implying hydrogen bonding and electrostatic interactions were involved in the corona formation. PVP-coating of MWCNT did not significantly influence the protein types found in the coronas, further reinforcing the possibility of hydrogen bonding and electrostatic interactions. In conclusion, we observed differential protein corona composition based on functionalization and purity of NTs, which may influence the unique biological effects of these nanomaterials.

4.1 Introduction

The field of nanotechnology is rapidly expanding and evolving with the development of numerous engineered nanomaterials. These synthesized nanomaterials can be utilized in various fields including multiple applications in biomedical and consumer products. Nanomaterials often possess a high degree of functionality to render a variety of physicochemical characteristics including diverse chemical composition, available surface groups, shape, electrothermal conductance capabilities, and solubility. Based upon these properties, nanomaterials may be distributed to any organ system and interact on a subcellular level making them useful for both the diagnosis and treatment of diseases.

Upon introduction into a physiological environment nanomaterials are rapidly coated with a layer of proteins, known as the protein corona [115], [164], [165]. The protein corona alters the size and interfacial composition of the nanomaterials, imparting

a biological identity distinct from their original synthetic identity that may modify their activity, bio-distribution, clearance, and toxicity. The distinct composition of the protein corona, and therefore the nanomaterial's biological activity, is influenced by the biological environment and the characteristics of each nanomaterial. Ultimately, the protein corona for each nanomaterial appears to be unique and is determined by each nanomaterial's individual composition, surface charge, shape and other distinguishing characteristics [5], [166]. The corona and its "epitope map" [115] can be viewed as the bioactive entity to which the cells respond. It has been hypothesized that modulation of the proteins which form the protein corona could be useful in targeting nanomaterials to desired tissues, cells and/or subcellular targets [167].

Research has demonstrated that the capacity of nanomaterials to bind a variety of plasma proteins including those implicated in coagulation, lipid transport, ion transport, complement activation, and pathogen recognition [166], [168]. Furthermore *in vitro* studies have demonstrated that the protein corona may influence nanomaterial uptake by cells and alter cytotoxicity [169–173]. Adsorption of a variety of proteins including IgG and fibrinogen has been shown to increase macrophage phagocytosis of nanomaterials *in vitro* [174], [175]. The ability of the protein corona to enhance macrophage phagocytosis and clearance may have significant implications such as modifying subsequent immune responses and increasing systemic inflammation and oxidative stress. Polysorbate-coated NPs have been shown to preferentially associate with apolipoprotein E, thereby increasing distribution across the blood brain barrier possibly through mimicking low-density lipoprotein and enhancing endothelial cell uptake [12], [176]. Conversely,

macrophage internalization of both positively and negatively-charged silicon microparticles is enhanced in serum-free media compared to media with serum, suggesting that addition of the protein corona in some cases may inhibit interactions with cell surface receptors mediating uptake [177]. Manipulation of cellular uptake via modulation of the protein corona could therefore be therapeutically beneficial for cell targeting of nanomaterials; however, it may also have unexpected toxicological consequences through effects on biodistribution, accumulation, and clearance. Evidently, the formation and biological effects of nanomaterials and their protein coronas are extremely complex and require further evaluation and study.

Because of cost, ethical, and efficiency considerations, *in vitro* toxicity assays are widely used for screening and assessing the toxicity of NPs. *In vitro* screening of NP safety has been ineffectual due to assay interference and contrasting findings likely resulting from differences in particle suspension, cell culture media and delivery, thereby limiting their predictive value. However, their predictive capabilities can be improved by characterizing NP interactions with fetal bovine serum proteins often used in cell culture media, and how protein coronas affect NP-cell interaction and biological effects [173]. Previous *in vitro* exposure studies of both functionalized and non-functionalized carbon NTs in barrier epithelial cells [178], [179] demonstrated significant NT-specific effects on relevant molecular and cellular functions and canonical pathways, with little overlap across NT type, dose, or functionalization, even in the absence of overt toxicity. These studies suggest other physicochemical characteristics, such as the protein corona, may be accountable for the inconsistencies. Accordingly, in the present study, we investigated

characteristics of NTs, along with that of halloysite nanoclay, which contributed to the formation of the protein corona in fetal bovine serum often used during the *in vitro* evaluation of nanomaterial toxicity. We employed a comprehensive proteomics analysis to determine the identities and individual abundance of proteins that associate with NTs after incubation in bovine serum-supplemented culture media. This information is necessary in understanding properties of nanomaterials that govern their interactions with proteins in biological environments and ultimately lead to the unique biological responses.

4.2 Materials and Methods

Reagents and materials:

DL-Dithiothreitol (DTT), urea, triethylphosphine, iodoethanol, and ammonium bicarbonate were purchased from Sigma-Aldrich (St. Louis, MO, USA). LC-MS grade 0.1% formic acid in acetonitrile and 0.1% formic acid in water were purchased from Burdick & Jackson (Muskegon, MI, USA). Modified sequencing grade porcine trypsin was obtained from Princeton Separations (Freehold, NJ, USA). DMEM with glutamax and 10% heat inactivated fetal bovine serum were purchased from Invitrogen (Carlsbad CA).

SWCNT were purchased from Unidym (Sunnyvale, CA) and MWCNT were purchased from Cheap Tubes Inc. (Brattleboro, VT). SWCNT-COOH and MWCNT-COOH were generated in a Microwave Accelerated Reaction System (Mode: CEM Mars)

fitted with internal temperature and pressure controls as previously described [180], [181]. Pre-weighed amounts of purified MWCNT were treated with a mixture of concentrated H_2SO_4 and HNO_3 solution by subjecting them to microwave radiation at 140 ℃ for 20 min. The product was filtered through a 10 μm membrane filter, washed with water to a neutral pH, and dried under vacuum at 80 ℃ to a constant weight. SWCNT-COOH was also functionalized in the Microwave Accelerated Reaction System [182]. Pre-weighed amounts of purified SWCNT were treated with a 1:1 mixture of concentrated H_2SO_4 and HNO_3 solution by subjecting them to microwave radiation at 120 ℃ for 3 min. The mixture was then diluted with distilled water and filtered through 10 μm membrane filter paper. The filtrate was transferred to a dialysis bag and placed in a container filled with DI water, which was continually replaced until it achieved neutral pH. The filtrate was then dried overnight at 50 ℃ under vacuum. This led to the formation of carboxylic acid groups on the surface of the NTs resulting in high aqueous dispersibility. MWCNT-PVPs were prepared according to a procedure previously reported by Ntim et al. [183]. Purified MWCNTs were dispersed in deionized water at a concentration of 50 mg/L with the aid of 1% SDS. One percent by weight of PVP was added to the mixture, which was then incubated at 50 ℃ for 12 hr. The carbon NTs were then filtered through a 10 μm membrane filter, washed with deionized water followed by three cycles of ultrasonic redispersion in deionized water to remove any residual SDS. The sample was filtered and dried under vacuum at room temperature to a constant weight.

TEM and energy dispersive spectroscopy (EDS):

All individual halloysite (nanoclay), SWCNT, and MWCNT samples were mixed with ethanol and sonicated in a water bath (Branson) for 10-15 min until well dispersed. For each sample a droplet of the suspension was placed on a copper grid and dried at room temperature. TEM imaging and EDS element analysis were performed using a Hitachi HD 2000 STEM equipped with an Oxford INCA Energy 200 EDS.

Hydrodynamic size and zeta potential characterization:

Approximately 0.1 mg of each sample was mixed with 1 mL 10% fetal bovine serum (FBS)-supplemented DMEM, and then dispersed via water bath sonication for 2 min. Samples were then incubated on a rotator for 1 h. The hydrodynamic sizes of the suspended samples were measured using a dynamic light scattering device (Malvern Instruments, Nanosizer S90). The zeta potentials of the suspended samples in water were measured using electrophroretic light scattering (Malvern Instruments, ZetaSizer Nano).

Protein corona generation and proteomic characterization:

Based on a modification of Tenzer's method [184], 1 mg of each NT type was suspended in 10 mL of DMEM culture media supplemented with 10% FBS, briefly sonicated in a bath sonicator, diluted 1:10 in FBS/media, and incubated for 1 h at 37℃ (to simulate *in vitro* exposure protocols). Stable protein coronas are at equilibrium within 5 min [185]. The samples were centrifuged (15 min at 3,000 x g/22℃) and the pellets containing the NT-protein complexes were washed and pelleted three times with PBS. After the third and final wash, the supernatant was free of protein. Protein coronas were solubilized *in situ* using a lysis buffer specific for label-free quantitative mass spectrometry (LFQMS) (8 M urea, 10 mM DTT freshly prepared). For comparative

reference purposes, 100 μg of FBS supplemented culture media proteins were also solubilized for LC-MS/MS analysis. Briefly, protein samples were reduced and alkylated by triethylphosphine and iodoethanol [186] and proteolyzed using porcine trypsin. Exactly 20 μg of each tryptic digest sample was injected randomly as two technical replicates onto a C_{18} reversed phase column for a 3 h high performance liquid chromatography (HPLC) gradient separation, electrospray ionization, and analysis using an LTQ-PROTEOMEX ion trap mass spectrometer. A blank was injected between each sample to clean and balance the column and eliminate carryover. The acquired data were searched against the most up-to-date UniProtKB Bos taurus (Bovine) database using SEQUEST (v. 28 rev. 12) algorithms in Bioworks (v. 3.3). Peptide and protein identifications were validated by PeptideProphet [187] and ProteinProphet [188] in the Trans-Proteomic Pipeline (TPP, v. 3.3.0). Only proteins and peptides with (a) protein probability ≥ 0.9, (b) peptide probability ≥ 0.8, and (c) peptide weight ≥ 0.5 were used in the quantification algorithm. Identified bovine proteins whose names appeared as "uncharacterized" were annotated using homologous human proteins identified by UniProt Blast based on similarity in amino acid sequence.

Protein abundance was determined using IdentiQuantXL™ [189]. After chromatogram alignment and peptide retention time determination, a weighted mean m/z of each peptide is calculated and a tab delimited file was created to extract peptide intensity using MASIC [190]. Peptides were then filtered according to intensity CV across all samples and intensity correlation for those identifying a particular protein. Protein abundance (intensity) was calculated from all qualified peptides corresponding to

a particular protein. Protein abundance/quantity calculated in this way has no units, and therefore are represented by unitless numerical values in Table 4-2 & Table 4-4. Comparison of the mean abundance of individual protein in each corona, generated by LFQMS, was performed within the IdentiQuantXL™ platform using one-way ANOVA and Pairwise Multiple Comparisons (Holm-Sidak method). False discovery rate (FDR) [191] was estimated using Q-value software.

4.3 Results and Discussion

Nanotube Characteristics:

Electron microscopy images (Figure 4-1) confirmed the dimensions of the carbon NTs (first row in Table 4-1): the SWCNT were 0.1-1 μm, the MWCNT were 10-30 μm, and the nanoclay were 0.5-2 μm in length. Results from the elemental analysis of energy dispersive spectra (Table 4-1) showed the elemental composition of the NTs and demonstrated changes in surface chemistry. The existence of nitrogen confirmed the polyvinylpyrrolidone (PVP) coating of MWCNT-PVP samples, whereas the relatively high content of oxygen indicates the existence of COOH-surface functionalization on MWCNT-COOH and SWCNT-COOH samples. The nanoclay, as expected, showed an abundance of oxygen, aluminum and silicon.

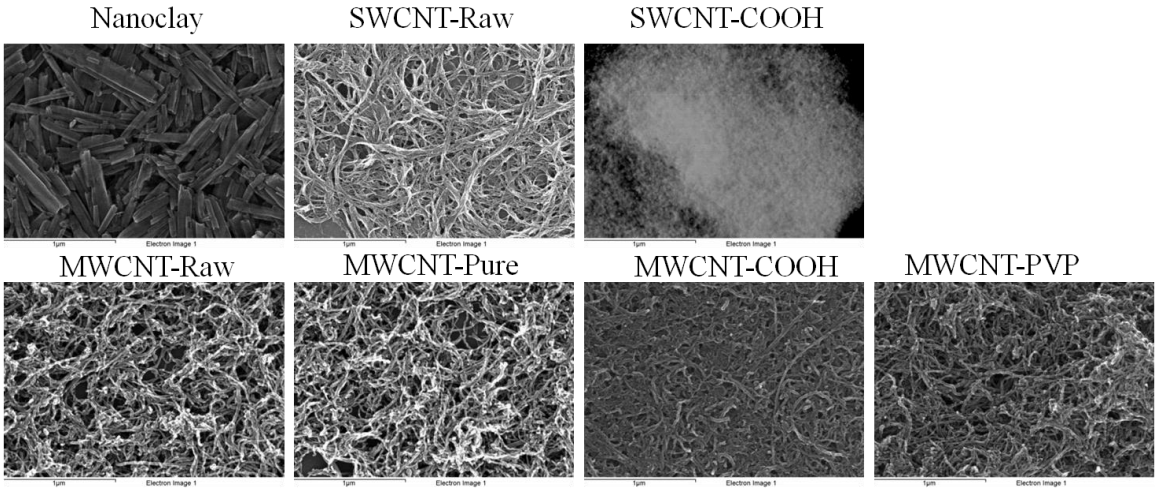

Figure 4-1 TEM images of nanoclay, unmodified SWCNT (SWCNT-Raw), carboxylated SWCNT (SWCNT-COOH), unmodified MWCNT (MWCNT-Raw), pure MWCNT (MWCNT-Pure, carboxylated MWCNT (MWCNT-COOH), and PVP-coated MWCNT (MWCNT-PVP) samples confirming the dimensions of all carbon NTs used in this study.

	Nanoclay	MWCNT-Pure	MWCNT-Raw	SWCNT-Raw	MWCNT-PVP	MWCNT-COOH	SWCNT-COOH
Length (μm)	0.5-2	10-30	10-30	0.1-1	10-30	10-30	0.1-1
Carbon (%)	3.81	98.77	98.65	94.91	97.59	97.4	96.92
Oxygen (%)	37.75	1.23	1.35	4.41	1.23	2.60	3.08
Nitrogen (%)	0.82			0.68	1.19		
Aluminum (%)	25.80						
Silicon (%)	25.42						
Calcium (%)	0.20						
Iron (%)	1.81						
Copper (%)	4.39						

Table 4-1 Length and Percent Elemental Composition of NPs. (All shaded cells denote elements that were not in sufficient quantity to be detected by energy dispersive spectroscopy.)

The hydrodynamic sizes of the samples suspended in FBS-supplemented DMEM culture medium, in comparison to those suspended in water, revealed consistently increased size for all COOH-surface functionalized NTs, by approximately 60 to 120%, likely due to the adsorption of proteins, amino acids and lipids from the medium (Figure 4-2). In contrast, the hydrodynamic size of non-functionalized SWCNT-Raw was decreased by approximately 25%, likely due to the debundling and dispersion of the SWCN-Raw NTs as a result of protein corona formation. For MWCNT-PVP, however, their sizes were comparable to those suspended in water (Figure 4-2), suggesting exchange of PVP by the proteins in the media for coating the MWCNT "core". For MWCNT-Raw and MWCNT-Pure samples, large aggregates were formed that precipitated out of the aqueous phase, suggesting the hydrophobicity of these two types of NTs was too high to be overcome by protein corona formation. All samples demonstrated negative zeta potentials in water (Figure 4-2). Zeta potential analysis of materials in DMEM was non-determinant due to the screening of the NTs by the ions and biomolecules in the medium. COOH-surface functionalization of both MWCNT and SWCNT and PVP-coating of MWCNT samples resulted in further decreased zeta potentials compared to raw NT samples, suggesting increased dispersion in water due to surface modulation.

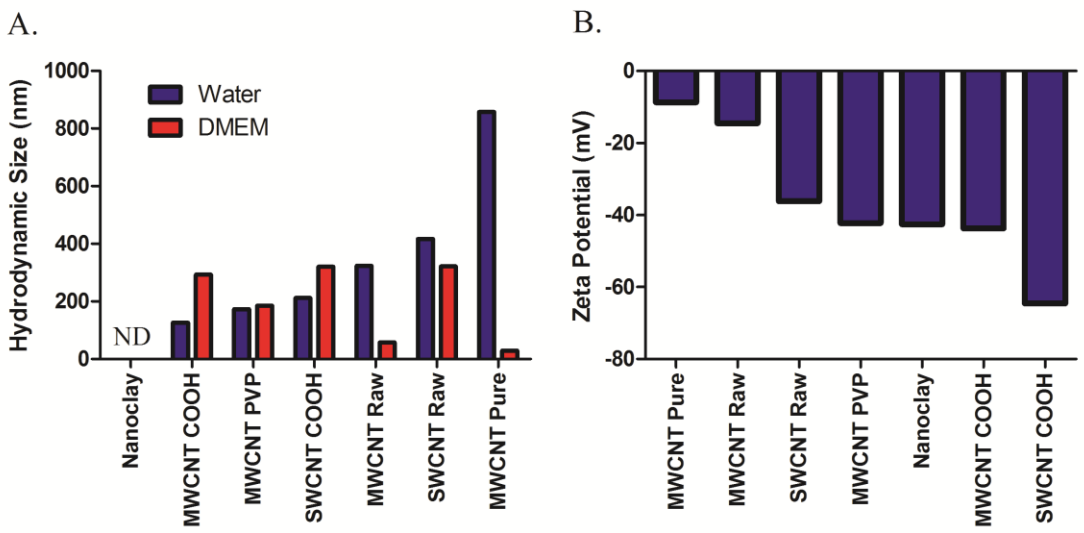

Figure 4-2 Characterization of nanoclay, SWCNT-Raw, SWCNT-COOH, MWCNT-Raw, MWCNT-Pure, MWCNT-COOH, and MWCNT-PVP samples. 2A) The hydrodynamic size for each NT was assessed in both water and DMEM cell culture media via dynamic light scattering. 2B) The zeta potentials for each NT were determined in water via electrophroretic light scattering.

Proteomic Results:

The protein corona that forms on NPs when they are exposed to protein-containing biological fluids changes their characteristics and may be responsible for NP bioactivity in cells. Since structurally similar NPs can have divergent biological effects in cell culture systems, we investigated the composition of the coronas formed on different of high aspect ratio NPs.

Proteomic analysis identified and quantified 366 different protein components of the various NT coronas. The numbers of constituent proteins detected in each NT corona are presented graphically in Figure 4-3A. The protein corona which formed on the nanoclay tubes consisted of the fewest number, 82 different proteins, whereas the SWCNT-COOH corona contained the most, at 181.

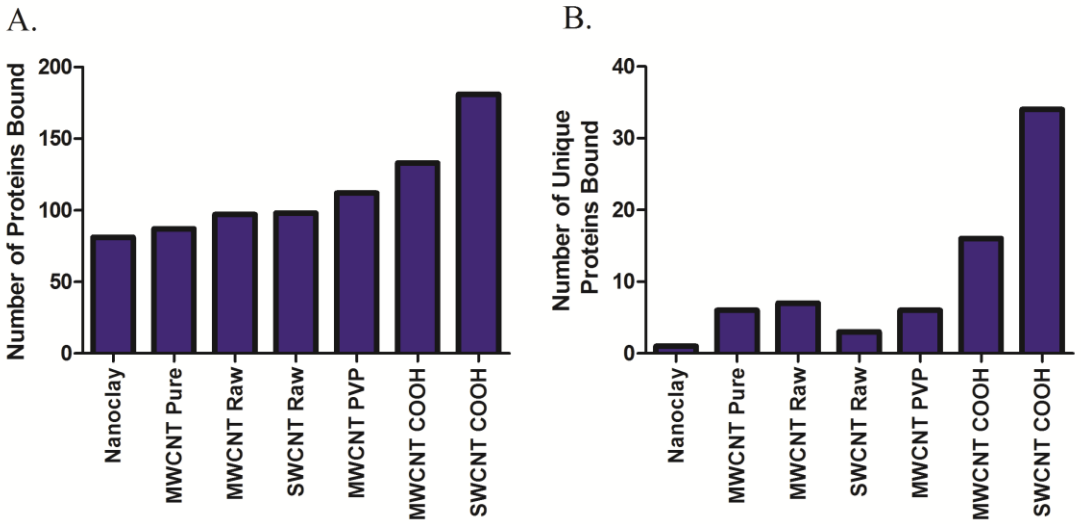

Figure 4-3 Total number and number of unique proteins found to associate with carbon-based NTs after incubation in DMEM cell culture media containing 10% fetal bovine serum. Samples were analyzed via HPLC-MS and proteins and peptides were identified using the UniProtKB Bos Taurus (Bovine) database and validated by PeptideProphet. Only proteins with a probability ≥ 0.9, or peptides with a probability ≥ 0.8, and a peptide weight ≥ 0.5 were used in the quantitation algorithm. 3A) Total number of constituent proteins detected in each NT protein corona. 3B) Total number of unique proteins detected in each NT protein corona.

All NT coronas were found to consist of 14 common proteins, including alpha-1-antiproteinase, alpha-2-HS-glycoprotein, alpha-S1-casein, apolipoprotein A-I, apolipoprotein A-II, keratin, type I cytoskeletal 10, keratin, type I cytoskeletal 15, keratin, type II cytoskeletal 1, keratin, type II cytoskeletal 5, keratin, type II cytoskeletal 6A, keratin, type II cytoskeletal 6C, keratin, type II cytoskeletal 75, serum albumin, and titin listed in Table 2 in the order of decreasing abundance. The five most abundant coronal proteins (titin, serum albumin, apolipoprotein A-I, apolipoprotein A-II, and alpha-S1-casein) exhibited significant differences across the various NTs, while the relative contributions of alpha-1-antiproteinase (aka alpha-1-antitrypsin in humans), alpha-2-HS-glycoprotein, and the 7 keratins to the NT coronas were not significantly different. With the exception of titin, alpha-S1-casein and the keratins, the highly abundant serum proteins are commonly found in NP coronas formed in human plasma/serum. Titin is the 14th most abundant protein in the FBS-DMEM media whereas albumin is 1st, alpha-2-HS-glycoprotein 2nd, and alpha-1-antiproteinase 3rd and Apo-AI is 17th, while alpha-S1-casein and the keratins (other than keratin 1) are far less abundant in the culture medium (Table 4-2). Importantly, the presence of the latter proteins in the coronas of all NPs suggests a selective enrichment which is not correlated with the protein concentrations within the media. It should also be mentioned that all of the above proteins are highly abundant in human plasma according to the most recent version of the Human Peptide Atlas database [192], with the exception of alpha-S1-casein, which is not a component of human plasma.

Protein	FBS Rank (of 2,507)	Nanoclay	MWCNT-PURE	MWCNT-RAW	SWCNT-RAW	MWCNT-PVP	MWCNT-COOH	SWCNT-COOH
Titin	14	**287,786,014¶**	249,183,558	235,313,725	**221,553,081**	**222,285,701**	**204,425,865**	**220,812,507**
Serum albumin	1	**207,804,997**	**194,609,173**	**228,671,883**	145,851,821	175,003,916	**146,190,486#**	**109,549,996***
Apolipoprotein A-I	17	**86,158,367***	25,189,155	30,866,967	16,884,667	15,747,789	20,862,300	15,827,248
Apolipoprotein A-II	85	**47,126,637***	18,727,535	21,872,077	9,851,962	13,874,155	17,637,071	9,948,567
Alpha-S1-casein	196	**43,612,167***	18,685,400	17,374,933	13,329,767	11,865,415	16,515,567	12,969,733
Alpha-1-antiproteinase	3	26,184,164	26,737,342	29,813,128	28,939,077	24,287,705	25,549,842	28,412,457
Alpha-2-HS-glycoprotein	2	26,276,777	31,171,165	30,278,503	11,817,688	24,758,827	27,448,186	14,549,701
Keratin, type I cytoskeletal 10	119	16,497,504	18,964,187	17,308,479	19,955,977	16,343,288	19,080,789	21,111,033
Keratin, type II cytoskeletal 1	27	12,015,333	8,305,850	6,632,780	7,534,533	5,764,675	6,095,444	7,003,015
Keratin, type II cytoskeletal 75	638	2,059,786	1,568,094	1,923,638	1,674,743	1,814,366	2,075,758	1,837,728
Keratin, type II cytoskeletal 6A	129	1,961,464	1,711,923	1,862,706	2,198,074	1,603,329	1,753,544	2,445,845
Keratin, type II cytoskeletal 5	1031	1,648,939	1,597,897	1,523,397	1,567,228	1,203,009	1,318,831	1,565,164
Keratin, type II cytoskeletal 6C	263	1,506,162	1,404,497	1,364,453	1,514,077	1,201,025	1,299,497	1,636,483
Keratin, type I cytoskeletal 15	347	866,543	1,039,746	779,822	1,199,950	796,696	953,023	1,000,895

Table 4-2 Abundance of the 14 proteins found in all NT protein coronas with their FBS-DMEM abundance ranking. *P<0.05 vs. all others; #P<0.05 vs. Nanoclay, MWCNT-PURE, MWCNT-RAW; ¶P<0.05 vs. SWCNT-RAW, MWCNT-PVP, MWCNT-COOH, SWCNT-COOH.

Nanoclay	MWCNT-PURE	MWCNT-RAW	SWCNT-RAW	MWCNT-PVP	MWCNT-COOH	SWCNT-COOH
TTN	XIRP2	**TTN**	**TTN**	XIRP2	**TTN**	XIRP2
ALB	**TTN**	**ALB**	**ALB**	**TTN**	**ALB**	**TTN**
APOA1	**ALB**	Bt.105991	TOP2B	**ALB**	NCOA6	NCOA6
COL6A6	KIF7	**APOA1**	AARS2	ABCA1	Bt.105991	**ALB**
APOA2	CCDC168	AHSG	**SERPINA1**	ALS2	ABCA1	P2RX5
KCTD3	AHSG	**SERPINA1**	KRT10	AHSG	LCT	ATAD2B
CSN1S1	P2RX5	ATAD2B	ATAT1	**SERPINA1**	AHSG	ALS2
ATAD2B	**SERPINA1**	ALS2	**APOA1**	COL3A1	**SERPINA1**	LCT
AHSG	**APOA1**	**APOA2**	CPS1	HBA	AARS2	KIF7
SERPINA1	HBA	COL6A6	CSN1S1	**KRT10**	ATAD2B	ABCA1
MTMR3	BIRC6	HBA	AHSG	**APOA1**	**APOA1**	CCDC168
HBA	KRT10	MTMR3	COL4A6	**APOA2**	**KRT10**	**SERPINA1**
DNAH1	**APOA2**	CSN1S1	**APOA2**	SLAMF9	**APOA2**	MTMR3
TTC13	CSN1S1	**KRT10**	TCTN1	Bt.65579	CSN1S1	**KRT10**
FAM179B	EP400	BSN	JAG1	ADAMTS16	HBA	PTPRS
BRPF1	PLCE1	CYP27B1	RPTN	CSN1S1	MTMR3	EP400
KRT10	TCTN1	AIM1L	MAGI1	AFAP1	BRPF1	ABCC1
HBG	WWP1	CPS1	Bt.63231	AGL	DNAH11	PTPRN
HERC5	NT5DC3	PTPRN	**KRT1**	STXBP5L	Bt.65579	**APOA1**
KIAA0232	STXBP5L	SYNPO2	DOCK4	ABCC1	BSN	VPS35
KRT1	AGL	FAM179B	LOC787087	MKI67	ABCC1	AHSG
LOC531152	SYNPO2	SIPA1L3	MUC5B	GLT25D2	GRIN2B	COL4A6
PTPRS	HCFC1	Bt.63231	Bt.90677	COL4A6	HCFC1	ATAT1
MAGI1	PDGFRL	HBG	ATP6V1B1	BIRC6	HBG	AFAP1
NEB	**KRT1**	SYNE1	NPTX2	Bt.63231	TMCO7	CSN1S1

Table 4-3 25 most abundant coronal proteins associated with each nanotube. Boxed proteins are unique to that NT corona; bold proteins are common to all 7 NT coronas (from Table 4-2).

The 25 most abundant proteins in each corona are listed in Table 4-3. Of all protein corona constituents, the most abundant was Xin actin-binding repeat-containing protein 2 (XIRP2) and was found only in MWCNT-Pure, MWCNT-PVP and SWCNT-COOH coronas. XIRP2, aka mXinβ and myomaxin, is a 382,300 Da protein expressed in cardiac and skeletal muscle where it interacts with filamentous actin and α-actinin through the novel actin-binding motif, the Xin repeat [193], [194]. It is also the 40th most abundant protein in the FBS-supplemented culture medium. Like titin, this largely

abundant coronal protein is associated with intracellular filamentous proteins. The ample presence of XIRP2 in the media and in NT coronas may be in the form of protein fragments that are more common to fetal serum and less so in adult human or bovine sera where they are known to interact with albumin [195]. Other proteins may also be present in the protein corona via their association with BSA, as part of the albuminome [195–197]. For instance, the keratins identified in the protein coronas may be there through their interaction with albumin directly, or indirectly via their known interaction with apolipoproteins, which also interact with albumin [198]. While it is known that both intact and fragmented proteins exist in the serum and in association with albumin and other major serum proteins, their composition is beyond the scope of this investigation.

Unmodified MWCNT and SWCNT were found to bind a similar number of proteins (Figure 4-3A). Unmodified MWCNT were found to more readily associate α-1-antiproteinase (SERPINA1) and α-2-HS-glycoprotein (AHSG) than unmodified SWCNT (Table 4-3). The addition of carboxyl groups to the surface of SWCNT and MWCNT resulted in an increase in the number of types of protein which associated with the nanomaterials compared to non-functionalized SWCNT and MWCNT-Raw (Figure 4-3A). This increase in the number of proteins bound to carboxylated-NT is likely due to the abundance of protein amines in the medium which could readily associate with the carboxyls through electrostatic interactions. The lower zeta potential (Figure 4-2B) and higher protein binding capability of SWCNT COOH (Figure 4-3), compared with that of MWCNT COOH, can be attributed to the larger surface area and therefore higher density of COOH groups on the SWCNT surfaces. In addition, carboxylation of NTs was found

to increase binding of nuclear receptor coactivator-6, lactase-phlorizin hydrolase (NCOA6) and ATP-binding cassette subfamily A member 1 (ABCA1) compared to unmodified NTs (Table 4-3). PVP-coated MWCNT also demonstrated a slight increase in number of proteins bound compared to raw non-functionalized MWCNT, implying the more significant roles of hydrogen bonding and/or nonspecific electrostatic interactions with protein amines than hydrophobic interaction in NT-protein corona formation. Furthermore, PVP coating of MWCNT was found to increase association of ATP-binding cassette subfamily A member compared to unmodified MWCNT.

To determine distinctive corona profiles, proteins that were unique to each nanomaterial were examined (Figure 4-3B and Table 4-4). With only a few exceptions (collectin-12, G-protein coupled receptor 98, basement membrane-specific heparan sulfate proteoglycan core protein, kininogen-1, receptor-type tyrosine-protein phosphatase zeta, plasma serine protease inhibitor, and vitrin), these NT-specific, low abundance coronal components are proteins of intracellular origin with few or no extracellular domains, representing virtually every subcellular compartment and organelle (via Generic Gene Ontology (GO) Term Mapper [199] (http://go.princeton.edu/cgi-bin/GOTermMapper)). It is well known that the proteinaceous composition of serum/plasma includes a significant quantity of low molecular weight protein fragments derived from cell and tissue proteins [200], many of which are secreted and shed after degradation [201]. In fact, 70% of the FBS-DMEM components identified and quantified by LC-MS/MS are intracellular, as are most of the coronal components. It is likely that the cellular proteins were fragments and not whole

proteins as most were identified by 2 peptides and were in comparatively lower abundance than the conventional "serum" protein constituents. Perhaps these cellular fragments are the epitope motifs [115], [202] to which the cell responds upon initial interaction with the NP-corona complex, and this may account for the differential effects so often observed when cells are exposed *in vitro* to similar NPs with slight surface modifications.

COOH-functionalization of SWCNT and MWCNT was found to increase the number of unique proteins which associated the NTs compared to non-functionalized raw NTs (Figure 4-3B), pointing to the role of covalent bonding between the carboxyls of the NTs and amines of the proteins in corona formation. Numerous low-abundance "cellular" proteins were found to be unique to the protein coronas of specific NT types. These NT-specific proteins are listed, along with their abundances, in Table 4-4.

Table 4. Proteins Unique to Nanotube Coronas

	Protein ID	Gene Name	Protein Name	Quantity
Reference Proteins*				
	P15497	APOA1	Apolipoprotein A-I	30,219,499
	P02769	ALB	Serum albumin	172,526,039
	F1N757	TTN	Titin	234,480,064
Nanoclay				
	F1MPT5	DST	Dystonin	3,861,367
MWCNT-Pure				
	G3MX12	HERC2	E3 ubiquitin-protein ligase HERC2	1,735,859
	F1MLJ1	PCDHB1	Protocadherin beta-1	3,155,333
	E1BEW9	WDR87	WD repeat-containing protein 87	6,299,685
	E1BGJ0	LRP1	Prolow-density lipoprotein receptor-related protein 1	7,429,100
	F1MYW0	NT5DC3	5'-nucleotidase domain-containing protein 3	11,721,867
	Q32PG0	WWP1	NEDD4-like E3 ubiquitin-protein ligase WWP1	12,260,233
MWCNT-Raw				
	P01044	KNG1	Kininogen-1	1,012,523
	F1MW73	MGC148692	KIAA1211 protein	1,568,099
	F1MSG6	RAPGEF2	Rap guanine nucleotide exchange factor 2	1,952,045
	Q2KHZ2	HBS1L	HBS1-like protein	4,041,483
	F1MAX6	KATNAL1	Katanin p60 ATPase-containing subunit A-like 1	4,289,983
	F1N300	Bt.76801	Condensin complex subunit 1	4,804,233
	F1MYB0	STOX2	Storkhead-box protein 2	7,332,400
SWCNT-Raw				
	F1MER7	HSPG2	Basement membrane-specific heparan sulfate proteoglycan core protein	1,610,263
	Q9TTA5	SMARCAL1	SWI/SNF-related matrix-associated actin-dependent regulator of chromatin subfamily A-like protein 1	3,302,833
	F1MIU48	TOP2B	DNA topoisomerase 2-beta	43,838,728
MWCNT-PVP				
	E1BA03	PAK6	Serine/threonine-protein kinase PAK 6	1,362,630
	E1BIU4	ZC3H7B	Zinc finger CCCH domain-containing protein 7B	3,710,533
	Q0III9	ACTN3	Alpha-actinin-3	3,886,300
	F1N0S1	ASAP3	Arf-GAP with SH3 domain, ANK repeat and PH domain-containing protein 3	3,987,033
	E1BAU4	PCDH17	Protocadherin-17	5,714,533
	F1N0V8	GLT25D2	Procollagen galactosyltransferase 2	8,720,067
MWCNT-COOH				
	Q95LI2	VIT	Vitrin	1,199,471
	E1BIN0	FHOD1	FH1/FH2 domain-containing protein 1	2,041,853
	A6QLR2	LARS	Leucine--tRNA ligase, cytoplasmic	2,665,600
	G3MXX3	Bt.103298	Chromodomain-helicase-DNA-binding protein 2	2,725,444
	F1MX14	MDGA2	MAM domain-containing glycosylphosphatidylinositol anchor protein 2	2,883,907
	E1BMN2	DIAPH3	Protein diaphanous homolog 3	3,074,724
	Q9N2I2	SERPINA5	Plasma serine protease inhibitor	3,212,431
	F1MD25	C11orf41	UPF0606 protein C11orf41	3,495,796
	G3MW09	Bt.82323	Multidrug resistance-associated protein 4	3,590,753
	E1BA65	PMS2	Mismatch repair endonuclease PMS2	3,647,800
	E1BA80	MYO18B	Unconventional myosin-XVIIIb	3,683,443
	Q0P5J8	FAM40A	Protein FAM40A	4,130,100
	F1MC84	FAT3	Protocadherin Fat 3	4,947,628
	A6QP52	SMTN	Smoothelin	5,745,756
	E1BG99	EIF4ENIF1	Eukaryotic translation initiation factor 4E transporter	6,688,973
	F1MCL3	GRIN2B	Glutamate [NMDA] receptor subunit epsilon-2	9,710,800
SWCNT-COOH				
	Q3B7M1	KLHL36	Kelch-like protein 36	1,188,690
	F1MGS8	NAALAD2	N-acetylated-alpha-linked acidic dipeptidase 2	1,567,551
	A6H709	HSPC321	Switch-associated protein 70	2,022,833
	F1MLF8	HGD	Homogentisate 1,2-dioxygenase	2,023,368
	E1AXU0	CMYA1	Cardiomyopathy associated protein 1	2,282,263
	F1MUL5	FAAH	Fatty-acid amide hydrolase 1	2,797,818
	E1B8Z3	DAAM2	Dishevelled-associated activator of morphogenesis 2	2,931,789
	E1BKS0	EPS8L1	Epidermal growth factor receptor kinase substrate 8-like protein 1	3,173,085
	E1BG53	PPARGC1B	Peroxisome proliferator-activated receptor gamma coactivator 1-beta	3,176,827
	E1BCY7	Bt.45696	Tyrosine-protein kinase SgK223	3,261,906
	F1MS10	Bt.65326	Dynein heavy chain 5, axonemal	3,374,833
	E1BGY9	JPH3	Junctophilin-3	3,405,295
	G3X7Z2	CACNA1B	Voltage-dependent N-type calcium channel subunit alpha-1B	3,413,133
	Q27991	MYH10	Myosin-10	3,774,257
	E1BGB2	PRRC2B	Protein PRRC2B	4,048,033
	E1BMG2	DNAH5	Dynein heavy chain 5, axonemal	4,183,145
	F1MH31	NUP214	Nuclear pore complex protein Nup214	4,619,333
	F1N0J3	ATP11A	Probable phospholipid-transporting ATPase IH	4,793,946
	G3N0C1	ANK2	Ankyrin-2	4,822,700
	F1MJJ0	DNAH9	Dynein heavy chain 9, axonemal	4,856,533
	F1N0A6	GPR98	G-protein coupled receptor 98	5,075,200
	E1BKO9	GALNT5	Polypeptide N-acetylgalactosaminyltransferase 5	5,084,459
	O02776	PARG	Poly(ADP-ribose) glycohydrolase	5,477,200
	F1N6H4	MACF1	Microtubule-actin cross-linking factor 1	6,296,211
	F1MI56	ANKRD17	Ankyrin repeat domain-containing protein 17	6,637,200
	E1BC55	LOC533883	Uncharacterized protein KIAA1671	6,824,667
	F1MNA8	ZMYM2	Zinc finger MYM-type protein 2	7,565,700
	F1MGK5	PTPRZ1	Receptor-type tyrosine-protein phosphatase zeta	7,929,133
	F1MYC9	SPTBN1	Spectrin beta chain, brain 1	8,029,370
	E1BM04	TBKBP1	TANK-binding kinase 1-binding protein 1	8,685,600
	F1MC30	GCNT4	Beta-1,3-galactosyl-O-glycosyl-glycoprotein beta-1,6-N-acetylglucosaminyltransferase 4	9,650,800
	E9QB09	WC1	WC1 (CD4-CD8- gamma delta T lymphocyte proteins)	10,846,900
	A6QP79	COLEC12	Collectin-12	12,443,233
	F1MFX9	PRKAG2	5'-AMP-activated protein kinase subunit gamma	12,863,582

*found in all NT coronas; mean quantity shown

Table 4-4 Proteins unique to nanotube coronas. * found in all NT coronas; mean quality shown.

Surprisingly, despite the prevalence of *in vitro* nanotoxicology investigations, only two studies have attempted to identify and characterize fetal bovine serum proteins and their quantitative composition via SDS-PAGE separation and identification by LC-MS/MS in coronas formed during *in vitro* NP exposures: citrate capped gold NP coronas [170] and magnetic iron oxide NP coronas [203]. The electrophoretic approach used to separate and detect coronal constituents in these studies may have limited the number of proteins actually identified. All other previous studies of corona composition of NPs using proteomic techniques have focused on human plasma/sera or cytosols and include: amorphous silica [184]; polystyrene [185]; sulfonated polystyrene and silica [204]; atheronal-b and cholesterol coated quantum dots [205]; lipoplexes and liposomes [206–210]; carboxyl-modified polystyrene [121]; carbon NTs and metal oxide [211] and surface-functionalized gold in cell lysate proteins [167]. The studies have used SDS-PAGE followed by LC-MS/MS identification.

Similar to our current study, Zhang et al. identified and quantified 88 distinct human plasma proteins by stable isotope labeling and LC-MS/MS on polystyrene NPs in which protein corona composition was surface modification-dependent [185]. Twelve of the 88 proteins identified in the coronas of these polystyrene NPs were also common to our FBS-DMEM protein corona profile for all nanomaterials assessed (plasma serine protease inhibitor, apolipoprotein A-I, apolipoprotein A-II, fibrinogen alpha chain, alpha-2-HS-glycoprotein, serotransferrin, kininogen-1, alpha-1-antitrypsin, vitamin D-binding protein, albumin, complement C3 and complement C4). Unlike the high proportion of cellular protein corona constituents observed in our study, only about 34% of Zhang et

al.'s coronal proteins were intracellular. Interestingly, when Capriotti et al. used LC-MS/MS to study the protein composition of coronas that formed on nanosized cationic liposomes (CLs), lipoplexes, and lipid/polycation/DNA (LPD) complexes exposed to human plasma roughly 70% of the 218 proteins were intracellular, similar to our results in high aspect-ration NTs [207]. In a subsequent quantitative analysis, coronal protein variety found on lipoplexes and LPD complexes was greater than that found on cationic liposomes while individual protein abundance differed as well [210], again, similar to our observations in NT coronas. Compared to these studies in human plasma/sera or cytosols our current study provides information useful in interpreting and evaluating *in vitro* nanomaterial toxicity studies. Taken together these previous studies and our current study may assist with the extrapolation of *in vitro* nanomaterial toxicity data to relevant *in vivo* interactions and human exposures.

4.4 Conclusion

NT protein coronas formed *in vitro* by exposure to FBS-DMEM media are extremely complex as others using comprehensive proteomics and human plasma have observed. Although typical serum proteins are abundant components of the protein coronas, the latter also contain a large amount of proteins/protein fragments of cellular origin. This provides a diverse composition of the each nanomaterial's protein corona which varies based on physicochemical differences. Factors such as nonspecific hydrogen bonding, electrostatic interaction and the specific covalent bonding between the

carboxyls of the NTs and amines of the proteins are likely responsible for the differences in protein corona composition. Since functionalized NTs bound similar quantities of proteins compared to pristine NTs, hydrophobic interactions and π-stacking between the aromatic moieties of the proteins and the aromatic groups of the NTs are deemed less significant in NT-protein corona formation. Although SWCNT-COOH and MWCNT-COOH were found to possess comparable hydrodynamic sizes, the conceivably more rugged surface morphology (due to bundling) and higher charge density of the former led to a slightly more robust binding of plasma proteins in both total number and structural uniqueness. These unique constituents of protein corona, even those in low abundance may cause unique cellular effects and bioactivity in *in vitro* nanotoxicology assessments.

CHAPTER 5. INTERACTION OF NANOPARTICLE-CORONA WITH BIOLOGICAL SYSTEMS

In chapter 5, the formation of NP-protein corona and the interaction of such corona with both simplified model and real biological systems are presented. First, lipid vesicles were developed to represent the physical aspects of a mammalian cell, and changes in the vesicle fluidity upon their interaction with pre-formed NP-protein corona were examined. Second, a scheme of protein corona-cell interaction is presented to determine the fate of such corona after being taken up by the cell.

5.1 Interactions of Silver Nanoparticle-Serum Albumin Protein Corona with Lipid Vesicles

The first half of chapter 5 examines the physical interaction between a lipid vesicle and an AgNP-HSA protein "corona". Specifically, the binding of AgNPs and HSA was analyzed by spectrophotometry and the induced conformational changes of the HSA were inferred from circular dichroism spectroscopy. The fluidity of the vesicle, a model system for mimicking cell membrane, was found to increase with the increased exposure to AgNP-HSA corona, though less pronounced compared to that induced by AgNPs alone. This study offers new information for understanding the role of physical forces in NP-cell interaction and has implications for nanomedicine and nanotoxicology.

5.1.1 Introduction

Understanding biological response to engineered nanomaterials is essential to the continued development of nanomedicines, whose expanding repertoire includes design of novel assemblies for gene and drug delivery and of highly specific and localized bioimaging and disease and tumor detection. On the other hand, the mass production of nanomaterials and rapid commercialization of nanotechnologies further justifies research addressing occupational and environmental exposure to administered or accidentally released NPs.[5], [69], [212], [213] Central to these crucial research needs is a mechanistic description of the unique interplay between biological systems and engineered nanomaterials,[5], [212], [213] especially at the cellular level which manifests the unit of life.

It has been realized that NPs, upon their entry into the bloodstream or -- more generically -- when dispersed in a biological fluid, interact readily with proteins, peptides, amino acids, fatty acids, lipids, and other soft and organic matter.[214–216] Consequently, the NPs acquire an enhanced mobility as well as biocompatibility and may elicit their impact on the host system through a collective entity of NP-protein "corona", rather than the physicochemistry of the NP "core" alone.[107], [211], [214–217] Such NP-protein corona may further initiate its contact with the cell through physical adsorption or recognition by the membrane receptors specific for the proteins that constitute the corona. Uptake of NPs is thought -- as agreed upon by a majority of the research community -- to be realized via the energy-dependent biological process of endocytosis, in addition to passive diffusion and mechanical or biochemical damage in the lipid membrane induced by the trespassing NP.[5] However, despite intensive

research efforts, both experimentally[17], [59], [81], [130–132], [148], [218–220] and through atomistic and coarse-grained computer simulations,[82], [83], [221–223] it remains unclear and often controversial as to what extent the thermodynamic and endocytotic pathways may individually contribute to the convoluted process of NP cell uptake.

Here we demonstrate a facile method of examining the physical interaction between a lipid vesicle -- a model cell membrane -- and a NP-protein corona. The lipid vesicle consists of zwitterionic DMPC doped with 10% anionic dimyristoyl phosphatidylglycerol (DMPG). The equal chain length of the fatty acyl tails and comparable head group sizes of DMPC and DMPG minimized phase separation in the vesicle.[224] Physically, a dipole moment existed in DMPC that pointed from the O^- to the N^+ within the lipid head, while only a negatively charged O^- was present in the lipid head of DMPG (Figure 5-1). Such net negative charge of the vesicle, afforded by the 10% DMPG lipids, conformed to the natural composition of weakly negative charge of cell membranes. In addition, the consideration of protein corona, instead of bare NP "core" alone, provided a more realistic system for examining the physical interactions between NPs and the cell.

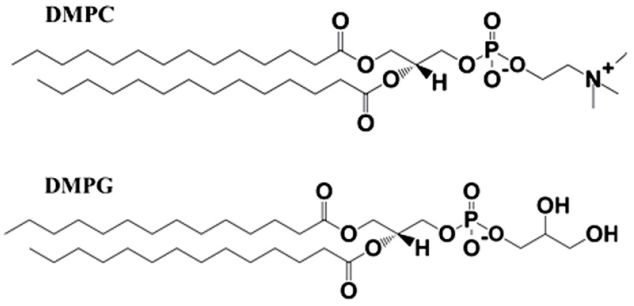

Figure 5-1 Chemical structures of DMPC and DMPG.

5.1.2 Results and Discussion

AgNPs (coated with citrate) were purchased from NanoComposix and used in our experiments. HSA (MW: 66,478) proteins were obtained from Sigma. Silver NPs were selected due to their increasing mass production and domestic use,[225] while the selection of HSA was based on its high abundance among plasma proteins. The zeta-potentials of AgNPs and HSA in Milli-Q water (pH = 6.5) were determined to be -31 mV and -17 mV, respectively (ZetaSizer Nano, Malvern). The stronger surface charge provided a stable suspension for AgNPs, while HSA molecules could be multimeric due to their weaker charge. AgNPs and HSA of molar ratios from 1:6 to 1:392 were incubated at room temperature for 1 h and the hydrodynamic sizes of their mixtures were determined by DLS (Nanosizer S90, Malvern). Figure 5-2 shows the increased size with the increased ratio of HSA to AgNPs. Multi-layer coating of HSA onto AgNPs was evident at the molar ratio of 1:122 and above, considering the size of an HSA monomer is ~8 nm.[226] The formation of AgNP-HSA corona was confirmed by transmission

electron microscopy (TEM, Hitachi H7600), where AgNPs (4.92×10^{-4} μM) were incubated with HSA (7.16 μM) at 4℃ overnight and negatively stained with phosphotungstic acid for 45 min prior to imaging. The average size of bare AgNPs was ~30 nm, in agreement with that provided by the vendor (Figure 5-3 left panel). With incubation a thick layer of optically less dense material, believed to be HSA, was clearly visible on the AgNP surfaces (Figure 5-3 right panel). The size of the AgNP-HSA corona determined by TEM was ~80 nm, in agreement with the DLS measurement. Since both the AgNPs and the HSA were net negatively charged, the formation of AgNP-HSA corona could result from the hydrophobic surface moieties of the AgNPs interacting with the hydrophobic domains of the HSA, as well as hydrogen bonding between the hydroxyls or oxygens of the citrate coating on the AgNPs and the nitrogen or sulfur electron acceptors or donors on the HSA.

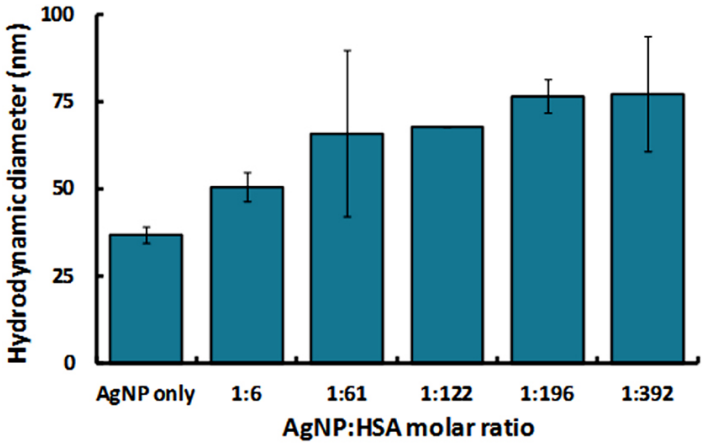

Figure 5-2 Hydrodynamic sizes of AgNP-HSA at molar ratios of 1:6 to 1:392. Incubation: 1 h.

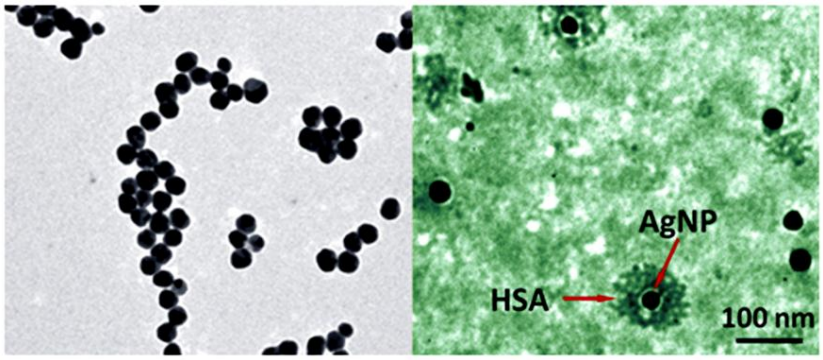

Figure 5-3 TEM images of bare AgNPs (left panel) and AgNP-HSA corona (right panel).

The formation of AgNP-HSA corona was further confirmed by measuring the absorption spectra of AgNPs (9.8×10^{-5} μM), HSA (1.42 μM) and their mixture AgNP-HSA using a UV-vis spectrophotometer (Cary 300 BIO, Varian). As shown in Figure 5-4 inset, a characteristic peak of SPR was identified for AgNPs at 404 nm. After incubation with HSA, the absorption peak was red-shifted to 412 nm. This phenomenon can be understood by the following analysis. Assume the dielectric constant of an AgNP relative to its surrounding medium is $\varepsilon = \frac{\varepsilon_s}{\varepsilon_m} = \varepsilon' + i\varepsilon''$, where ε_s and ε_m are the dielectric constants of the AgNP and the medium respectively. Here ε' is negative and decreases with the increasing wavelength of light, while ε'' is approximately constant for wavelength longer than 300 nm. According to the Clausius-Mossotti relation,[25] the extinction cross-section of the AgNP can be expressed as $C_{ext} \propto \frac{1}{(2+\varepsilon')^2 + \varepsilon''^2}$, and its extinction peak occurs at ε' = -2, or $\mathrm{Re}(\varepsilon_s) = -2\varepsilon_m$. Thus when ε_m was increased due to the binding of

(dielectric) HSA molecules onto the AgNP, a red-shift in wavelength occurred for the extinction to reach its new peak value.

To examine the physical interaction between AgNP-HSA and cell membranes, artificial vesicles were generated by lipid extrusion. Specifically, 10 mg of DMPC lipids, doped with 10% DMPG, were first dissolved in 1 mL of chloroform in a flask, and then dried under airflow to form thin lipid sheets on the flask bottom. After that 1 mL of Milli-Q water (at 30 ℃) was added to the flask to hydrate the lipid sheets and the mixture of lipids and water was agitated for ~2 min to form large multilamellar vesicles (LMV). This process was performed in a warm water bath to avoid gel-liquid crystal transition. A water-bath sonication was then applied to the mixture for 5 to 10 min to form large unilamellar vesicles (LUV). After sonication, the vesicle suspension was extruded through a porous polycarbonate membrane (pore size: 100 nm) to yield uniformly sized LUV (100 nm). In particular, for the detection of vesicle phase transition, Laurdan dye was added to the chloroform solution to partition into the vesicle bilayers.

To investigate the effect of AgNP binding on the conformation of HSA, circular dichroism (CD) spectroscopy was performed. AgNPs and HSA were incubated for 8 h prior to the measurement, using the same molar ratio but diluted 16× as in the UV-vis measurement to comply with the sensitivity of the spectropolarimeter (Jasco J-810). The vesicle-HSA sample was prepared by mixing the DMPC vesicles (10% DMPG-doped) and HSA immediately before the CD measurement. The vesicle-AgNP-HSA sample was obtained from the mixture of DMPC vesicles (10% DMPG-doped) and pre-formed AgNP-HSA corona. The CD spectra were acquired at room temperature over a

wavelength range of 200-300 nm using quartz cuvettes, and were averaged over three scans taken at a speed of 50 nm/min. The backgrounds of the AgNPs and vesicles were subtracted accordingly.

The readout values of the HSA ellipticity (θ, in mdeg) were converted to a standard unit of deg·cm^2/dmol ([θ]) using equation $[\theta] = (\theta \times M_0)/(10000 \times C_{soln} \times L)$, where M_0 is the mean residue molecular weight (118 g/mol), C_{soln} is the protein concentration in solution (in g/mL), and L is the path length through the buffer (1 cm). As shown in Figure 5-4, the α-helix content in HSA decreased by 15.7% after incubation with AgNPs, compared to that for the native state of HSA, and decreased by 18.4% after incubation with the vesicles. However, incubating vesicles with the pre-formed AgNP-HSA corona reversed the conformational change of HSA induced by AgNPs, causing a decrease of only 3.2% in the α-helix content of the HSA. For β-sheets, increases of 5.8% and 15.9% were observed for the samples of AgNP-HSA and vesicle-HSA respectively, and a decrease of 7.3% was measured for the sample of vesicle-AgNP-HSA, compared to that for the sample of HSA alone. These results suggest that, in the presence of either vesicles or AgNPs, HSA could undergo significant conformational changes to alter its α-helices into β-sheets and other secondary structures. Such changes can be attributed to the interaction between the hydrophobic domains in the HSA and the hydrophobic surface areas of the AgNPs, and electrostatic attraction between the negatively charged surface domains of HSA and the positively charged DMPC lipid head groups. In contrast, the net negative charge of the vesicles further compromised the relatively weak affinity of the

negatively charged AgNPs for the HSA, leading to the partial recovery of protein conformation.

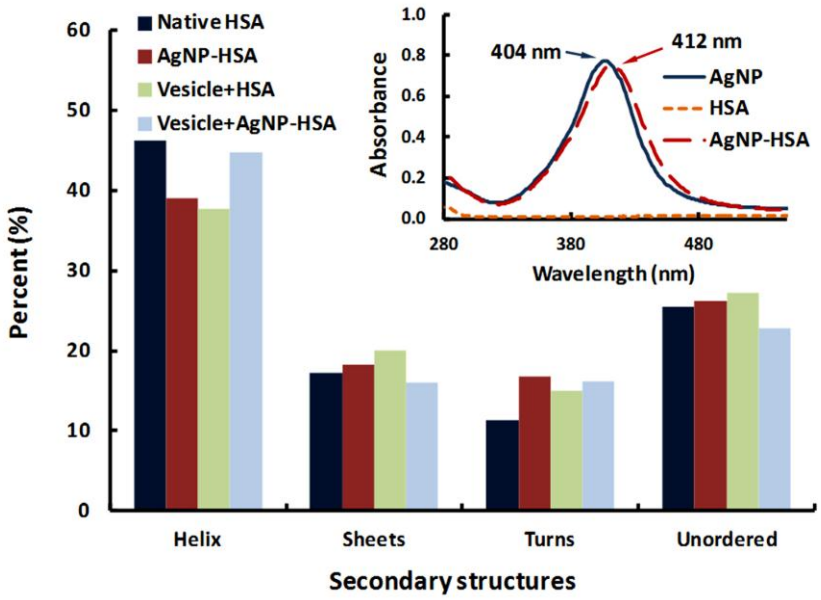

Figure 5-4 Percent of secondary HSA structures inferred from the CD spectra for native HSA, HSA pre-incubated with AgNPs, HSA in the presence of vesicles, and HSA pre-incubated with AgNPs in the presence of vesicles. Inset: UV-vis spectra showing a red-shift of the extinction peak of AgNPs pre-incubated with HSA. Pre-incubation time: 8 h.

The effect of AgNP-HSA protein corona on the fluidity of DMPG-doped DMPC vesicles was evaluated based on the fluorescence emission of the Laurdan dyes partitioned within the vesicle bilayers (Figure 5-5). First, samples of AgNP-HSA mixtures were prepared at different concentrations (6.15×10^{-7} to 492×10^{-7} μM for AgNPs and, accordingly, 8.95×10^{-3} to 716×10^{-3} μM for HSA) and incubated at 4 ℃ overnight to

ensure the equilibrium of their binding. Then the samples were separately added to the vesicle suspensions of 0.05 mg/mL. A spectrofluorometer (Cary Eclipse, Varian) was used to excite the Laurdan at 340 nm and the fluorescence intensities of the dyes were collected at both 416 nm and 473 nm to derive the GP values for the vesicles:[17], [81] $GP = \frac{I_{416} - I_{473}}{I_{416} + I_{473}}$. An increasing GP value indicates a phase transition toward gelatin, while a decreasing GP value represents fluidization. The spectrofluorometer chamber was operated at 25 ℃, above the lipid phase transition temperature. Measurements were repeated for AgNPs and HSA respectively.

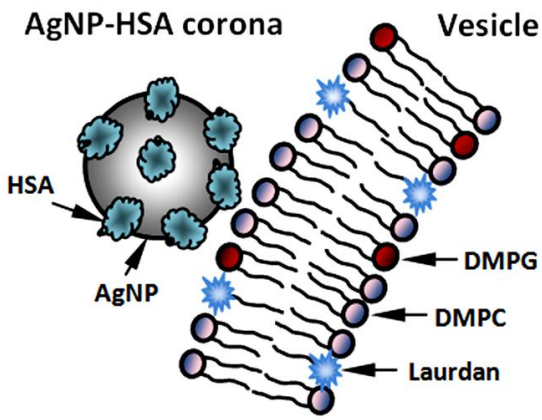

Figure 5-5 Schematic of AgNP-HSA corona interacting with a Laurdan-labeled, DMPG-doped DMPC vesicle.

Compared with the control vesicles, HSA showed little impact while both AgNPs and AgNP-HSA gave rise to decreased GP values in the vesicles (Figure 5-6). This indicates an enhanced fluidization of the vesicle bilayers, which may be attributed to the

structural reorganizations of the vesicles in response to the NP adsorption. In addition to the prevalent weak forces of hydrogen bonding and vdW interaction, strong and long range electrostatic interactions between the charged domains of the lipids (N^+ in the DMPC and O^- in the DMPG, Figure 5-1) and that of the AgNPs (e.g., citrate coating) or AgNP-HSA also took place to alter the vesicle fluidity. As shown in Figure 5-6, at low NP/protein concentrations, the effect of AgNPs on vesicle fluidity was similar to that induced by AgNP-HSA, implying that both AgNPs and HSA in the corona interacted with the lipid vesicles. In contrast, at high NP/ protein concentrations, due to the presence of excess unbound HSA molecules, the vesicles experienced less perturbation from the AgNPs in the corona than from bare AgNPs.

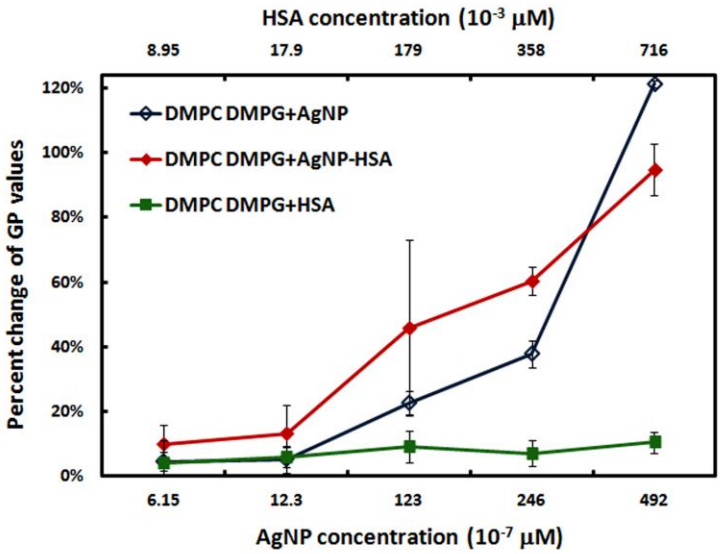

Figure 5-6 Percent change of GP values for vesicles incubated with different concentrations of AgNPs, HSA, or AgNP-HSA. The concentration of the (DMPC+10% DMPG) lipids was 0.05 mg/mL for all cases. The percent changes were calculated by

comparing the actual GP values of the samples with that of the vesicle suspension (control). Since the GP values of the control were negative, a positive percent change corresponds to a decreasing GP value.

5.1.3 Conclusion

Taken together the results from the UV-vis, TEM and CD measurements, it is evident that the binding of AgNP-HSA was primarily mediated by the physical forces of hydrogen bonding, electrostatic interaction, and hydrophobic interaction. Upon the formation of AgNP-HSA corona the percent of α-helices was reduced while that of β sheets was increased in the HSA secondary structures, possibly resulting from breakage of the hydrogen bonds between neighboring α-helices and configuration of new, sterically less ordered hydrogen bonds between the α-helices and the citrate coating of the AgNPs. As shown in the CD measurement, the presence of lipid vesicles alleviated the conformational changes of the proteins induced by the NPs, likely due to the electrostatic repulsion between the vesicles and the NPs. Conversely, the GP measurement demonstrated that both NPs and protein corona interacted with lipid vesicles to enhance fluidity of the latter, although free proteins did not exert much effect on the vesicle conformation. Overall, our study suggests that the formation of NP-protein corona may negate, to certain extent, the physical interactions between the NP core and cell membranes. Such physical perspective, when combined with the biological and biochemical mechanisms of endocytosis, lipid peroxidation, and enzymatic activity,[49]

may prove essential for our understanding and prediction of the behavior of nanomaterials in biological systems for the advancement of nanomedicine and nanotoxicology.

5.2 Formation and Cell Translocation of Carbon Nanotube-Fibrinogen Protein Corona

The second half of chapter 5 examines the binding of plasma fibrinogen (FBI) with both single-walled and multi-walled carbon nanotubes (SWNTs and MWNTs). Specifically, our absorbance study indicated that MWNTs were coated with multi-layers of FBI to render a "hard protein corona", while SWNTs were adsorbed with thin layers of the protein to precipitate out of the aqueous phase. In addition, static quenching as a result of energy transfer from fluorescently labeled FBI to their nanotube substrates was revealed by Stern-Volmer analysis. When exposed to HT-29 cells, the nanotubes and FBI could readily dissociate, possibly stemming from their differential affinities for the amphiphilic membrane bilayer.

5.2.1 Introduction

Carbon-based nanomaterials have been studied extensively over the past two decades for their unique physical properties and vast potential in electronics, imaging, sensing, biotechnology, and environmental remediation. CNTs, a major class of carbon-based nanomaterials, are especially attractive for biological and medicinal applications owing to their large surface area, high aspect ratio, and simplicity for accommodating

chemical groups and drug loads.[227] However, integrating carbon nanomaterials with biological systems must first address the inherently poor solubility and biocompatibility of the engineered materials, on molecular, cellular and whole organism levels.[5], [212]

The solubility and biocompatibility of carbon-based nanomaterials may be afforded or enhanced through specific surface functionalization or nonspecific adsorption of proteins, lipids, amino acids, and nucleic acids.[228–232] Alternatively to such purposeful surface modifications, NPs voluntarily assume the form of a NP-protein "corona" upon entering living systems,[215] resulting from their surface adsorption by plasma proteins and other biomolecular species. Naturally, understanding the formation of NP-protein corona has become a focused area of study due to its great relevance to delineating the fate and toxicity as well as facilitating the biological and medicinal applications of nanomaterials.[202]

The currently accepted paradigm assumes that the formation of NP-protein corona depends upon the physicochemical properties of the NPs (surface charge, coating, shape, roughness, and reactivity), the solvent (pH, ionic strength, and temperature), and the proteins (amphiphilicity, charge, p*Ka*, chemical composition, and folding dynamics).[202], [216], [233] In addition, plasma proteins may exhibit short ("soft") or long-term ("hard") residence times on their NP substrates,[234] derived from the cooperativity (the Vroman effect,[118] folding/unfolding) between the proteins convolved with the protein affinity for the NP substrates mediated by electrostatic and hydrophobic interactions, vdW forces, and hydrogen bonding.

5.2.2 Results and Discussion

In consideration of the vast biological and medicinal potentials of carbon-based nanomaterials, we have examined the binding of both SWNTs and MWNTs with FBI, a major class of plasma glycoprotein that is essential for the coagulation of blood. It is shown through this study that the formation and stability of CNT-FBI coronas correlate with the differential surface areas of the two types of CNTs, as indicated by our UV-vis spectrophotometry and electron and fluorescence measurements. In addition, we have determined that the binding of fluorescently labeled FBI onto CNTs induced static (and possibly dark) quenching of the protein fluorescence. Utilizing the energy transfer between labeled FBI and CNTs (Figure 5-7), we have shown that CNT-FBI coronas could dissociate upon cell translocation, likely as a result of the different affinities of the proteins and the nanostructures for the membrane bilayers. The knowledge derived from this biophysical study complements the existing proteomic, thermodynamic, and chromatographic studies of NP-protein corona,[111], [202], [211], [217], [233], [234] and may benefit both *in vitro* and *in vivo* evaluations of biological responses to intentionally administered or accidentally released nanomaterials.

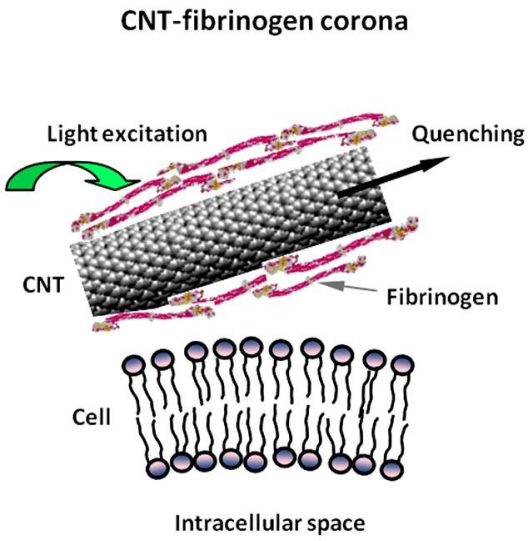

Figure 5-7 Schematic of the present study, showing quenching of FBI fluorescence as a result of energy transfer from the proteins to their CNT substrate and translocation of CNT-FBI across a cell membrane.

SWNTs (diameter: 1.4 nm, length: 0.5-3 μm, 5% impurities) and MWNTs (OD: 40-70 nm, ID: 5-40 nm, length: 0.5-2 μm) were purchased from Carbon Nanotechnologies and Sigma. Bovine plasma FBI (termed as "unlabeled FBI", MW: 330kDa) and Alexa Fluor 546-labeled human plasma FBI (termed as "labeled FBI", ~15 dyes per FBI, Ex/Em: 558/573 nm) were received from Sigma and Invitrogen. The surface areas of SWNTs and MWNTs (in powder form) were derived from the Brunauer-Emmett-Teller (BET) equation[235] and the Barrett-Joyner-Halenda (BJH) method[236] as 855 and 104 m^2/g, respectively, using a physisorption analyzer (Micromeritics ASAP 2010).

The formation of CNT-FBI coronas was first visualized by scanning electron microscopy (SEM) imaging (Figure 5-8). Specifically, CNTs and unlabeled FBI were mixed with Milli-Q water to final concentrations of 0.3 and 0.4 mg/mL respectively and incubated overnight. The CNT-FBI samples were then deposited onto aluminum substrates and air-dried. A Hummer 6.2 (Anatech) sputter was used to pre-coat the samples with a 2-4 nm layer of platinum for 1 min (pressure: 80 milli-torr, voltage: 15 mA). SEM imaging of the CNT-FBI protein coronas was then performed using a Hitachi S4800 electron microscope, at accelerating voltages of 10-15 kV. FBI coated both the SWNTs and MWNTs fully, and especially in the case of MWNTs the protein agglomeration on the nanotube surfaces appeared complex in morphology. This is likely due to the bundling of the SWNTs (Figure 5-8, SWNTs control), whose surface roughness and grooves could promote the predominantly axial orientations of the tubular FBI. In comparison, the larger and flatter MWNT surfaces should be less restrictive for the binding of the protein.

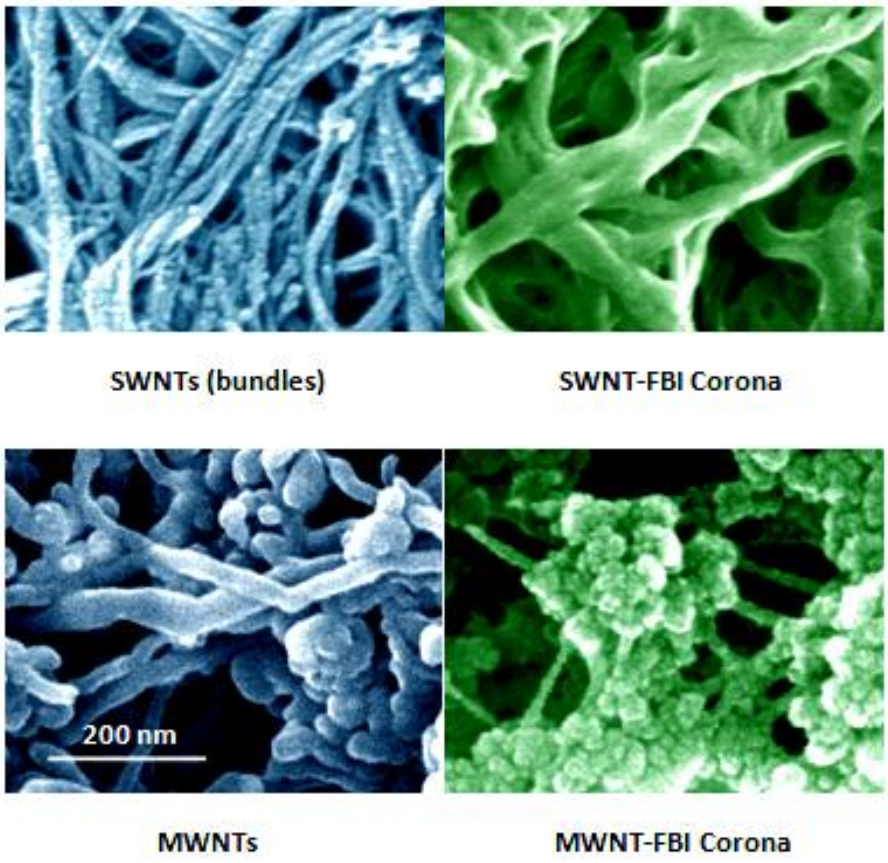

Figure 5-8 SEM images of SWNT bundles, SWNT-FBI coronas (top panels), MWNTs, and MWNT-FBI coronas (bottom panels). Scale bar: 200 nm for all panels.

The stabilities of the CNT-FBI coronas were characterized by a Cary 300 BIO spectrophotometer (Varian). SWNTs and MWNTs were mixed separately with unlabeled FBI in Milli-Q water (pH 6.5) to render final concentrations of 0.5 mg/mL for both types of the CNTs and 2.5 mg/mL for the protein, respectively. The absorbance of the CNT-FBI mixtures was measured at 280 nm, corresponding to the wavelength where the tryptophan residues in FBI exhibited a peak absorbance. The absorbance measurement was conducted for 10 h, at a time interval of 30 min. As shown in Figure 5-9, the

absorbance dropped exponentially until stabilized after ~400 min for the SWNT-FBI sample, while it remained very stable for the MWNT-FBI sample over the entire course of 10 h. This result suggests that the SWNT-FBI coronas were "softer" than the MWNT-FBI, a proposition also corroborated by our analysis below. In addition to vdW force, hydrophobic interaction, as well as π-stacking which could underlie the formation of CNT-FBI coronas, FBI could also initiate hydrogen bonding between adjacent CNT-FBI coronas. In the case of SWNTs such inter-corona interaction could further destabilize the protein coating to induce precipitation.

The two different trends of protein absorbance in Figure 5-9 can be analyzed using the Mason-Weaver differential equation:[237] $\frac{\partial c}{\partial t} = D\frac{\partial^2 c}{\partial t^2} + sg\frac{\partial c}{\partial z}$, where c is concentration of the solute (i.e., the CNT-FBI corona), D and s are the solute diffusion constant and sedimentation coefficient, z is a length parameter, and g is the acceleration of gravity. Based on the fitted exponents of -0.007 (for SWNTs) and 0 (for MWNTs) in Fig. 2a, the value of $4D/(sg)^2$ was calculated as 136.7 min for SWNTs and infinity for MWNTs. Assuming m_0 and m_b are the actual and buoyant mass of the solute, ρ_f and ρ_0 the densities of the solute and water, k_b the Boltzmann constant, and T the temperature, and evoking equations $m_b = m_0(1-\rho_f / \rho_0)$ and $s/D = m_b / k_b T$ derived from the Einstein relation we estimate that SWNT-FBI possessed an effective density of 1.36 g/cm^3 while MWNT-FBI assumed an effective density approximately equal to that of water. Since the density of SWNTs is ~1.4 times that of water[238] and is only slightly higher than that of SWNT-FBI, we conclude that SWNT bundles were coated with thin layers of FBI to

elicit a poor stability in water. In contrast, our analysis implies that MWNTs were adsorbed with multilayers of the protein to render a hard corona.

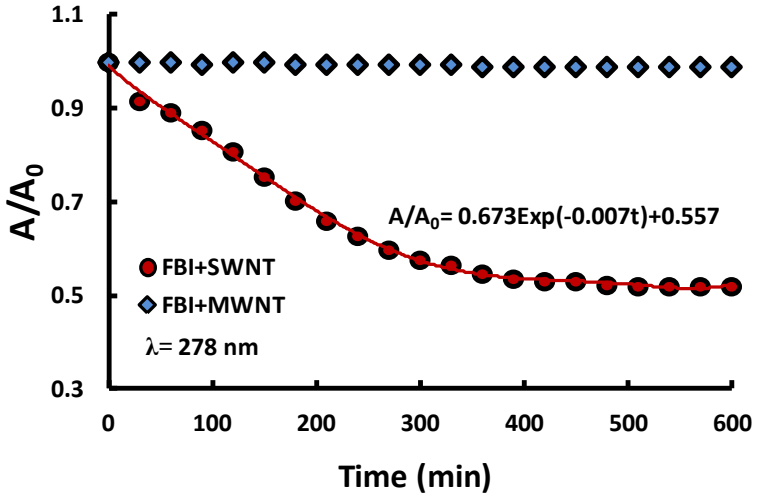

Figure 5-9 Normalized absorbance curves showing the stability of CNT-FBI coronas for both SWNTs (blue diamonds) and MWNTs (red circles) over 10 h.

Fluorescence spectroscopy was utilized to yield more insight on the binding of CNTs and FBI. Specifically, 3 mg of SWNTs and MWNTs were each added to 3 mL of Milli-Q water and bath sonicated for 1 h. The CNTs were then mixed individually with 66.7 μL of the labeled-FBI (1.5 mg/mL) and Milli-Q water to yield samples containing 10-80 μg/mL of SWNTs, 100-800 μg/mL of MWNTs, and 100 μg/mL of labeled FBI. The CNT-labeled FBI samples were then bath sonicated (Precision, Thermo) for 15 min and incubated for 1 h on a rotator. After that the CNT-labeled FBI mixtures were centrifuged at 12,100 RCF (13,400 RPM) for 15 min and supernatants containing free,

labeled FBI molecules were collected. Fluorescence intensities (Ex/Em: 558 nm/565-585 nm) of the supernatants were acquired using a Cary Eclipse spectrofluorometer (Varian).

Compared with the control, the fluorescence intensities of all CNT-labeled FBI samples decreased (Figure 5-10) as a result of CNT-FBI corona formation. Such fluorescence quenching can be attributed to the energy transfer between the labeled FBI (donor) upon excitation and the CNTs (acceptor) upon their binding with the proteins. This energy transfer was efficient for SWNTs because their second van Hove absorption transitions (i.e., 500-900 nm)[15], [239] coincided with the emission of the Alexa Fluor 546 dye. Based on geometrical argument and our surface area measurement, the adsorbing capability of SWNTs was estimated as one order of magnitude higher than that of MWNTs per unit mass. Indeed, the fluorescence intensities were comparable between SWNT and the 10× more concentrated MWNT samples, showing a good correlation between protein adsorption capacity and surface area of the CNTs.

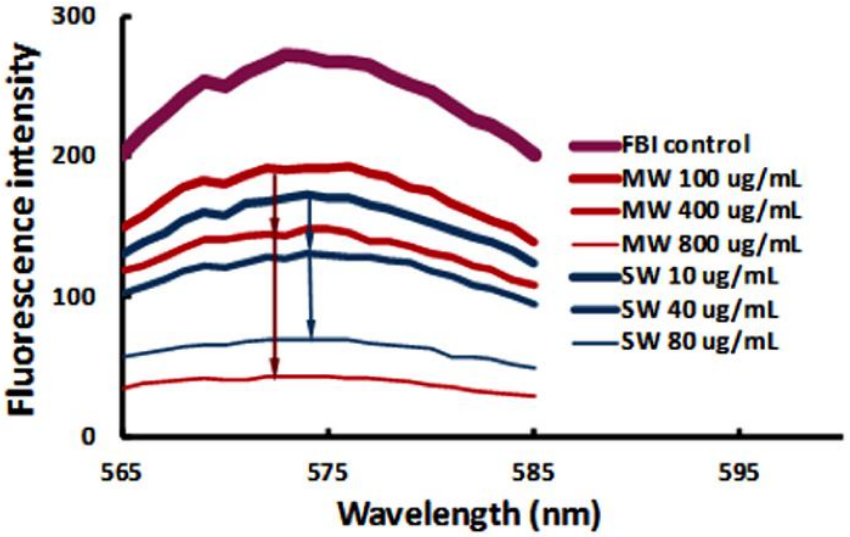

Figure 5-10 Fluorescence intensities of free, labeled FBI supernatants obtained from pelleting SWNT-FBI (blue curves, 10, 40, and 80 μg/mL of the SWNTs) and MWNT-FBI coronas (red curves, 100, 400, and 800 μg/mL of the MWNTs). The fluorescence intensities decreased with increased nanotube concentration for both samples.

The peak fluorescence intensities at 572 nm were plotted for the CNT-labeled FBI samples and fitted using the Stern-Volmer equation:[240] $I_0/I_f = 1 + K_{SV}[CNT]$, here I_0 and I_f are the fluorescence intensities of the labeled FBI (control) and CNT-labeled FBI mixture respectively, K_{SV} is the Stern-Volmer quenching coefficient, and [*CNT*] is the concentration of the nanotubes. The Stern-Volmer plots appeared linear for both SWNT-FBI and MWNT-FBI samples at lower CNT concentrations (first 4 data points in Figure 5-11), indicating a single quenching mechanism. At higher CNT concentrations, however, both curves deviated from linearity to denote occurrence of additional quenching mechanisms. Since collision between CNTs and FBI should occur more frequently at high concentrations the linear Stern-Volmer plots at the low CNT concentrations were attributed to static quenching. Though not substantiated in this study CNTs may also absorb light analogously to blackbody.[241] In our experiment, the molar mass ratio of the SWNTs to MWNTs was 1:418, and therefore the ratio of the Stern-Volmer coefficients for the SWNT-FBI and MWNT-FBI samples was 32.7:(8.8×418)=1:112. This analysis revealed that MWNTs were far more efficient quenchers than SWNTs,

whose smaller diameter and greater curvature were less favorable for the adsorption and alignment of the tubular FBI molecules.

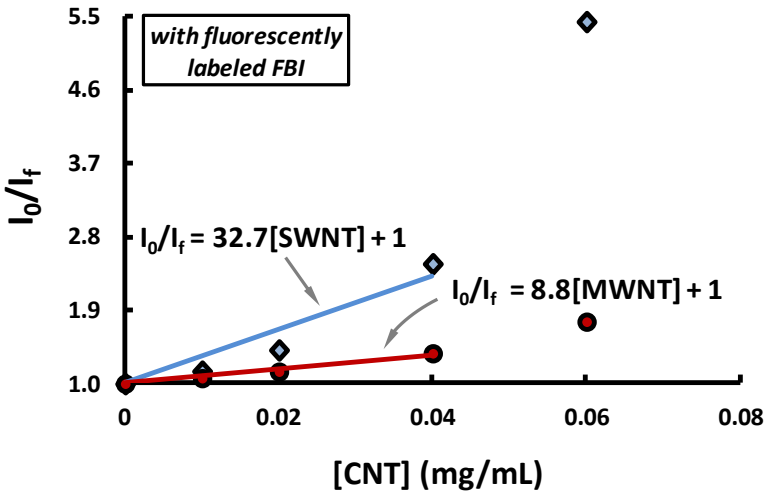

Figure 5-11 Stern-Volmer plots show quenching coefficients of 32.7 and 8.8 for SWNT-FBI and MWNT-FBI coronas, respectively. I_0 and I_f: fluorescence intensities of the labeled FBI control and the CNT-labeled FBI mixture, respectively. CNT concentrations: 0.02 to 0.08 mg/mL.

The fluorescence quenching upon corona formation was utilized to examine the stability of CNT-FBI *in vitro*. For this purpose, HT-29 human colonic adenocarcinoma cell lines were cultured in DMEM with 1% penicillin streptomycin, 1% sodium pyruvate, and 10% fetal bovine serum. Approximately 5,000 cells were seeded in each well of a chambered glass slide and allowed to attach overnight at 37 ℃ with 5% CO_2. The culture medium was then replaced with phosphate buffered saline (PBS) and CNTs coated with purified labeled FBI (free proteins removed by centrifugation) and added in each well to

obtain concentrations of 1.25 and 12.5 μg/mL for the SWNTs and the MWNTs, respectively. This mass concentration ratio of 1:10 was to ensure the same amount of labeled FBI coated on the two types of nanotubes. The CNT-FBI coronas were allowed to incubate with cells for 2 h, followed by washing and replacing with fresh PBS prior to imaging.

As shown in Figure 5-12, the FBI fluorescence is largely quenched in both panels (c) and (d), indicating CNT-FBI corona formation for both SWNTs and MWNTs. Cell adsorption of SWNT-FBI and fluorescence recovery of FBI in intracellular space were evident **(**Figure 5-12e, arrows), suggesting dissociation of SWNTs and FBI post membrane translocation. The isoelectric point of FBI is 5.5,[242] and therefore the proteins were slightly positively charged when stored/processed in endosomes and lysosomes (~pH 4.5) and slightly negatively charged when located in cytosol (~pH 7.2). Since the SWNT surfaces were charge neutral, changes in pH in the intra- and extracellular environment should not drastically impact the binding of SWNT-FBI. The dissociation of SWNTs and FBI is therefore attributed to their differential affinities for the amphiphilic cell membranes.

Pronounced cell adsorption of MWNT-FBI and recovery of FBI fluorescence in the extracellular space were observed, but minimal fluorescence was seen in the intracellular space perhaps due to the high energy cost for MWNT endocytosis (Figure 5-12f). In addition, cell damage (from elongated to round shapes) was more apparent for MWNTs than SWNTs (Figure 5-12f vs. e), likely due to the higher dosage and the toxicity associated with the MWNTs.[243]

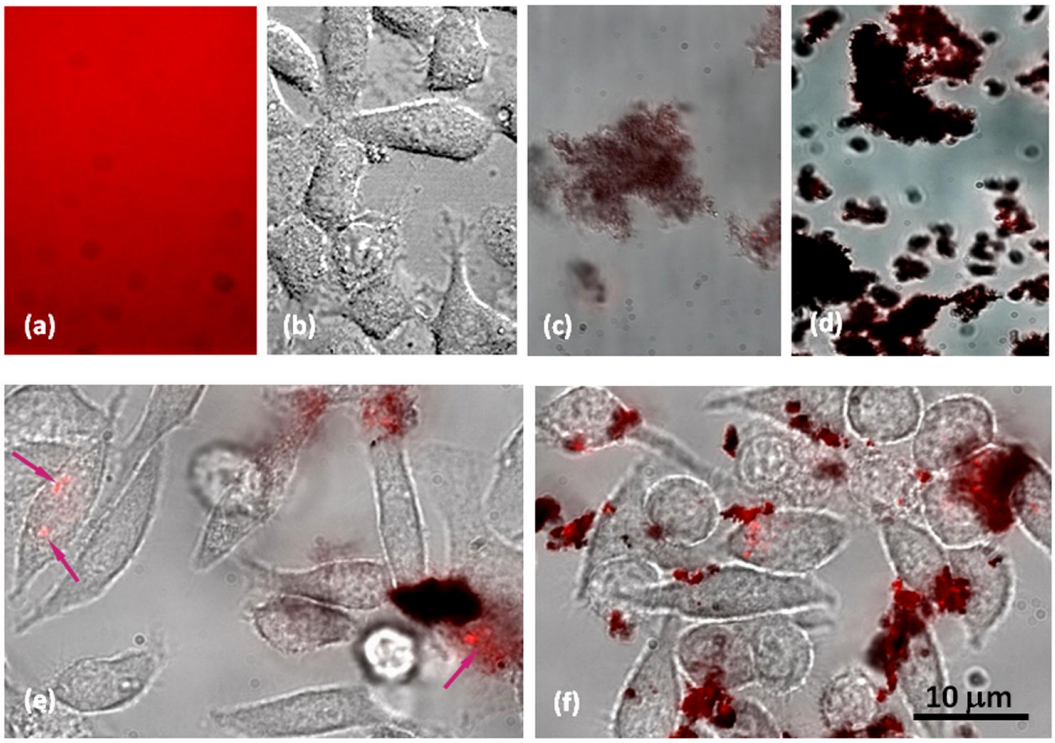

Figure 5-12 HT-29 cell uptake of CNT-FBI coronas overlaid from bright field and confocal fluorescence images. (a, b) Controls of labeled FBI fluorescence and HT-29 cells. (c, d) Controls of SWNT-FBI and MWNT-FBI showing fluorescence quenching. (e) Cell adsorption of SWNT-FBI and FBI fluorescence recovery in the intracellular space (arrows). (f) Pronounced cell adsorption and dissociation of MWNT-FBI in the extracellular space indicated by fluorescence recovery. Cell damage induced by MWNTs is evident. Scale bar: 10 µm for all images.

5.2.3 Conclusion

In short, we have examined the formation and stability of CNT-FBI coronas in the aqueous phase and *in vitro*. The binding between CNTs and FBI is consistent with the high hydrophobic and aromatic moieties of both the protein and the nanotubes. The differential "hardness" and stability of the SWNT-FBI and MWNT-FBI coronas were analyzed based on the concept of buoyant mass and Stern-Volmer plots, and were attributed to the different surface areas and morphology of the two types of CNTs. This study offers a new biophysical perspective for elucidating the concept of NP-protein corona and their dynamic conformational changes, a topic essential to our understanding of the implications and applications of nanomaterials in living systems.

CHAPTER 6. CONCLUSION AND FUTURE WORK

6.1 Conclusions of Dissertation

This dissertation has been focused on an investigation of NP-cell interaction on both the molecular and cellular level, an essential component of our inquiry into the behaviors of NPs in biological and ecosystems. A number of studies have been conducted and described in the chapters, involving characterization of the physicochemistry of NPs and the responses of their host systems upon nanomaterial exposure, using the principles of biophysics, molecular and plant cell biology, and toxicology. The most important observations and conclusions of this dissertation are summarized below.

Differential uptake of fullerene derivatives across plant vs. mammalian cells (chapter 2)

- The difference in the responses of plant and mammalian cells to NPs is a combined result of NP filtration by the porous plant cell wall, confinement on NP mobility by the hydrophobic, thick, and rigid plant cell wall and the amphiphilic, thin, and fluidic plasma membrane, as well as the physiochemical properties of the NPs. The filtration by the plant cell wall favors uptake of smaller and hydrophilic or amphiphilic NPs.
- Post-translocation small and hydrophilic NPs are confined at the interface between the plant cell wall and its plasma membrane, and can self assemble to initiate a mechanical damage to the plasma membrane.

- At high concentrations adsorption of hydrophobic NPs onto the plant cell wall and their retention within the plant cell wall could impact the physiological state of the plant cell.

Absence of a cell wall in mammalian cells is favorable for minimizing the adverse effect of hydrophilic NPs, but encourages membrane partitioning by hydrophobic NPs to induce cell damage. This observation is entirely opposite to that for plant cells mainly due to the presence of a plant cell wall and is consistent with the simulation predictions by Qiao and Ke. [82]

Endocytosis and exocytosis of NPs (chapter 3)

- Increased concentrations of NPs usually enhance their uptake by endocytosis.
- The rate of exocytosis of NPs by mammalian cells correlates with increased Ca^{2+} concentration in the extracellular space.
- Exocytosis of NPs could result in a phase transition in the cell membrane moving from the liquid phase to the gel phase, through recovery of lipids from the exocytosed vesicles.

Surface modifications of nanostructures by proteins and their interactions with cells (chapters 4 and 5)

- Our proteomic analysis have identified and quantified different protein components in the NP-protein coronas formed in cell culture media.

Based on the surface physicochemical properties of the NPs, it is evident that such NP-protein coronas are formed primarily by the physical forces of hydrogen bonding, electrostatic interactions, and hydrophobic interactions.

- Upon binding onto NP surface, proteins typically undergo secondary structural changes to render reduced percentage of α-helices and increased percentage of β-sheets, possibly resulting from breakage of the hydrogen bonds between neighboring α-helices and configuration of new, sterically less ordered hydrogen bonds between the α-helices and the hydrophilic coating of the NPs.
- The NP-specific, low abundance coronal components detected by the proteomic study are proteins of intracellular origin with few or no extracellular domains, representing virtually every subcellular compartment and organelle.
- COOH-functionalized CNTs were found to increase the number of unique proteins associated with the CNTs, compared to non-functionalized raw CNTs, pointing to the role of covalent bonding between the carboxyls of the NTs and amines of the proteins in corona formation.
- The presence of lipid vesicles alleviated the conformational changes of the proteins induced by negatively charged NPs, resulting from the

electrostatic repulsions between the negatively charged vesicles and the NPs.

- Both NPs and NP-protein corona interacted with lipid vesicles to enhance membrane fluidity, although free proteins did not exert much effect on the vesicle conformation due to energetic concerns.
- SWNTs form softer coronas than do MWNTs due to their different morphologies and thus different binding energy landscapes.
- The fibrinogen-adsorbing capability of SWNTs was estimated as one order of magnitude higher than that of MWNTs per unit mass. While MWNTs were far more efficient quenchers than SWNTs, whose smaller diameter and greater curvature were less favorable for the adsorption and alignment of the tubular protein molecules.
- Our fluorescence imaging showed that NP-protein corona could dissociate post its membrane translocation, implying the dynamic nature of such NP-protein complex that is not well understood.

6.2 Future Work

Throughout this PhD research, I have studied the interactions of gold, silver, and fullerene NPs with both plant and mammalian cells, on both the cellular and molecular level. My project has revealed how proteins in biological fluids and in cell culture media may interact, bind, and modify the surfaces of NPs of different physicochemistry, and how those surface modifications may impact the fate of nanomaterials in biological

systems. Such biophysical observations and characterizations have enriched our knowledge regarding the complex phenomena at the nano-bio interface and, at the same time, indicated that much has yet to be learned to better guide the safe development of nanotechnology and protect the environment from the potential pitfalls of discharged nanomaterials. In the light of such an understanding I propose my future work in the following two categories.

1. As delineated throughout this dissertation that NP-biomolecular interactions depend strongly on the shape, size, and surface charge of the NPs and the structural characters of the biomolecules. Thus, I propose to examine the binding of an array of nanomaterials (metal, metal oxides, graphene, graphene oxides, QDs, and plastic) and biomolecules (lipids, amino acids, fatty acids, peptides, and proteins) of different size, surface charge, and surface coating, in order to establish a comprehensive library regarding the binding modes, dynamics and energetics of NP-biocoronas. For example, it would be desirable to compare the interactions of globular HSA and rod-like fibrinogen with both citrate- and PVP-coated AuNPs and Au nanorods, and establish the correlations between NP morphology and the dynamics and hardness of their protein coronas.

2. As aforementioned that the surface modifications of NPs by biomolecules could greatly impact the response of their hosting biological systems, such

as ligand-receptor recognition, uptake, translocation, ROS production, and immune response elicited by the NPs. It is therefore of great relevance and significance that the biological responses to nanomaterials ought to be examined with respect to the entity of NP-protein corona, instead of the properties of the NP alone or the proteins alone. Based on the receptors for a specific cell type that is of interest, we could first surface-modify NPs with their corresponding ligand molecules, determine conformational changes of the ligands residing on the NP surfaces that are induced by physical adsorption and the crowding amongst the packed and free proteins, and then correlate the NP-protein coronas with their cellular uptake, translocation, and cytotoxicity. In addition, the fate of metallic NPs in biological systems should also be examined, for example, in connection with ion release of the NPs, and cellular trafficking, processing, and enzymatic degradation of the NPs. Furthermore, NPs coated by specific antigens could trigger severe immune responses of mast cells and lymphocytes. Testing immune response on those cell types, such as specific and non-specific IgE production, is of great importance for addressing the impact of NP-biocorona on immune systems and therefore shedding light on the connections between NP exposure and human health.

APPENDIX

Glossary of Terms

Symbol	Quantity
AFM	atomic force microscopy
AO/EB	acridine orange/ethdium bromide
ATP	adenosine-5'-triphosphate
BAM	N-tert-butylacrylamide
BFG	bovine fibrinogen
BSA	bovine serum albumin
CB	carbon black
CD	circuar dichroism
CNT	carbon nanotube
CTC	circulating tumor cells
DC-chol	3b-[N-(N′,N′-dimethylaminoethane)- carbamoyl]-cholesterol
DEX	dexamethasone
DMEM	Dulbecco's Modified Eagle's Medium
DMPC	dimyristoyl phosphocholine
DNA	deoxyribonucleic acid
DOPC	dioleoylphosphatidycholine
DOPE	dioleoylphosphatidycholine
DPPC	dioleoylphosphatidycholine
EDS	energy dispersion x-ray spectroscopy
EGF	epidermal growth factor
EGFR	epidermal growth factor receptor
FBI	fibrinogen

FBS	fetal bovine serum
FD	fluorescein diacetate
FDR	false discovery rate
FFT	fast fourier transform
GFP	green fluorescent protein
GP	generalized polarization
GSH	tripeptide glutathione
H-bonding	hydrogen-bonding
HDL	high density lipoprotein
HSA	human serum albumin
HUVEC	human umbilical vein endothelial cells
ITC	isothermal titration calorimetry
IgG	Immunoglobulin G
LFQMS	label-free quantitative mass spectrometry
LPC	lysophophatidylcholine
MD	molecular dynamics
MRI	magnetic resonance imaging
MTT	methyl thiazolyl tetrazolium
MWCNT	multi-walled carbon nanotubes
MWNT	multi-walled nanotube
NIPAM	N-*iso*propylacrylamide
NIR	near infrared
NOM	natural organic matter
NP	nanoparticle
NT	nanotube
oxSWNH	oxidized single-wall carbon nanohorn
PAGE	polyacrylamide gel electrophoresis

PEG	polyethylene glycol
PEG-PHDCA	poly(methoxypolyethyleneglycol cyanoa-crylate-co-hexadecylcyanoacrylate)
PEI	polyethylenimine
PI	propidium iodide
PL-PEG	phospholipid-polyethylene glycol
POPC	palmitoyloleoylphosphocholine
PRM	proline-rich peptide motifs
PVP	polyvinylpyrrolidone
Phe	phenylalanine
QD	quantum dot
RNA	ribonucleic acid
ROS	reactive oxygen species
SC	Subtilisin Carlsberg
SCCHN	squamous cell carcinoma of the head and neck
SDS	sodium dodecyl sulfate
SERS	surface enhanced spectroscopy
siRNA	small interfering ribonucleic acid
SLN	solid lipid nanoparticle
SPR	surface plasmon resonance
SRCD	synchrotron radiation circular dichroism
SWCNT	single-walled carbon nanotube
SWNH	sigle-wall cabon nanohorn
SWNT	single-walled nanotube
TEM	transmission electron microscopy
TNB	Temple-Northeastern-Birmingham
TPP	Trans-Proteomic Pipeline
Tf	transferrin

Trp	tryptophan
Tyr	tyrosine
vdW	*van der Waals*
VEGF	vascular endothelial growth factor
WST	water-soluble tetrazolium

REFERENCE

[1] F. Lao, W. Li, D. Han, Y. Qu, Y. Liu, Y. Zhao, and C. Chen, "Fullerene derivatives protect endothelial cells against NO-induced damage.," *Nanotechnology*, vol. 20, no. 22, p. 225103, Jun. 2009.

[2] J. Weng, X. Song, L. Li, H. Qian, K. Chen, X. Xu, C. Cao, and J. Ren, "Highly luminescent CdTe quantum dots prepared in aqueous phase as an alternative fluorescent probe for cell imaging," *Talanta*, vol. 70, no. 2, pp. 397–402, Sep. 2006.

[3] C. Billotey, C. Wilhelm, M. Devaud, J. C. Bacri, J. Bittoun, and F. Gazeau, "Cell internalization of anionic maghemite nanoparticles: quantitative effect on magnetic resonance imaging.," *Magnetic resonance in medicine : official journal of the Society of Magnetic Resonance in Medicine / Society of Magnetic Resonance in Medicine*, vol. 49, no. 4, pp. 646–54, Apr. 2003.

[4] Z. Cheng, A. K. Chen, H.-Y. Lee, and A. Tsourkas, "Examination of folate-targeted liposomes with encapsulated poly(2-propylacrylic acid) as a pH-responsive nanoplatform for cytosolic drug delivery.," *Small*, vol. 6, no. 13, pp. 1398–401, Jul. 2010.

[5] A. E. Nel, L. Mädler, D. Velegol, T. Xia, E. M. V. Hoek, P. Somasundaran, F. Klaessig, V. Castranova, and M. Thompson, "Understanding biophysicochemical interactions at the nano-bio interface.," *Nature Materials*, vol. 8, no. 7, pp. 543–57, Jul. 2009.

[6] B. D. Chithrani, A. a Ghazani, and W. C. W. Chan, "Determining the size and shape dependence of gold nanoparticle uptake into mammalian cells.," *Nano Letters*, vol. 6, no. 4, pp. 662–8, Apr. 2006.

[7] X. Ma, Y. Wu, S. Jin, Y. Tian, X. Zhang, Y. Zhao, L. Yu, and X.-J. Liang, "Gold nanoparticles induce autophagosome accumulation through size-dependent nanoparticle uptake and lysosome impairment.," *ACS Nano*, vol. 5, no. 11, pp. 8629–39, Nov. 2011.

[8] W. E. N. Jiang, B. Y. S. Kim, J. T. Rutka, and W. C. W. Chan, "Nanoparticle-mediated cellular response is size-dependent," *Nature Nanotechnology*, vol. 3, no. 3, pp. 145–150, Mar. 2008.

[9] J. Huang, L. Bu, J. Xie, K. Chen, Z. Cheng, X. Li, and X. Chen, “Effects of nanoparticle size on cellular uptake and liver MRI with polyvinylpyrrolidone-coated iron oxide nanoparticles.,” *ACS Nano*, vol. 4, no. 12, pp. 7151–60, Dec. 2010.

[10] H.-J. Yen, S.-H. Hsu, and C.-L. Tsai, “Cytotoxicity and Immunological Response of Gold and Silver Nanoparticles of Different Sizes,” *Small*, vol. 5, no. 13, pp. 1553–1561, Jul. 2009.

[11] F. Lu, S.-H. Wu, Y. Hung, and C. Mou, “Size Effect on Cell Uptake in Well-Suspended, Uniform Mesoporous Silica Nanoparticles**,” *Small*, vol. 5, no. x, pp. 1–6, Jun. 2009.

[12] J. Kreuter, “Nanoparticulate systems for brain delivery of drugs.,” *Advanced Drug Delivery Reviews*, vol. 47, no. 1, pp. 65–81, Mar. 2001.

[13] H. R. Kim, I. K. Kim, K. H. Bae, S. H. Lee, Y. Lee, and T. G. Park, “Cationic solid lipid nanoparticles reconstituted from low density lipoprotein components for delivery of siRNA.,” *Molecular pharmaceutics*, vol. 5, no. 4, pp. 622–31, 2008.

[14] K. Pasupathy, S. Lin, Q. Hu, H. Luo, and P. C. Ke, “Direct plant gene delivery with a poly(amidoamine) dendrimer,” *Biotechnology Journal*, vol. 3, no. 8, pp. 1078–1082, Aug. 2008.

[15] S. Lin, G. Keskar, Y. Wu, X. Wang, A. S. Mount, S. J. Klaine, J. M. Moore, A. M. Rao, and P. C. Ke, “Detection of phospholipid-carbon nanotube translocation using fluorescence energy transfer,” *Applied Physics Letters*, vol. 89, no. 14, p. 143118, 2006.

[16] T. Murakami, K. Ajima, J. Miyawaki, M. Yudasaka, S. Iijima, and K. Shiba, “Drug-Loaded Carbon Nanohorns: Adsorption and Release of Dexamethasone in Vitro,” *Molecular Pharmaceutics*, vol. 1, no. 6, pp. 399–405, 2004.

[17] R. Chen, G. Huang, and P. C. Ke, “Calcium-enhanced exocytosis of gold nanoparticles,” *Applied Physics Letters*, vol. 97, no. 9, p. 093706, 2010.

[18] R. Chen, P. Choudhary, R. N. Schurr, P. Bhattacharya, J. M. Brown, and P. Chun Ke, “Interaction of lipid vesicle with silver nanoparticle-serum albumin protein corona.,” *Applied Physics Letters*, vol. 100, no. 1, pp. 13703–137034, Jan. 2012.

[19] C. S. Seney, B. M. Gutzman, and R. H. Goddard, “Correlation of Size and Surface-Enhanced Raman Scattering Activity of Optical and Spectroscopic Properties for Silver Nanoparticles,” *The Journal of Physical Chemistry C*, vol. 113, no. 1, pp. 74–80, Jan. 2009.

[20] a Serra, E. Filippo, M. Re, M. Palmisano, M. Vittori-Antisari, a Buccolieri, and D. Manno, "Non-functionalized silver nanoparticles for a localized surface plasmon resonance-based glucose sensor.," *Nanotechnology*, vol. 20, no. 16, p. 165501, Apr. 2009.

[21] K. a Willets and R. P. Van Duyne, "Localized surface plasmon resonance spectroscopy and sensing.," *Annual Review of Physical Chemistry*, vol. 58, pp. 267–97, Jan. 2007.

[22] M. V. Yigit, L. Zhu, M. a Ifediba, Y. Zhang, K. Carr, A. Moore, and Z. Medarova, "Noninvasive MRI-SERS Imaging in Living Mice Using an Innately Bimodal Nanomaterial.," *ACS Nano*, vol. 5, no. 2, pp. 1056–1066, Dec. 2011.

[23] S. Lin, J. Reppert, Q. Hu, J. S. Hudson, M. L. Reid, T. A. Ratnikova, A. M. Rao, H. Luo, and P. C. Ke, "Uptake, translocation, and transmission of carbon nanomaterials in rice plants.," *Small*, vol. 5, no. 10, pp. 1128–32, May 2009.

[24] K. Welsher, Z. Liu, S. P. Sherlock, J. T. Robinson, Z. Chen, D. Daranciang, and H. Dai, "A route to brightly fluorescent carbon nanotubes for near-infrared imaging in mice.," *Nature Nanotechnology*, vol. 4, no. 11, pp. 773–80, Nov. 2009.

[25] C. F. Bohren, E. Clothiaux, and D. R. Huffman, *Absorption and Scattering of Light by Small Particles*, 2nd ed. New Jersey: Wiley-VCH Hoboken, 2010, p. 700.

[26] D. V. Guzatov, S. V. Vaschenko, V. V. Stankevich, A. Y. Lunevich, Y. F. Glukhov, and S. V. Gaponenko, "Plasmonic Enhancement of Molecular Fluorescence near Silver Nanoparticles: Theory, Modeling, and Experiment," *The Journal of Physical Chemistry C*, vol. 116, no. 19, pp. 10723–10733, May 2012.

[27] X. Wang, X. Qian, J. J. Beitler, Z. G. Chen, F. R. Khuri, M. M. Lewis, H. J. C. Shin, S. Nie, and D. M. Shin, "Detection of circulating tumor cells in human peripheral blood using surface-enhanced Raman scattering nanoparticles.," *Cancer research*, vol. 71, no. 5, pp. 1526–32, Mar. 2011.

[28] C. Loo, A. Lin, L. Hirsch, M.-H. Lee, J. Barton, N. Halas, J. West, and R. Drezek, "Nanoshell-enabled photonics-based imaging and therapy of cancer.," *Technology in cancer research & treatment*, vol. 3, no. 1, pp. 33–40, Feb. 2004.

[29] T. A. Ratnikova, M. J. Bebber, G. Huang, L. L. Larcom, and P. C. Ke, "Cytoprotective properties of a fullerene derivative against copper.," *Nanotechnology*, vol. 22, no. 40, p. 405101, Oct. 2011.

[30] The Project on Emerging Nanotechnologies, “Analysis-This is the first publicly available on-line inventory of nanotechnology-based consumer products.” [Online]. Available: http://www.nanotechproject.org/inventories/consumer/analysis_draft/. [Accessed: 13-Sep-2012].

[31] A. D. Maynard, “NANOTECHNOLOGY : A Research Strategy for Addressing Risk,” 2006.

[32] H. Yang, C. Liu, D. Yang, H. Zhang, and Z. Xi, “Comparative study of cytotoxicity, oxidative stress and genotoxicity induced by four typical nanomaterials: the rolw of particle size, shape and composition,” *Journal of applied toxicology : JAT*, vol. 29, no. 1, pp. 69–78, Jan. 2009.

[33] M. Shi, H. S. Kwon, Z. Peng, A. Elder, and H. Yang, “Effects of surface chemistry on the generation of reactive oxygen species by copper nanoparticles.,” *ACS Nano*, vol. 6, no. 3, pp. 2157–64, Mar. 2012.

[34] E.-J. Park, J. Yi, Y. Kim, K. Choi, and K. Park, “Silver nanoparticles induce cytotoxicity by a Trojan-horse type mechanism.,” *Toxicology in vitro : an international journal published in association with BIBRA*, vol. 24, no. 3, pp. 872–8, Apr. 2010.

[35] R. D. Handy, F. von der Kammer, J. R. Lead, M. Hassellöv, R. Owen, and M. Crane, “The ecotoxicology and chemistry of manufactured nanoparticles.,” *Ecotoxicology (London, England)*, vol. 17, no. 4, pp. 287–314, May 2008.

[36] a Ivask, O. Bondarenko, N. Jepihhina, and A. Kahru, “Profiling of the reactive oxygen species-related ecotoxicity of CuO, ZnO, TiO2, silver and fullerene nanoparticles using a set of recombinant luminescent Escherichia coli strains: differentiating the impact of particles and solubilised metals.,” *Analytical and Bioanalytical Chemistry*, vol. 398, no. 2, pp. 701–16, Sep. 2010.

[37] S. J. H. Soenen, E. Illyes, D. Vercauteren, K. Braeckmans, Z. Majer, S. C. D. Smedt, M. D. Cuyper, S. C. De Smedt, and M. De Cuyper, “The role of nanoparticle concentration-dependent induction of cellular stress in the internalization of non-toxic cationic magnetoliposomes,” *Biomaterials*, vol. 30, no. 30, pp. 6803–6813, Dec. 2009.

[38] S. J. Soenen, P. Rivera-Gil, J.-M. Montenegro, W. J. Parak, S. C. De Smedt, and K. Braeckmans, “Cellular toxicity of inorganic nanoparticles: Common aspects and guidelines for improved nanotoxicity evaluation,” *Nano Today*, pp. 446–465, Sep. 2011.

[39] A. M. Derfus, W. C. W. Chan, and S. N. Bhatia, “Probing the Cytotoxicity of Semiconductor Quantum Dots,” *Nano Letters*, vol. 4, no. 1, pp. 11–18, 2004.

[40] P. Rivera Gil, G. Oberdörster, A. Elder, V. Puntes, and W. J. Parak, “Correlating physico-chemical with toxicological properties of nanoparticles: the present and the future.,” *ACS Nano*, vol. 4, no. 10, pp. 5527–31, Oct. 2010.

[41] S. Hong, J. a. Hessler, M. M. Banaszak Holl, P. Leroueil, A. Mecke, and B. G. Orr, “Physical interactions of nanoparticles with biological membranes: The observation of nanoscale hole formation,” *Journal of Chemical Health and Safety*, vol. 13, no. 3, pp. 16–20, May 2006.

[42] S. M. Hussain, K. L. Hess, J. M. Gearhart, K. T. Geiss, and J. J. Schlager, “In vitro toxicity of nanoparticles in BRL 3A rat liver cells,” *Toxicology in Vitro*, vol. 19, pp. 975–983, 2005.

[43] S. Kittler, C. Greulich, J. Diendorf, M. Köller, and M. Epple, “Toxicity of Silver Nanoparticles Increases during Storage Because of Slow Dissolution under Release of Silver Ions,” *Chemistry of Materials*, vol. 22, no. 16, pp. 4548–4554, Aug. 2010.

[44] Z.-M. Xiu, J. Ma, and P. J. J. Alvarez, “Differential effect of common ligands and molecular oxygen on antimicrobial activity of silver nanoparticles versus silver ions.,” *Environmental science & technology*, vol. 45, no. 20, pp. 9003–8, Oct. 2011.

[45] R. F. Domingos, D. F. Simon, C. Hauser, and K. J. Wilkinson, “Bioaccumulation and effects of CdTe/CdS quantum dots on Chlamydomonas reinhardtii - nanoparticles or the free ions?,” *Environmental science & technology*, vol. 45, no. 18, pp. 7664–9, Sep. 2011.

[46] C. Carlson, S. M. Hussain, a M. Schrand, L. K. Braydich-Stolle, K. L. Hess, R. L. Jones, and J. J. Schlager, “Unique Cellular Interaction of Silver Nanoparticles: Size-Dependent Generation of Reactive Oxygen Species,” *The Journal of Physical Chemistry C*, vol. 112, no. 43, pp. 13608–19, Oct. 2008.

[47] D. Casanova, C. Bouzigues, T.-L. Nguyên, R. O. Ramodiharilafy, L. Bouzhir-Sima, T. Gacoin, J.-P. Boilot, P.-L. Tharaux, and A. Alexandrou, “Single europium-doped nanoparticles measure temporal pattern of reactive oxygen species production inside cells.,” *Nature Nanotechnology*, vol. 4, no. 9, pp. 581–5, Sep. 2009.

[48] L. K. Limbach, P. Wick, P. Manser, R. N. Grass, A. Bruinink, and W. J. Stark, "Exposure of engineered nanoparticles to human lung epithelial cells: influence of chemical composition and catalytic activity on oxidative stress.," *Environmental science & technology*, vol. 41, no. 11, pp. 4158–63, Jun. 2007.

[49] M. Mortimer, K. Kasemets, M. Vodovnik, R. Marinsek-Logar, and A. Kahru, "Exposure to CuO nanoparticles changes the fatty acid composition of protozoa Tetrahymena thermophila.," *Environmental science & technology*, vol. 45, no. 15, pp. 6617–24, Aug. 2011.

[50] W.-K. Oh, S. Kim, M. Choi, C. Kim, Y. S. Jeong, B.-R. Cho, J.-S. Hahn, and J. Jang, "Cellular uptake, cytotoxicity, and innate immune response of silica-titania hollow nanoparticles based on size and surface functionality.," *ACS Nano*, vol. 4, no. 9, pp. 5301–13, Sep. 2010.

[51] K. H. Park, M. Chhowalla, Z. Iqbal, and F. Sesti, "Single-walled carbon nanotubes are a new class of ion channel blockers.," *The Journal of biological chemistry*, vol. 278, no. 50, pp. 50212–6, Dec. 2003.

[52] S. Kraszewski, M. Tarek, W. Treptow, and C. Ramseyer, "Affinity of C60 neat fullerenes with membrane proteins: a computational study on potassium channels.," *ACS Nano*, vol. 4, no. 7, pp. 4158–64, Jul. 2010.

[53] T. A. Ratnikova, P. N. Govindan, E. Salonen, and P. C. Ke, "In vitro polymerization of microtubules with a fullerene derivative.," *ACS Nano*, vol. 5, no. 8, pp. 6306–14, Aug. 2011.

[54] M. Kumari, a Mukherjee, and N. Chandrasekaran, "Genotoxicity of silver nanoparticles in Allium cepa.," *The Science of the total environment*, vol. 407, no. 19, pp. 5243–6, Sep. 2009.

[55] L. He, L. Yang, Z.-R. Zhang, T. Gong, L. Deng, Z. Gu, and X. Sun, "In vitro evaluation of the genotoxicity of a family of novel MeO-PEG-poly(D,L-lactic-co-glycolic acid)-PEG-OMe triblock copolymer and PLGA nanoparticles.," *Nanotechnology*, vol. 20, no. 45, p. 455102, Nov. 2009.

[56] P. V. AshaRani, G. Low Kah Mun, M. P. Hande, and S. Valiyaveettil, "Cytotoxicity and Genotoxicity of Silver Nanoparticles in Human Cells," *ACS Nano*, vol. 3, no. 2, pp. 279–90, Feb. 2009.

[57] B. Trouiller, R. Reliene, A. Westbrook, P. Solaimani, and R. H. Schiestl, "Titanium dioxide nanoparticles induce DNA damage and genetic instability in vivo in mice.," *Cancer research*, vol. 69, no. 22, pp. 8784–9, Nov. 2009.

[58] R. Foldbjerg, D. A. Dang, and H. Autrup, “Cytotoxicity and genotoxicity of silver nanoparticles in the human lung cancer cell line, A549.,” *Archives of toxicology*, vol. 85, no. 7, pp. 743–50, Jul. 2011.

[59] A. Chompoosor, K. Saha, P. S. Ghosh, D. J. Macarthy, O. R. Miranda, Z.-J. Zhu, K. F. Arcaro, and V. M. Rotello, “The role of surface functionality on acute cytotoxicity, ROS generation and DNA damage by cationic gold nanoparticles.,” *Small*, vol. 6, no. 20, pp. 2246–9, Oct. 2010.

[60] H. An and B. Jin, “DNA exposure to buckminsterfullerene (C60): toward DNA stability, reactivity, and replication.,” *Environmental science & technology*, vol. 45, no. 15, pp. 6608–16, Aug. 2011.

[61] I. Papageorgiou, C. Brown, R. Schins, S. Singh, R. Newson, S. Davis, J. Fisher, E. Ingham, and C. P. Case, “The effect of nano- and micron-sized particles of cobalt-chromium alloy on human fibroblasts in vitro.,” *Biomaterials*, vol. 28, no. 19, pp. 2946–58, Jul. 2007.

[62] N. Hanagata, F. Zhuang, S. Connolly, and J. Li, “Molecular Responses of Human Lung Epithelial Cells to the Toxicity of Copper Oxide Nanoparticles Inferred from Whole Genome Expression Analysis,” *ACS Nano*, no. 12, pp. 9326–9338, 2011.

[63] J. Valant, D. Drobne, K. Sepčić, A. Jemec, K. Kogej, and R. Kostanjsek, “Hazardous potential of manufactured nanoparticles identified by in vivo assay.,” *Journal of hazardous materials*, vol. 171, no. 1–3, pp. 160–5, Nov. 2009.

[64] C. M. Sayes, J. D. Fortner, W. Guo, D. Lyon, A. M. Boyd, K. D. Ausman, Y. J. Tao, B. Sitharaman, L. J. Wilson, J. B. Hughes, J. L. West, and V. L. Colvin, “The Differential Cytotoxicity of Water-Soluble Fullerenes,” *Nano Letters*, vol. 4, no. 10, pp. 1881–1887, Oct. 2004.

[65] T. S. Hauck, R. E. Anderson, H. C. Fischer, S. Newbigging, and W. C. W. Chan, “In vivo quantum-dot toxicity assessment.,” *Small*, vol. 6, no. 1, pp. 138–44, Jan. 2010.

[66] Y. Li, Y. Zhou, H.-Y. Wang, S. Perrett, Y. Zhao, Z. Tang, and G. Nie, “Chirality of Glutathione Surface Coating Affects the Cytotoxicity of Quantum Dots,” *Angewandte Chemie*, vol. 123, no. 26, pp. 5982–5986, Jun. 2011.

[67] E. Navarro, A. Baun, R. Behra, N. B. Hartmann, J. Filser, A.-J. Miao, A. Quigg, P. H. Santschi, and L. Sigg, “Environmental behavior and ecotoxicity of engineered nanoparticles to algae, plants, and fungi.,” *Ecotoxicology (London, England)*, vol. 17, no. 5, pp. 372–86, Jul. 2008.

[68] S.-C. Hsieh, F.-F. Wang, C.-S. Lin, Y.-J. Chen, S.-C. Hung, Y.-J. Wang, and A. I. N. Press, "The inhibition of osteogenesis with human bone marrow mesenchymal stem cells by CdSe/ZnS quantum dot labels," *Biomaterials*, vol. 27, no. 8, pp. 1656–1664, Mar. 2006.

[69] N. Lewinski, V. Colvin, and R. Drezek, "Cytotoxicity of Nanoparticles," *Small*, vol. 4, no. 1, pp. 26 – 49, Jan. 2008.

[70] E. Oberdörster, "Manufactured Nanomaterials (Fullerenes, C60) Induce Oxidative Stress in the Brain of Juvenile Largemouth Bass," *Environmental Health Perspectives*, vol. 112, no. 10, pp. 1058–1062, Apr. 2004.

[71] J. Fang, D. Y. Lyon, M. R. Wiesner, J. Dong, and P. J. J. Alvarez, "Effect of a fullerene water suspension on bacterial phospholipids and membrane phase behavior.," *Environmental science & technology*, vol. 41, no. 7, pp. 2636–42, Apr. 2007.

[72] S. Lin, P. Bhattacharya, N. C. Rajapakse, D. E. Brune, and P. C. Ke, "Effects of Quantum Dots Adsorption on Algal Photosynthesis," *The Journal of Physical Chemistry C*, vol. 113, no. 25, pp. 10962–10966, Jun. 2009.

[73] P. Bhattacharya, S. Lin, J. P. Turner, and P. C. Ke, "Physical Adsorption of Charged Plastic Nanoparticles Affects Algal Photosynthesis," *The Journal of Physical Chemistry C*, vol. 114, no. 39, pp. 16556–16561, Oct. 2010.

[74] K.-J. Dietz and S. Herth, "Plant nanotoxicology.," *Trends in Plant Science*, vol. 16, no. 11, pp. 582–589, Sep. 2011.

[75] Q. Liu, Y. Zhao, Y. Wan, J. Zheng, X. Zhang, C. Wang, X. Fang, and J. Lin, "Study of the Inhibitory Effect of Water- Soluble Fullerenes on Plant Growth at the Cellular Level," *ACS Nano*, vol. 4, no. 10, pp. 5743–5748, Oct. 2010.

[76] P. Begum, R. Ikhtiari, and B. Fugetsu, "Graphene phytotoxicity in the seedling stage of cabbage, tomato, red spinach, and lettuce," *Carbon*, vol. 49, no. 12, pp. 3907–3919, Oct. 2011.

[77] "Cell (biology)," *Wikipedia*. [Online]. Available: http://en.wikipedia.org/wiki/Cell_(biology).

[78] "Lipid bilayer," *Wikipedia*. [Online]. Available: http://en.wikipedia.org/wiki/Lipid_bilayer.

[79] "Cell membrane," *Wikipedia*. [Online]. Available: http://en.wikipedia.org/wiki/Cell_membrane.

[80] S. O. Nielsen, B. Ensing, V. Ortiz, P. B. Moore, and M. L. Klein, "Lipid bilayer perturbations around a transmembrane nanotube: a coarse grain molecular dynamics study.," *Biophysical Journal*, vol. 88, no. 6, pp. 3822–8, Jun. 2005.

[81] B. Wang, L. Zhang, S. C. Bae, S. Granick, and S. Chul, "Nanoparticle-induced surface reconstruction of phospholipid membranes," *Proceedings of the National Academy of Sciences of the United States of America*, vol. 105, no. 47, pp. 18171–5, Nov. 2008.

[82] R. Qiao, A. P. Roberts, A. S. Mount, S. J. Klaine, and P. C. Ke, "Translocation of C60 and its derivatives across a lipid bilayer.," *Nano Letters*, vol. 7, no. 3, pp. 614–9, Mar. 2007.

[83] J. Wong-ekkabut, S. Baoukina, W. Triampo, I. Tang, D. P. Tieleman, and L. Monticelli, "Computer simulation study of fullerene translocation through lipid membranes," *Nature Nanotechnology*, vol. 3, pp. 363–368, 2008.

[84] J. Zupanc, D. Drobne, B. Drasler, J. Valant, A. Iglic, V. Kralj-Iglic, D. Makovec, M. Rappolt, B. Sartori, and K. Kogej, "Experimental evidence for the interaction of C-60 fullerene with lipid vesicle membranes," *Carbon*, vol. 50, no. 3, pp. 1170–1178, Mar. 2012.

[85] M. Marsh, "The Structural Era of Endocytosis," *Science*, vol. 285, no. 5425, pp. 215–220, Jul. 1999.

[86] S. D. Conner and S. L. Schmid, "Regulated portals of entry into the cell.," *Nature*, vol. 422, no. 6927, pp. 37–44, Mar. 2003.

[87] M. Marsh, *Endocytosis*. Oxford University Press, USA, 2001.

[88] H. R. Kim, S. Gil, K. Andrieux, V. Nicolas, M. Appel, H. Chacun, D. Desmaële, F. Taran, D. Georgin, and P. Couvreur, "Low-density lipoprotein receptor-mediated endocytosis of PEGylated nanoparticles in rat brain endothelial cells.," *Cellular and molecular life sciences : CMLS*, vol. 64, no. 3, pp. 356–64, Mar. 2007.

[89] A. Verma, O. Uzun, Y. Hu, Y. Hu, H.-S. Han, N. Watson, S. Chen, D. J. Irvine, and F. Stellacci, "Surface-structure-regulated cell-membrane penetration by monolayer-protected nanoparticles.," *Nature Materials*, vol. 7, no. 7, pp. 588–95, Jul. 2008.

[90] J. Zimmerberg, "Molecular Mechanisms of Membrane Fusion: Steps During Phospholipid and Exocytotic Membrane Fuision," *Bioscience Reports*, vol. 7, no. 4, pp. 251–268, Jan. 1987.

[91] P. M. Lledo, “Exocytosis in excitable cells: a conserved molecular machinery from yeast to neuron.,” *European journal of endocrinology / European Federation of Endocrine Societies*, vol. 137, no. 1, pp. 1–9, Jul. 1997.

[92] P. Savigny, J. Evans, and K. M. McGrath, “Cell membrane structures during exocytosis.,” *Endocrinology*, vol. 148, no. 8, pp. 3863–74, Aug. 2007.

[93] E. D. Gundelfinger, M. M. Kessels, and B. Qualmann, “Temporal and spatial coordination of exocytosis and endocytosis.,” *Nature Reviews - Molecular Cell Biology*, vol. 4, no. 2, pp. 127–39, Mar. 2003.

[94] H. Hyung, J. D. Fortner, J. B. Hughes, and J.-H. Kim, “Natural organic matter stabilizes carbon nanotubes in the aqueous phase.,” *Environmental science & technology*, vol. 41, no. 1, pp. 179–84, Jan. 2007.

[95] B. Pan and B. Xing, “Adsorption Mechanisms of Organic Chemicals on Carbon Nanotubes,” *Environmental Science & Technology*, vol. 42, no. 24, pp. 9005–9013, Dec. 2008.

[96] K. Yang and B. Xing, “Adsorption of organic compounds by carbon nanomaterials in aqueous phase: Polanyi theory and its application.,” *Chemical reviews*, vol. 110, no. 10, pp. 5989–6008, Oct. 2010.

[97] N. B. Shah, G. M. Vercellotti, J. G. White, A. Fegan, C. R. Wagner, and J. C. Bischof, “Blood-Nanoparticle Interactions and in Vivo Biodistribution: Impact of Surface PEG and Ligand Properties.,” *Molecular pharmaceutics*, Jul. 2012.

[98] a. V. Bychkova, O. N. Sorokina, a. L. Kovarskii, V. B. Leonova, and M. a. Rozenfel’d, “Interaction between blood plasma proteins and magnetite nanoparticles,” *Colloid Journal*, vol. 72, no. 5, pp. 696–702, Oct. 2010.

[99] Z. J. Deng, G. Mortimer, T. Schiller, A. Musumeci, D. Martin, and R. F. Minchin, “Differential plasma protein binding to metal oxide nanoparticles.,” *Nanotechnology*, vol. 20, no. 45, p. 455101, Nov. 2009.

[100] M. Lück, B. R. Paulke, W. Schröder, T. Blunk, and R. H. Müller, “Analysis of plasma protein adsorption on polymeric nanoparticles with different surface characteristics.,” *Journal of biomedical materials research*, vol. 39, no. 3, pp. 478–85, Mar. 1998.

[101] M. a Dobrovolskaia, A. K. Patri, J. Zheng, J. D. Clogston, N. Ayub, P. Aggarwal, B. W. Neun, J. B. Hall, and S. E. McNeil, "Interaction of colloidal gold nanoparticles with human blood: effects on particle size and analysis of plasma protein binding profiles.," *Nanomedicine : nanotechnology, biology, and medicine*, vol. 5, no. 2, pp. 106–17, Jun. 2009.

[102] P. Aggarwal, J. B. Hall, C. B. McLeland, M. a Dobrovolskaia, and S. E. McNeil, "Nanoparticle interaction with plasma proteins as it relates to particle biodistribution, biocompatibility and therapeutic efficacy.," *Advanced Drug Delivery Reviews*, vol. 61, no. 6, pp. 428–37, Jun. 2009.

[103] S. K. Lai, Y.-Y. Wang, and J. Hanes, "Mucus-penetrating nanoparticles for drug and gene delivery to mucosal tissues.," *Advanced Drug Delivery Reviews*, vol. 61, no. 2, pp. 158–71, Feb. 2009.

[104] B. C. Tang, M. Dawson, S. K. Lai, Y.-Y. Wang, J. S. Suk, M. Yang, P. Zeitlin, M. P. Boyle, J. Fu, and J. Hanes, "Biodegradable polymer nanoparticles that rapidly penetrate the human mucus barrier.," *Proceedings of the National Academy of Sciences of the United States of America*, vol. 106, no. 46, pp. 19268–73, Nov. 2009.

[105] X. Wang, P. Katwa, R. Podila, P. Chen, P. C. Ke, A. M. Rao, D. M. Walters, C. J. Wingard, and J. M. Brown, "Multi-walled carbon nanotube instillation impairs pulmonary function in C57BL/6 mice.," *Particle and fibre toxicology*, vol. 8, no. 1, p. 24, Jan. 2011.

[106] A. a Kapralov, W. H. Feng, A. a Amoscato, N. Yanamala, K. Balasubramanian, D. E. Winnica, E. R. Kisin, G. P. Kotchey, P. Gou, L. J. Sparvero, P. Ray, R. K. Mallampalli, J. Klein-Seetharaman, B. Fadeel, A. Star, A. a Shvedova, and V. E. Kagan, "Adsorption of surfactant lipids by single-walled carbon nanotubes in mouse lung upon pharyngeal aspiration.," *ACS Nano*, vol. 6, no. 5, pp. 4147–56, May 2012.

[107] S. Laera, G. Ceccone, F. Rossi, D. Gilliland, R. Hussain, G. Siligardi, and L. Calzolai, "Measuring protein structure and stability of protein-nanoparticle systems with synchrotron radiation circular dichroism.," *Nano Letters*, vol. 11, no. 10, pp. 4480–4, Oct. 2011.

[108] X. Wu, S.-T. Yang, H. Wang, L. Wang, W. Hu, A. Cao, and Y. Liu, "Influences of the size and hydroxyl number of fullerenes/fullerenols on their interactions with proteins.," *Journal of nanoscience and nanotechnology*, vol. 10, no. 10, pp. 6298–304, Oct. 2010.

[109] G. Zuo, X. Zhou, Q. Huang, H. Fang, and R. Zhou, "Adsorption of Villin Headpiece onto Graphene , Carbon Nanotube , and C60 : Effect of Contacting Surface Curvatures on Binding Affinity," *Journal of Physical Chemistry*, pp. 23323–23328, 2011.

[110] A. a Vertegel, R. W. Siegel, and J. S. Dordick, "Silica nanoparticle size influences the structure and enzymatic activity of adsorbed lysozyme.," *Langmuir : the ACS journal of surfaces and colloids*, vol. 20, no. 16, pp. 6800–7, Aug. 2004.

[111] J. Wang, U. B. Jensen, G. V. Jensen, S. Shipovskov, V. S. Balakrishnan, D. Otzen, J. S. Pedersen, F. Besenbacher, and D. S. Sutherland, "Soft interactions at nanoparticles alter protein function and conformation in a size dependent manner.," *Nano Letters*, vol. 11, no. 11, pp. 4985–91, Nov. 2011.

[112] G. Zuo, Q. Huang, G. Wei, R. Zhou, and H. Fang, "Plugging into proteins: poisoning protein function by a hydrophobic nanoparticle.," *ACS Nano*, vol. 4, no. 12, pp. 7508–14, Dec. 2010.

[113] C. Ge, J. Du, L. Zhao, L. Wang, Y. Liu, D. Li, Y. Yang, R. Zhou, Y. Zhao, Z. Chai, and C. Chen, "Binding of blood proteins to carbon nanotubes reduces cytotoxicity.," *Proceedings of the National Academy of Sciences of the United States of America*, vol. 108, no. 41, pp. 16968–73, Oct. 2011.

[114] S.-T. Yang, Y. Liu, Y.-W. Wang, and A. Cao, "Biosafety and Bioapplication by Designing the Protein-Nanoparticle Interactions," *Unpublished Manuscript*, pp. 1–54.

[115] I. Lynch, T. Cedervall, M. Lundqvist, C. Cabaleiro-Lago, S. Linse, and K. a Dawson, "The nanoparticle-protein complex as a biological entity; a complex fluids and surface science challenge for the 21st century.," *Advances in Colloid and Interface Science*, vol. 134–135, pp. 167–74, Oct. 2007.

[116] G. Baier, C. Costa, A. Zeller, D. Baumann, C. Sayer, P. H. H. Araujo, V. Mailänder, A. Musyanovych, and K. Landfester, "BSA adsorption on differently charged polystyrene nanoparticles using isothermal titration calorimetry and the influence on cellular uptake.," *Macromolecular bioscience*, vol. 11, no. 5, pp. 628–38, May 2011.

[117] L. VROMAN, "Effect of Adsorbed Proteins on the Wettability of Hydrophilic and Hydrophobic Solids," *Nature*, vol. 196, no. 4853, pp. 476–477, Nov. 1962.

[118] L. Vroman, A. L. Adams, G. C. Fischer, and P. C. Munoz, "Interaction of high molecular weight kininogen, factor XII, and fibrinogen in plasma at interfaces," *Blood*, pp. 156–159, 1980.

[119] P. Vilaseca, K. A. Dawson, and G. Franzese, “Understanding surface-adsorption of proteins: the Vroman effect,” *arXiv*, Feb. 2012.

[120] D. Dell’Orco, M. Lundqvist, C. Oslakovic, T. Cedervall, S. Linse, and D. D. Orco, “Modeling the time evolution of the nanoparticle-protein corona in a body fluid.,” *PloS one*, vol. 5, no. 6, p. e10949, Jan. 2010.

[121] M. Lundqvist, J. Stigler, T. Cedervall, T. Berggård, M. B. Flanagan, I. Lynch, G. Elia, and K. Dawson, “The evolution of the protein corona around nanoparticles: a test study.,” *ACS Nano*, vol. 5, no. 9, pp. 7503–9, Sep. 2011.

[122] E. Casals, T. Pfaller, A. Duschl, G. J. Oostingh, and V. Puntes, “Time evolution of the nanoparticle protein corona.,” *ACS Nano*, vol. 4, no. 7, pp. 3623–32, Jul. 2010.

[123] E. Casals, T. Pfaller, A. Duschl, G. J. Oostingh, and V. F. Puntes, “Hardening of the Nanoparticle-Protein Corona in Metal (Au, Ag) and Oxide (Fe(3) O(4) , CoO, and CeO(2)) Nanoparticles.,” *Small*, vol. 7, no. 24, pp. 1–8, Nov. 2011.

[124] V. L. Colvin, “The potential environmental impact of engineered nanomaterials,” *Nature Biotechnology*, vol. 21, no. 10, pp. 1166–1171, 2003.

[125] A. Nel, T. Xia, L. Mädler, and N. Li, “Toxic potential of materials at the nanolevel.,” *Science*, vol. 311, no. 5761, pp. 622–7, Feb. 2006.

[126] A. D. Maynard, R. J. Aitken, T. Butz, V. Colvin, K. Donaldson, G. Oberdörster, M. a Philbert, J. Ryan, A. Seaton, V. Stone, S. S. Tinkle, L. Tran, N. J. Walker, and D. B. Warheit, “Safe handling of nanotechnology.,” *Nature*, vol. 444, no. 7117, pp. 267–9, Nov. 2006.

[127] P. C. Ke and R. Qiao, “Carbon nanomaterials in biological systems,” *Journal of Physics: Condensed Matter*, vol. 19, no. 37, p. 373101, Sep. 2007.

[128] A. A. Shvedova, V. Castranova, E. R. Kisin, D. Schwegler-Berry, A. R. Murray, V. Z. Gandelsman, A. Maynard, and P. Baron, “Exposure to carbon nanotube material: assessment of nanotube cytotoxicity using human keratinocyte cells.,” *Journal of toxicology and environmental health. Part A*, vol. 66, no. 20, pp. 1909–26, Oct. 2003.

[129] K. Kostarelos, L. Lacerda, G. Pastorin, W. Wu, S. Wieckowski, J. Luangsivilay, S. Godefroy, D. Pantarotto, J.-P. Briand, S. Muller, M. Prato, and A. Bianco, “Cellular uptake of functionalized carbon nanotubes is independent of functional group and cell type.,” *Nature Nanotechnology*, vol. 2, no. 2, pp. 108–13, Feb. 2007.

[130] E. Salonen, S. Lin, M. L. Reid, M. Allegood, X. Wang, A. M. Rao, I. Vattulainen, and P. C. Ke, "Real-Time Translocation of Fullerene Reveals Cell Contraction," *Small*, vol. 4, no. 11, pp. 1986–1992, Nov. 2008.

[131] Y. Zhang, M. Yang, J. Park, J. Singelyn, H. Ma, M. J. Sailor, E. Ruoslahti, M. Ozkan, and C. Ozkan, "A surface-charge study on cellular-uptake behavior of F3-peptide-conjugated iron oxide nanoparticles.," *Small*, vol. 5, no. 17, pp. 1990–6, Sep. 2009.

[132] E. C. Cho, J. Xie, P. a Wurm, and Y. Xia, "Understanding the role of surface charges in cellular adsorption versus internalization by selectively removing gold nanoparticles on the cell surface with a I2/KI etchant.," *Nano Letters*, vol. 9, no. 3, pp. 1080–1084, Mar. 2009.

[133] J. L. Ferry, P. Craig, C. Hexel, P. Sisco, R. Frey, P. L. Pennington, M. H. Fulton, I. G. Scott, A. W. Decho, S. Kashiwada, C. J. Murphy, and T. J. Shaw, "Transfer of gold nanoparticles from the water column to the estuarine food web," *Nature Nanotechnology*, vol. 4, no. June, pp. 2–5, 2009.

[134] L. Yang and D. J. Watts, "Particle surface characteristics may play an important role in phytotoxicity of alumina nanoparticles.," *Toxicology letters*, vol. 158, no. 2, pp. 122–32, Aug. 2005.

[135] L. Zheng, F. Hong, S. Lu, and C. Liu, "Effect of Nano-TiO2 on Strength of Naturally Aged Seeds and Growth of Spinach," *Biological trace element research*, vol. 104, no. 1, pp. 83–91, Apr. 2005.

[136] O. I. S. Torney, B. G. Trewyn, V. S. Lin, and K. A. N. Wang, "Mesoporous silica nanoparticles deliver DNA and chemicals into plants," *Nature Nanotechnology*, pp. 295–300, 2007.

[137] Z. Lei, S. Mingyu, L. Chao, C. Liang, H. Hao, W. Xiao, L. Xiaoqing, Y. Fan, G. Fengqing, and H. Fashui, "Effects of Nanoanatase TiO2 on photosynthesis of spinach chloroplasts under different light illumination.," *Biological trace element research*, vol. 119, no. 1, pp. 68–76, Oct. 2007.

[138] D. Lin and B. Xing, "Phytotoxicity of nanoparticles: inhibition of seed germination and root growth.," *Environmental Pollution*, vol. 150, no. 2, pp. 243–50, Nov. 2007.

[139] F. Yang, C. Liu, F. Gao, M. Su, X. Wu, L. Zheng, F. Hong, and P. Yang, "The improvement of spinach growth by nano-anatase TiO2 treatment is related to nitrogen photoreduction.," *Biological trace element research*, vol. 119, no. 1, pp. 77–88, Oct. 2007.

[140] H. Zhu, J. Han, J. Q. Xiao, and Y. Jin, “Uptake, translocation, and accumulation of manufactured iron oxide nanoparticles by pumpkin plants.,” *Journal of environmental monitoring : JEM*, vol. 10, no. 6, pp. 713–7, Jun. 2008.

[141] Q. Liu, B. Chen, Q. Wang, X. Shi, Z. Xiao, J. Lin, and X. Fang, “Carbon nanotubes as molecular transporters for walled plant cells.,” *Nano Letters*, vol. 9, no. 3, pp. 1007–10, Mar. 2009.

[142] J. Shang, T. A. Ratnikova, S. Anttalainen, E. Salonen, P. C. Ke, and H. T. Knap, “Experimental and simulation studies of a real-time polymerase chain reaction in the presence of a fullerene derivative.,” *Nanotechnology*, vol. 20, no. 41, p. 415101, Oct. 2009.

[143] G. Davies, A. Fataftah, A. Cherkasskiy, E. a. Ghabbour, A. Radwan, S. a. Jansen, S. Kolla, M. D. Paciolla, J. L. T. Sein, W. Buermann, M. Balasubramanian, J. Budnick, and B. Xing, “Tight metal binding by humic acids and its role in biomineralization,” *Journal of the Chemical Society, Dalton Transactions*, vol. 1, no. 21, pp. 4047–4060, 1997.

[144] J. Šamaj, F. Baluška, B. Voigt, M. Schlicht, D. Volkmann, and D. Menzel, “Endocytosis, Actin Cytoskeleton, and Signaling,” *Plant Physiology*, vol. 135, pp. 1150–1161, 2004.

[145] P. Gonzalez, J. P. Romero, E. Etxeberria, and E. Baroja-Fernandez, “Fluid phase endocytic uptake of artificial nano-spheres and fluorescent quantum dots by sycamore cultured cells: evidence for the distribution of solutes to different intracellular compartments.,” *Plant signaling & behavior*, vol. 1, no. 4, pp. 196–200, Jul. 2006.

[146] C. T. Brett and K. W. Waldron, *Physiology and Biochemistry of Plant Cell Walls*, 2nd ed. London: Springer, 1996, p. 256.

[147] K. C. Hwang and D. Mauzerall, “Photoinduced electron transport across a lipid bilayer mediated by C70.,” *Nature*, vol. 361, no. 6408, pp. 138–40, Jan. 1993.

[148] R. Chen, T. A. Ratnikova, M. B. Stone, S. Lin, M. Lard, G. Huang, J. S. Hudson, and P. C. Ke, “Differential uptake of carbon nanoparticles by plant and Mammalian cells.,” *Small*, vol. 6, no. 5, pp. 612–7, Mar. 2010.

[149] A. S. Barnard, “One-to-one comparison of sunscreen efficacy, aesthetics and potential nanotoxicity.,” *Nature Nanotechnology*, vol. 5, no. 4, pp. 271–4, Apr. 2010.

[150] S. K. Sahoo and V. Labhasetwar, “Nanotech approaches to drug delivery and imaging,” *Drug Discovery Today*, vol. 8, no. 24, pp. 1112–1120, 2003.

[151] V. Matveev, R. Bertram, and A. Sherman, “Ca2+ current versus Ca2+ channel cooperativity of exocytosis.,” *The Journal of neuroscience : the official journal of the Society for Neuroscience*, vol. 29, no. 39, pp. 12196–209, Sep. 2009.

[152] M. Oheim, F. Kirchhoff, and W. Stühmer, “Calcium microdomains in regulated exocytosis.,” *Cell calcium*, vol. 40, no. 5–6, pp. 423–39, 2006.

[153] M. Coggins and D. Zenisek, “Evidence that exocytosis is driven by calcium entry through multiple calcium channels in goldfish retinal bipolar cells.,” *Journal of neurophysiology*, vol. 101, no. 5, pp. 2601–19, May 2009.

[154] R. S. Zucker, “Exocytosis: a molecular and physiological perspective.,” *Neuron*, vol. 17, no. 6, pp. 1049–55, Dec. 1996.

[155] J. Panyam and V. Labhasetwar, “Dynamics of endocytosis and exocytosis of poly(D,L-lactide-co-glycolide) nanoparticles in vascular smooth muscle cells.,” *Pharmaceutical research*, vol. 20, no. 2, pp. 212–20, Feb. 2003.

[156] H.-J. Kaiser, D. Lingwood, I. Levental, J. L. Sampaio, L. Kalvodova, L. Rajendran, and K. Simons, “Order of lipid phases in model and plasma membranes.,” *Proceedings of the National Academy of Sciences of the United States of America*, vol. 106, no. 39, pp. 16645–50, Sep. 2009.

[157] S. Semrau and T. Schmidt, “Membrane heterogeneity – from lipid domains to curvature effects,” *Soft Matter*, vol. 5, no. 17, p. 3174, 2009.

[158] N. C. Harata, A. M. Aravanis, and R. W. Tsien, “Kiss-and-run and full-collapse fusion as modes of exo-endocytosis in neurosecretion.,” *Journal of neurochemistry*, vol. 97, no. 6, pp. 1546–70, Jun. 2006.

[159] M. Mortimer, R. Järving, A. R. Brash, N. Samel, and I. Järving, “Identification and characterization of an arachidonate 11R-lipoxygenase.,” *Archives of biochemistry and biophysics*, vol. 445, no. 1, pp. 147–55, Jan. 2006.

[160] U. Becherer, T. Moser, W. Stühmer, and M. Oheim, “Calcium regulates exocytosis at the level of single vesicles.,” *Nature Neuroscience*, vol. 6, no. 8, pp. 846–53, Aug. 2003.

[161] M. Liang, I.-C. Lin, M. R. Whittaker, R. F. Minchin, M. J. Monteiro, and I. Toth, “Cellular uptake of densely packed polymer coatings on gold nanoparticles.,” *ACS Nano*, vol. 4, no. 1, pp. 403–13, Jan. 2010.

[162] Y.-L. Zhang, J. a Frangos, and M. Chachisvilis, "Laurdan fluorescence senses mechanical strain in the lipid bilayer membrane.," *Biochemical and Biophysical Research Communications*, vol. 347, no. 3, pp. 838–41, Sep. 2006.

[163] H. Lodish, A. Berk, C. A. Kaiser, M. Krieger, M. P. Scott, A. Bretscher, H. Ploegh, and P. Matsudaira, *Molecular Cell Biology*, 6th ed. San Francisco: W. H. Freeman, 2008.

[164] T. Blunk, D. F. Hochstrasser, J.-C. Sanchez, B. W. Müller, and R. H. Müller, "Colloidal carriers for intravenous drug targeting: Plasma protein adsorption patterns on surface-modified latex particles evaluated by two-dimensional polyacrylamide gel electrophoresis," *Electrophoresis*, vol. 14, pp. 1382–1387, 1993.

[165] M. S. Ehrenberg, A. E. Friedman, J. N. Finkelstein, G. Oberdörster, and J. L. McGrath, "The influence of protein adsorption on nanoparticle association with cultured endothelial cells.," *Biomaterials*, vol. 30, no. 4, pp. 603–10, Feb. 2009.

[166] C. D. Walkey, W. C. W. Chan, and C. S. Reviews, "Understanding and controlling the interaction of nanomaterials with proteins in a physiological environment.," *Chemical Society reviews*, vol. 41, no. 7, pp. 2780–99, Nov. 2012.

[167] R. R. Arvizo, K. Giri, D. Moyano, O. R. Miranda, B. Madden, D. J. McCormick, R. Bhattacharya, V. M. Rotello, J.-P. Kocher, and P. Mukherjee, "Identifying New Therapeutic Targets via Modulation of Protein Corona Formation by Engineered Nanoparticles.," *PloS one*, vol. 7, no. 3, p. e33650, Jan. 2012.

[168] M. Lundqvist, J. Stigler, G. Elia, I. Lynch, T. Cedervall, and K. A. Dawson, "Nanoparticle size and surface properties determine the protein corona with possible implications for biological impacts," *Proceedings of the National Academy of Sciences of the United States of America*, vol. 105, no. 38, pp. 14265–70, Sep. 2008.

[169] M. J. D. Clift, S. Bhattacharjee, D. M. Brown, and V. Stone, "The effects of serum on the toxicity of manufactured nanoparticles.," *Toxicology letters*, vol. 198, no. 3, pp. 358–65, Oct. 2010.

[170] G. Maiorano, S. Sabella, B. Sorce, V. Brunetti, M. A. Malvindi, R. Cingolani, and P. P. Pompa, "Effects of cell culture media on the dynamic formation of protein-nanoparticle complexes and influence on the cellular response.," *ACS Nano*, vol. 4, no. 12, pp. 7481–91, Dec. 2010.

[171] L. Lartigue, C. Wilhelm, J. Servais, C. Factor, A. Dencausse, J.-C. Bacri, N. Luciani, and F. Gazeau, "Nanomagnetic sensing of blood plasma protein interactions with iron oxide nanoparticles: impact on macrophage uptake.," *ACS Nano*, vol. 6, no. 3, pp. 2665–78, Mar. 2012.

[172] A. Panas, C. Marquardt, O. Nalcaci, H. Bockhorn, W. Baumann, H.-R. Paur, S. Mülhopt, S. Diabaté, and C. Weiss, "Screening of different metal oxide nanoparticles reveals selective toxicity and inflammatory potential of silica nanoparticles in lung epithelial cells and macrophages.," *Nanotoxicology*, Jan. 2012.

[173] R. Tedja, M. Lim, R. Amal, and C. Marquis, "Effects of serum adsorption on cellular uptake profile and consequent impact of titanium dioxide nanoparticles on human lung cell lines.," *ACS Nano*, vol. 6, no. 5, pp. 4083–93, May 2012.

[174] A. Beduneau, Z. Ma, C. B. Grotepas, A. Kabanov, B. E. Rabinow, N. Gong, R. L. Mosley, H. Dou, M. D. Boska, and H. E. Gendelman, "Facilitated monocyte-macrophage uptake and tissue distribution of superparmagnetic iron-oxide nanoparticles.," *PloS one*, vol. 4, no. 2, p. e4343, Jan. 2009.

[175] Z. J. Deng, M. Liang, M. Monteiro, I. Toth, and R. F. Minchin, "Nanoparticle-induced unfolding of fibrinogen promotes Mac-1 receptor activation and inflammation.," *Nature Nanotechnology*, vol. 6, no. 1, pp. 39–44, Jan. 2011.

[176] J. Kreuter, R. N. Alyautdin, D. a Kharkevich, and a a Ivanov, "Passage of peptides through the blood-brain barrier with colloidal polymer particles (nanoparticles).," *Brain research*, vol. 674, no. 1, pp. 171–4, Mar. 1995.

[177] R. E. Serda, J. Gu, J. K. Burks, K. Ferrari, C. Ferrari, and M. Ferrari, "Quantitative mechanics of endothelial phagocytosis of silicon microparticles.," *Cytometry. Part A : the Journal of the International Society for Analytical Cytology*, vol. 75, no. 9, pp. 752–60, Sep. 2009.

[178] B. L. Blazer-Yost, A. Banga, A. Amos, E. Chernoff, X. Lai, C. Li, S. Mitra, and F. A. Witzmann, "Effect of carbon nanoparticles on renal epithelial cell structure, barrier function, and protein expression," *Nanotoxicology*, vol. 5, no. 3, pp. 354–371, 2011.

[179] X. Lai, B. L. Blazer-Yost, J. W. Clack, S. L. Fears, S. Mitra, S. A. Ntim, H. N. Ringham, and F. A. Witzmann, "Protein expression profiles of intestinal epithelial co-cultures: effect of functionalized carbon nanotube exposure," *International Journal of Biomedical Nanoscience and Nanotechnology*.

[180] Y. Chen, Z. Iqbal, and S. Mitra, “Microwave-Induced Controlled Purification of Single-Walled Carbon Nanotubes without Sidewall Functionalization,” *Advanced Functional Materials*, vol. 17, no. 18, pp. 3946–3951, Dec. 2007.

[181] Y. Chen and S. Mitra, “Fast Microwave-Assisted Purification, Functionalization and Dispersion of Multi-Walled Carbon Nanotubes,” *Journal of Nanoscience and Nanotechnology*, vol. 8, no. 11, p. 6, 2008.

[182] Y. Wang, Z. Iqbal, and S. Mitra, “Microwave-induced rapid chemical functionalization of single-walled carbon nanotubes,” *Carbon*, vol. 43, no. 5, pp. 1015–1020, Jan. 2005.

[183] S. A. Ntim, O. Sae-Khow, F. a Witzmann, and S. Mitra, “Effects of polymer wrapping and covalent functionalization on the stability of MWCNT in aqueous dispersions.,” *Journal of colloid and interface science*, vol. 355, no. 2, pp. 383–8, Mar. 2011.

[184] S. Tenzer, D. Docter, S. Rosfa, A. Wlodarski, A. Rekik, S. K. Knauer, C. Bantz, T. Nawroth, C. Bier, J. Sirirattanapan, W. Mann, L. Treuel, R. Zellner, M. Maskos, and R. H. Stauber, “Nanoparticle Size Is a Critical Physico- chemical Determinant of the Human Blood Plasma Corona : A Comprehensive Quantitative Proteomic Analysis,” *ACS Nano*, vol. 5, no. 9, pp. 7155–7167, 2011.

[185] H. Zhang, K. E. Burnum, M. L. Luna, B. O. Petritis, J. Kim, W. Qian, R. J. Moore, A. Heredia-langner, B.-J. M. Webb-Robertson, B. D. Thrall, D. G. Camp, R. D. Smith, J. G. Pounds, T. Liu, H. Z. Ã, K. E. B. Ã, and D. G. C. Ii, “Quantitative proteomics analysis of adsorbed plasma proteins classifies nanoparticles with different surface properties and size.,” *Proteomics*, vol. 11, no. 23, pp. 4569–4577, Sep. 2011.

[186] X. Lai, R. L. Bacallao, B. L. Blazer-Yost, D. Hong, S. B. Mason, and F. a Witzmann, “Characterization of the renal cyst fluid proteome in autosomal dominant polycystic kidney disease (ADPKD) patients.,” *Proteomics - Clinical Applications*, vol. 2, no. 7–8, pp. 1140–1152, Jul. 2008.

[187] A. Keller, A. I. Nesvizhskii, E. Kolker, and R. Aebersold, “Empirical statistical model to estimate the accuracy of peptide identifications made by MS/MS and database search.,” *Analytical Chemistry*, vol. 74, no. 20, pp. 5383–92, Oct. 2002.

[188] A. I. Nesvizhskii, A. Keller, E. Kolker, and R. Aebersold, “A statistical model for identifying proteins by tandem mass spectrometry.,” *Analytical Chemistry*, vol. 75, no. 17, pp. 4646–58, Sep. 2003.

[189] X. Lai, L. Wang, H. Tang, and F. a Witzmann, “A novel alignment method and multiple filters for exclusion of unqualified peptides to enhance label-free quantification using peptide intensity in LC-MS/MS.,” *Journal of proteome research*, vol. 10, no. 10, pp. 4799–812, Oct. 2011.

[190] M. E. Monroe, J. L. Shaw, D. S. Daly, J. N. Adkins, and R. D. Smith, “MASIC: a software program for fast quantitation and flexible visualization of chromatographic profiles from detected LC-MS(/MS) features.,” *Computational biology and chemistry*, vol. 32, no. 3, pp. 215–7, Jun. 2008.

[191] J. D. Storey, “A direct approach to false discovery rates,” *Journal of the Royal Statistical Society: Series B (Statistical Methodology)*, vol. 64, no. 3, pp. 479–498, Aug. 2002.

[192] T. Farrah, E. W. Deutsch, G. S. Omenn, D. S. Campbell, Z. Sun, J. a Bletz, P. Mallick, J. E. Katz, J. Malmström, R. Ossola, J. D. Watts, B. Lin, H. Zhang, R. L. Moritz, and R. Aebersold, “A high-confidence human plasma proteome reference set with estimated concentrations in PeptideAtlas.,” *Molecular & cellular proteomics : MCP*, vol. 10, no. 9, p. M110.006353, Sep. 2011.

[193] D. Pacholsky, P. Vakeel, M. Himmel, T. Löwe, T. Stradal, K. Rottner, D. O. Fürst, and P. F. M. van der Ven, “Xin repeats define a novel actin-binding motif.,” *Journal of cell science*, vol. 117, no. Pt 22, pp. 5257–68, Oct. 2004.

[194] H.-T. Huang, O. M. Brand, M. Mathew, C. Ignatiou, E. P. Ewen, S. a McCalmon, and F. J. Naya, “Myomaxin is a novel transcriptional target of MEF2A that encodes a Xin-related alpha-actinin-interacting protein.,” *The Journal of biological chemistry*, vol. 281, no. 51, pp. 39370–9, Dec. 2006.

[195] D. Scumaci, M. Gaspari, M. Saccomanno, G. Argirò, B. Quaresima, C. M. Faniello, P. Ricci, F. Costanzo, and G. Cuda, “Assessment of an ad hoc procedure for isolation and characterization of human albuminome.,” *Analytical Biochemistry*, vol. 418, no. 1, pp. 161–3, Nov. 2011.

[196] R. L. Gundry, Q. Fu, C. a Jelinek, J. E. Van Eyk, and R. J. Cotter, “Investigation of an albumin-enriched fraction of human serum and its albuminome.,” *Proteomics. Clinical Applications*, vol. 1, no. 1, pp. 73–88, Jan. 2007.

[197] R. L. Gundry, M. Y. White, J. Nogee, I. Tchernyshyov, and J. E. Van Eyk, “Assessment of albumin removal from an immunoaffinity spin column: critical implications for proteomic examination of the albuminome and albumin-depleted samples.,” *Proteomics*, vol. 9, no. 7, pp. 2021–8, Apr. 2009.

[198] M. Zhou, D. a Lucas, K. C. Chan, H. J. Issaq, E. F. Petricoin, L. a Liotta, T. D. Veenstra, and T. P. Conrads, "An investigation into the human serum 'interactome'.," *Electrophoresis*, vol. 25, no. 9, pp. 1289–98, May 2004.

[199] M. A. Harris, J. Clark, A. Ireland, J. Lomax, M. Ashburner, R. Foulger, K. Eilbeck, S. Lewis, B. Marshall, C. Mungall, J. Richter, G. M. Rubin, J. A. Blake, C. Bult, M. Dolan, H. Drabkin, J. T. Eppig, D. P. Hill, L. Ni, M. Ringwald, R. Balakrishnan, J. M. Cherry, K. R. Christie, M. C. Costanzo, S. S. Dwight, S. Engel, D. G. Fisk, J. E. Hirschman, E. L. Hong, R. S. Nash, A. Sethuraman, C. L. Theesfeld, D. Botstein, K. Dolinski, B. Feierbach, T. Berardini, S. Mundodi, S. Y. Rhee, R. Apweiler, D. Barrell, E. Camon, E. Dimmer, V. Lee, R. Chisholm, P. Gaudet, W. Kibbe, R. Kishore, E. M. Schwarz, P. Sternberg, M. Gwinn, L. Hannick, J. Wortman, M. Berriman, V. Wood, N. de la Cruz, P. Tonellato, P. Jaiswal, T. Seigfried, and R. White, "The Gene Ontology (GO) database and informatics resource.," *Nucleic acids research*, vol. 32, no. Database issue, pp. D258–61, Jan. 2004.

[200] L. A. Liotta and E. F. Petricoin, "Serum peptidome for cancer detection: spinning biologic trash into diagnostic gold," *Journal of Clinical Investigation*, vol. 116, no. 1, pp. 26–30, 2006.

[201] R. S. Tirumalai, K. C. Chan, D. a Prieto, H. J. Issaq, T. P. Conrads, and T. D. Veenstra, "Characterization of the low molecular weight human serum proteome.," *Molecular & cellular proteomics : MCP*, vol. 2, no. 10, pp. 1096–103, Oct. 2003.

[202] A. a Shemetov, I. Nabiev, and A. Sukhanova, "Molecular interaction of proteins and peptides with nanoparticles.," *ACS Nano*, vol. 6, no. 6, pp. 4585–602, Jun. 2012.

[203] H. T. R. Wiogo, M. Lim, V. Bulmus, J. Yun, and R. Amal, "Stabilization of magnetic iron oxide nanoparticles in biological media by fetal bovine serum (FBS).," *Langmuir : the ACS journal of surfaces and colloids*, vol. 27, no. 2, pp. 843–50, Jan. 2011.

[204] M. P. Monopoli, D. Walczyk, A. Campbell, G. Elia, I. Lynch, F. B. Bombelli, and K. a Dawson, "Physical-chemical aspects of protein corona: relevance to in vitro and in vivo biological impacts of nanoparticles.," *Journal of the American Chemical Society*, vol. 133, no. 8, pp. 2525–34, Mar. 2011.

[205] K. Prapainop and P. Wentworth, "A shotgun proteomic study of the protein corona associated with cholesterol and atheronal-B surface-modified quantum dots.," *European journal of pharmaceutics and biopharmaceutics : official journal of Arbeitsgemeinschaft für Pharmazeutische Verfahrenstechnik e.V*, vol. 77, no. 3, pp. 353–9, Apr. 2011.

[206] G. Caracciolo, L. Callipo, S. C. De Sanctis, C. Cavaliere, D. Pozzi, and A. Laganà, "Surface adsorption of protein corona controls the cell internalization mechanism of DC-Chol-DOPE/DNA lipoplexes in serum.," *Biochimica et Biophysica Acta*, vol. 1798, no. 3, pp. 536–43, Mar. 2010.

[207] A. L. Capriotti, G. Caracciolo, G. Caruso, P. Foglia, D. Pozzi, R. Samperi, and A. Laganà, "Differential analysis of 'protein corona' profile adsorbed onto different nonviral gene delivery systems.," *Analytical Biochemistry*, vol. 419, no. 2, pp. 180–9, Dec. 2011.

[208] A. L. Capriotti, G. Caracciolo, G. Caruso, P. Foglia, D. Pozzi, R. Samperi, A. Lagana, D. Chimica, S. Universita, M. Molecolare, and A. Laganà, "DNA affects the composition of lipoplex protein corona: a proteomics approach.," *Proteomics*, vol. 11, no. 16, pp. 3349–58, Aug. 2011.

[209] A. L. Capriotti, G. Caracciolo, C. Cavaliere, C. Crescenzi, D. Pozzi, and A. Laganà, "Shotgun proteomic analytical approach for studying proteins adsorbed onto liposome surface.," *Analytical and Bioanalytical Chemistry*, vol. 401, no. 4, pp. 1195–202, Sep. 2011.

[210] A. L. Capriotti, G. Caracciolo, G. Caruso, C. Cavaliere, D. Pozzi, R. Samperi, and A. Laganà, "Label-free quantitative analysis for studying the interactions between nanoparticles and plasma proteins.," *Analytical and Bioanalytical Chemistry*, Jan. 2012.

[211] J. Sund, H. Alenius, M. Vippola, K. Savolainen, and A. Puustinen, "Proteomic characterization of engineered nanomaterial-protein interactions in relation to surface reactivity.," *ACS Nano*, vol. 5, no. 6, pp. 4300–9, Jun. 2011.

[212] P. C. Ke and M. H. Lamm, "A biophysical perspective of understanding nanoparticles at large," *Phys. Chem. Chem. Phys.*, 2011.

[213] A. Verma and F. Stellacci, "Effect of Surface Properties on Nanoparticle-Cell Interactions.," *Small*, vol. 6, no. x, pp. 1–10, Jan. 2009.

[214] J. Klein, "Probing the interactions of proteins and nanoparticles.," *Proceedings of the National Academy of Sciences of the United States of America*, vol. 104, no. 7, pp. 2029–30, Feb. 2007.

[215] I. Lynch, A. Salvati, and K. A. Dawson, "Protein-nanoparticle interactions: What does the cell see?," *Nature Nanotechnology*, vol. 4, no. 9, pp. 546–7, Sep. 2009.

[216] I. Lynch and K. A. Dawson, "Protein-nanoparticle Interactions," *Review Literature And Arts Of The Americas*, vol. 3, no. 1, pp. 40–47, Feb. 2008.

[217] T. Cedervall, I. Lynch, S. Lindman, T. Bergg ård, E. Thulin, H. Nilsson, K. A. Dawson, and S. Linse, "Understanding the nanoparticle-protein corona using methods to quantify exchange rates and affinities of proteins for nanoparticles.," *Proceedings of the National Academy of Sciences of the United States of America*, vol. 104, no. 7, pp. 2050–5, Feb. 2007.

[218] V. V. Ginzburg and S. Balijepalli, "Modeling the thermodynamics of the interaction of nanoparticles with cell membranes.," *Nano Letters*, vol. 7, no. 12, pp. 3716–22, Dec. 2007.

[219] Y. Roiter, M. Ornatska, A. R. Rammohan, J. Balakrishnan, D. R. Heine, and S. Minko, "Interaction of Nanoparticles with Lipid Membrane," *Nano Letters*, vol. 8, no. 3, pp. 941–944, 2008.

[220] M. R. R. D. Planque, S. Aghdaei, T. Roose, H. Morgan, and M. R. R. de Planque, "Electrophysiological characterization of membrane disruption by nanoparticles.," *ACS Nano*, vol. 5, no. 5, pp. 3599–606, May 2011.

[221] H. Yuan, J. Li, G. Bao, and S. Zhang, "Variable Nanoparticle-Cell Adhesion Strength Regulates Cellular Uptake," *Physical Review Letters*, vol. 105, no. 13, pp. 1–4, Sep. 2010.

[222] K. Yang and Y.-Q. Ma, "Computer simulation of the translocation of nanoparticles with different shapes across a lipid bilayer.," *Nature Nanotechnology*, vol. 5, no. 8, pp. 579–83, Aug. 2010.

[223] X. Shi, A. von dem Bussche, R. H. Hurt, A. B. Kane, H. Gao, and A. V. Bussche, "Cell entry of one-dimensional nanomaterials occurs by tip recognition and rotation.," *Nature Nanotechnology*, vol. 6, no. 11, pp. 714–9, Nov. 2011.

[224] P. C. Ke and C. a. Naumann, "Single Molecule Fluorescence Imaging of Phospholipid Monolayers at the Air−Water Interface," *Langmuir*, vol. 17, no. 12. pp. 3727–3733, Jun-2001.

[225] C. O. Hendren, X. Mesnard, J. Dröge, and M. R. Wiesner, "Estimating production data for five engineered nanomaterials as a basis for exposure assessment.," *Environmental science & technology*, vol. 45, no. 7, pp. 2562–9, Apr. 2011.

[226] T. Meierhofer, J. M. H. van den Elsen, P. J. Cameron, X. Mu ñoz-Berbel, and a T. a Jenkins, "The interaction of serum albumin with cholesterol containing lipid vesicles.," *Journal of fluorescence*, vol. 20, no. 1, pp. 371–6, Jan. 2010.

[227] D. Pantarotto, C. D. Partidos, R. Graff, J. Hoebeke, J. Briand, M. Prato, and A. Bianco, “Synthesis, Structural Characterization, and Immunological Properties of Carbon Nanotubes Functionalized with Peptides SWNT conjugates was performed by NMR spectroscopy,” *Journal of American Chemical Society*, no. 7, pp. 6160–6164, 2003.

[228] J. L. Bahr and J. M. Tour, “Covalent chemistry of single-wall carbon nanotubes,” *Journal of Materials Chemistry*, vol. 12, no. 7, pp. 1952–1958, Jun. 2002.

[229] R. J. Chen, Y. Zhang, and D. Wang, “Noncovalent Sidewall Functionalization of Single-Walled Carbon Nanotubes for Protein Immobilization,” *Journal of American Chemical Society*, no. 18, pp. 3838–3839, 2001.

[230] M. Zheng, A. Jagota, E. D. Semke, B. a Diner, R. S. McLean, S. R. Lustig, R. E. Richardson, and N. G. Tassi, “DNA-assisted dispersion and separation of carbon nanotubes.,” *Nature Materials*, vol. 2, no. 5, pp. 338–42, May 2003.

[231] R. Rao, J. Lee, Q. Lu, G. Keskar, K. O. Freedman, W. C. Floyd, A. M. Rao, and P. C. Ke, “Single-molecule fluorescence microscopy and Raman spectroscopy studies of RNA bound carbon nanotubes,” *Applied Physics Letters*, vol. 85, no. 18, p. 4228, 2004.

[232] Y. Wu, J. S. Hudson, Q. Lu, J. M. Moore, A. S. Mount, A. M. Rao, E. Alexov, and P. C. Ke, “Coating single-walled carbon nanotubes with phospholipids.,” *The journal of physical chemistry. B*, vol. 110, no. 6, pp. 2475–8, Feb. 2006.

[233] M. Mahmoudi and V. Serpooshan, “Large Protein Absorptions from Small Changes on the Surface of Nanoparticles,” *The Journal of Physical Chemistry C*, vol. 115, no. 37, pp. 18275–18283, Sep. 2011.

[234] S. Milani, F. B. Bombelli, A. S. Pitek, K. A. Dawson, and J. Rädler, “Reversible Versus Irreversible Binding of Transferrin to Polystyrene Nanoparticles: Soft and Hard Corona,” *ACS Nano*, no. 3, pp. 2532–2541, 2012.

[235] S. Brunauer, P. H. Emmett, and E. Teller, “Adsorption of gases in multimolecular layers,” *Journal of the American Chemical Society*, vol. 60, no. 2, pp. 309–319, 1938.

[236] E. P. Barrett, L. G. Joyner, and P. P. Halenda, “The determination of pore volume and area distributions in porous substances. I. Computations from nitrogen isotherms,” *Journal of the American Chemical Society*, vol. 73, no. 1, pp. 373–380, 1951.

[237] M. Mason and W. Weaver, “The settling of small particles in a fluid,” *Physical Review*, vol. 23, no. 3, pp. 412–426, 1924.

[238] G. Gao, T. Çagin, and W. A. Goddard III, “Energetics, structure, mechanical and vibrational properties of single-walled carbon nanotubes,” *Nanotechnology*, vol. 9, pp. 184–191, 1998.

[239] S. M. Bachilo, M. S. Strano, C. Kittrell, R. H. Hauge, R. E. Smalley, and R. B. Weisman, “Structure-assigned optical spectra of single-walled carbon nanotubes.,” *Science*, vol. 298, no. 5602, pp. 2361–6, Dec. 2002.

[240] O. Stern and M. Volmer, “Über die Abklingzeit der Fluoreszenz,” *Physik. Zeitschr.*, vol. 20, p. 183, 1919.

[241] K. Mizuno and J. Ishii, “A black body absorber from vertically aligned single-walled carbon nanotubes,” *Proceedings of the National Academy of Sciences of the United States of America*, vol. 106, no. 15, pp. 6044–6047, 2009.

[242] E. A. Caspary and R. A. Kekwick, “Some physicochemical properties of human fibrinogen,” *Biochemical Journal*, vol. 67, pp. 41–48, 1957.

[243] C. A. Poland, R. Duffin, I. Kinloch, A. Maynard, W. a H. Wallace, A. Seaton, V. Stone, S. Brown, W. Macnee, and K. Donaldson, “Carbon nanotubes introduced into the abdominal cavity of mice show asbestos-like pathogenicity in a pilot study.,” *Nature Nanotechnology*, vol. 3, no. 7, pp. 423–8, Jul. 2008.